

THESIS FOR THE DEGREE OF DOCTOR OF PHILOSOPHY

Microstructure engineering of additively manufactured materials by  
powder bed fusion-laser beam: Cases for ferritic stainless steels and  
medium entropy alloys

SRI BALA ADITYA MALLADI



Department of Industrial and Materials Science

CHALMERS UNIVERSITY OF TECHNOLOGY

Gothenburg, Sweden 2024

Microstructure engineering of additively manufactured materials by powder bed fusion-laser beam: Cases for ferritic stainless steels and medium entropy alloys

SRI BALA ADITYA MALLADI

ISBN: 978-91-7905-989-7

© SRI BALA ADITYA MALLADI, 2024

Doktorsavhandlingar vif Chalmers tekniska högskola

Ny serie nr ISSN 0346-718X

**Series number:** 5455

Department of Industrial and Materials Science

Chalmers University of Technology

SE-412 96 Gothenburg

Sweden

Tel: +46 (0)31 772 1000

Printed by Chalmers digitaltryck

Gothenburg, Sweden 2024

# **Microstructure engineering of additively manufactured materials by laser-based powder bed fusion: Cases for ferritic stainless steels and medium entropy alloy**

Sri Bala Aditya Malladi

Department of Industrial and Materials Science  
Chalmers University of Technology

## **Abstract**

Powder bed fusion laser beam (PBF-LB) is a powder bed fusion additive manufacturing process that is one of the most established and widely used techniques for manufacturing near net shape components. The unique characteristics of PBF-LB, such as the high cooling rates and local directional heat transfer, lead to the formation of unique microstructures. These microstructures can be tailored to achieve desired properties by controlling the process parameters. This thesis studies the influence of PBF-LB processing conditions on the microstructure and resulting properties of two different types of alloys: high alloyed ferritic stainless steels and medium entropy alloys.

Due to the rapid melting and solidification, the resulting microstructure typically consists of columnar grains due to the conditions favourable for the epitaxial growth. Ways to address this include, by either manipulating the process parameters to limit the favourable conditions for epitaxial growth, or by utilizing the alloy design approach to promote the columnar to equiaxed transition. The first part of the thesis focuses on ferritic stainless steels. The influence of inoculation on heterogeneous nucleation and as-printed microstructure is studied in ferritic stainless steels with and without inoculants. The results show that inoculation can promote equiaxed grain growth and significantly reduce the epitaxial growth by altering the solidification conditions.

The second part of the thesis focuses on medium entropy alloys. The influence of interstitial solid solution strengthening on the mechanical properties of CoCrNi-N medium entropy alloys in as-printed and heat-treated conditions is studied. The results show that interstitial solid solution strengthening can improve the mechanical properties of the alloys and also provide significant microstructural stability by delaying the onset of recrystallization and grain growth as compared to the nitrogen free CoCrNi. In addition, the influence of processing conditions, specifically the high cooling rates on the as-printed microstructure, mechanical properties, and TRIP

behaviour of a  $\text{Co}_{45}\text{Cr}_{25}(\text{FeNi})_{30}$  metastable medium entropy alloy is investigated. The results show that processing conditions can significantly affect the microstructure and phase stability which in turn influence the resulting deformation behaviour of the alloy.

The results of this thesis demonstrate that PBF-LB is a versatile process that can be used to produce high-performance materials with tailored microstructure and properties. The findings of this research will be valuable to researchers and engineers who are interested in developing novel alloys and materials by and for additive manufacturing.

**Keywords:** Laser-based powder bed fusion, inoculation, ferritic stainless steels, medium entropy alloys, interstitial solid solution strengthening, microstructural characterization, phase transformation, recrystallization.

## PREFACE

This doctoral thesis is based on the work performed in the Department of Industrial and Materials Science at Chalmers University of Technology from June 2019 to December 2023. The work has been carried out under the supervision of Professor Lars Nyborg and Professor Sheng Guo. This work has been performed within the framework of project funding from strategic innovation program Metalliska Material through the project Design of Novel Materials and Processes for Next Generation Additive Manufacturing (DEMA) supported by the Swedish Governmental Agency for Innovation Systems (VINNOVA) within the framework of the Vinnova, Swedish Energy Agency and FORMAS national innovation programme, and through Centre for Additive Manufacture-Metal (CAM<sup>2</sup>) with support from VINNOVA as well as via the European Union's Horizon 2020 research and innovation programme within the project MANUELA-Additive Manufacturing Using Metal Pilot Line. Support from Chalmers Production Area of Advance is also greatly acknowledged. Support from Swedish Research Council for added costs associated with allocated beam line work as well as the travel grant support from Axel Hultgren foundation for research stay at Kyoto University, Japan is also greatly acknowledged for the support.

This thesis consists of an introductory part with an emphasis on aspects related to microstructural engineering of ferritic stainless steels and medium entropy alloys during additive manufacturing and a summary of results, which are included in the following appended papers.

### List of appended papers:

**Paper I: Grain refinement in additively manufactured ferritic stainless steel by *in situ* inoculation using pre-alloyed powder.**

*A. Durga, Niklas Holländer Pettersson, Sri Bala Aditya Malladi, Zhuoer Chen, Sheng Guo, Lars Nyborg, Greta Lindwall, Scripta Materialia, Vol. 194, 2021, 113690, DOI: 10.1016/j.scriptamat.2020.113690.*

**Paper II: Single track versus bulk samples: Understanding the grain refinement in inoculated ferritic stainless steels manufactured by powder bed fusion-laser beam.**

*Sri Bala Aditya Malladi, Zhuoer Chen, A. Durga, Niklas Holländer Pettersson, Greta Lindwall, Sheng Guo, Lars Nyborg, Materialia, Vol. 32, 2023, 101952, DOI: <https://doi.org/10.1016/j.mtla.2023.101952>.*

- Paper III: Additive Manufacturing of interstitial nitrogen strengthened CoCrNi medium entropy alloy.**  
*Sri Bala Aditya Malladi, Dmitri Riabov, Sheng Guo, Lars Nyborg*  
*Submitted*
- Paper IV: Laser based powder bed fusion of dispersion strengthened CoCrNi by ex-situ addition of TiN.**  
*Sri Bala Aditya Malladi, Laura Cordova, Sheng Guo, Lars Nyborg,*  
*Procedia CIRP, Vol. 111, 2022, 368-372,*  
DOI: <https://doi.org/10.1016/j.procir.2022.08.168>.
- Paper V: Corrosion behaviour of additively manufactured 316L and CoCrNi.**  
*Sri Bala Aditya Malladi, Pui Lam Tam, Yu Cao, Sheng Guo, Lars Nyborg,*  
*Surface and Interface Analysis, Vol. 55, 404-410*  
DOI: <https://doi.org/10.1002/sia.7200>.
- Paper VI: Nitrogen-Mediated Retardation of Recrystallization Kinetics in CoCrNi-N Medium Entropy Alloys Fabricated by Powder Bed Fusion-Laser Beam.**  
*Sri Bala Aditya Malladi, R. Gholizadeh, N. Tsuji, Sheng Guo, Lars Nyborg*  
*In manuscript*
- Paper VII: Understanding phase transformation and mechanical behaviour of an additively manufactured Co<sub>45</sub>Cr<sub>25</sub>(FeNi)<sub>30</sub> metastable medium entropy alloy.**  
*Sri Bala Aditya Malladi, Tatiana Mishurova, Vishnu Anilkumar, Bharat Mehta, Alexander Evans, Kumar Babu Surreddi, Malte Blankenburg, Giovanni Bruno, Sheng Guo, Lars Nyborg*  
*In manuscript*

## **Contribution to the appended papers**

**Paper I:** The author planned the work in collaboration with the co-authors. The corresponding author wrote the paper while the main PBF-LB experimental work was performed by the author who also contributed towards finalizing the paper.

**Paper II:** The author planned and performed the experimental work. Analysis of results was performed in collaboration with the co-authors. The author wrote the paper with the help of co-authors.

**Paper III:** The author planned and performed the experimental work. Analysis of results was performed in collaboration with the co-authors. The author wrote the paper with the help of co-authors.

**Paper IV:** The author planned and performed the experimental work. Analysis of results was performed in collaboration with the co-authors. The author wrote the paper with the help of co-authors.

**Paper V:** The author planned and performed the experimental work. Analysis of results was performed in collaboration with the co-authors. The author wrote the paper with the help of co-authors.

**Paper VI:** The author, along with the support of co-authors planned and performed the experimental work. TEM work was performed by Dr. Reza Gholizadeh. Analysis of results was performed in collaboration with the co-authors. The author wrote the paper with the help of co-authors.

**Paper VII:** The author planned and performed the experimental work along with the support of co-authors. Analysis of results was performed in collaboration with the co-authors. The author wrote the paper with the help of co-authors.





## **Table of Contents**

1	Introduction .....	1
1.1	Background.....	1
1.2	Objectives.....	2
1.3	Research questions .....	3
2	Powder bed fusion-laser beam .....	5
2.1	Working principle.....	5
2.2	Microstructure evolution in PBF-LB .....	5
2.3	Influence of process conditions on the microstructural evolution .....	7
2.3.1	Influence of printing parameters .....	7
2.3.2	Influence of scan strategy.....	8
2.4	Columnar to equiaxed transition.....	9
2.4.1	Inoculation .....	11
2.4.2	Grain control by inoculation in PBF-LB .....	12
3	Materials .....	15
3.1	SS441 ferritic stainless steel .....	15
3.1.1	Microstructure and mechanical properties .....	15
3.2	High entropy alloys and medium entropy alloys.....	16
3.2.1	Phase formation rules in HEAs.....	18
3.2.2	Influence of stacking fault energy (SFE) .....	19
3.2.3	Metastability in HEAs and MEAs.....	20
3.2.4	The CoCrNi MEA.....	21
3.2.5	Non-equiatomic, metastable MEAs.....	23
4	Methods .....	25
4.1	Powder bed fusion-laser beam .....	25
4.2	Metallographic preparation .....	25
4.3	Optical microscopy.....	26
4.4	Scanning electron microscopy .....	26
4.5	Transmission electron microscopy.....	28
4.6	X-ray diffraction.....	29

4.7	High energy X-ray diffraction (HEXRD).....	30
4.8	Hardness .....	33
4.9	Tensile testing.....	33
4.10	Thermodynamic calculations.....	34
5	Summary of results .....	35
5.1	Inoculation in ferritic stainless steels .....	35
5.2	Influence of printing parameters on microstructure of ferritic stainless steels .....	38
5.3	Influence of nitrogen doping on microstructure and properties of CoCrNi medium entropy alloy .....	40
5.3.1	Properties of CoCrNi and CoCrNi-N MEAs.....	44
5.3.2	Corrosion and passivation behaviour of CoCrNi and CoCrNi-N MEAs .....	46
5.4	Recrystallization behaviour of CoCrNi-N MEA .....	47
5.5	Microstructure and mechanical behaviour of Co <sub>45</sub> Cr <sub>25</sub> (FeNi) <sub>30</sub> non-equiatomic medium entropy alloy.....	53
6	Conclusions .....	59
7	Future scope .....	63
	Acknowledgements .....	65
	References .....	67





# **1 Introduction**

## **1.1 Background**

Additive Manufacturing (AM) has revolutionized traditional manufacturing approaches, offering a paradigm shift in the production of metallic materials. The term additive manufacturing (AM) refers to the plethora of techniques which manufactures parts from the 3-dimensional model data by the process of joining materials layer up on layer [1]. According to the ASTM standard 52900:2021, additive manufacturing techniques are classified under 7 different categories and the classification is shown in Figure 1. Among the AM processes, powder bed fusion techniques use high power energy sources such as electron beam (termed, powder bed fusion – electron beam or PBF-EB) and laser beam (termed, powder bed fusion – laser beam or PBF-LB) to selectively melt and solidify the metal particles to achieve full densification. Due to the intrinsic ability of powder bed fusion processes to manufacture near net shape components straight from the 3D model, there is increasing demand in the applications mainly in the fields of automobile, aerospace, and biomedical fields [2–4]. As the demand for such near-net shape manufacturing of customized products grows, these techniques are expected to play an increasingly important role for future manufacturing needs.

Among the powder bed fusion processes, powder bed fusion laser beam (PBF-LB) is one of the most established and widely used techniques owing to its adaptability for various alloy systems and the quality of parts produced. The characteristics of produced components depend on the physical phenomena that take place because of the interaction between the laser and the powder. Especially, the high cooling rates in PBF-LB result in some unique microstructures that are different from their cast counter parts. The local directional heat transfer during the solidification process also influences the microstructure by leading to columnar grain morphologies presenting both opportunities and challenges. This phenomenon, while contributing to the uniqueness of the microstructures, also introduces complexities such as the potential for solidification cracking or anisotropy in the mechanical properties with respect to orientation in the produced parts. Due to these aspects, the interest in development of novel alloys over the past decade has grown exponentially [5–13].

The inherent challenges of PBF-LB, combined with the increasing demand, highlights the critical need for alloys designed to exploit the unique characteristics of the process.

The alloy development strategies should mainly focus on i) reducing the solidification cracking/hot tearing by shortening the solidification range, ii) inducing the inoculation to promote equiaxed grain growth to suppress the formation of solidification cracks and to reduce the anisotropy and iii) improving the mechanical performance of the as-printed parts by taking advantage of the processing conditions and suppressing the formation of undesired phases.

While the cost of additive manufacturing remains a consideration, the unique characteristics of PBF-LB, provides the opportunity to produce the complex alloy systems such as high/medium entropy alloys to near net shape components, which are otherwise laborious to manufacture using traditional techniques. This not only accelerates the development of novel alloys but also unveils microstructures and mechanical properties that are unattainable through traditional routes.

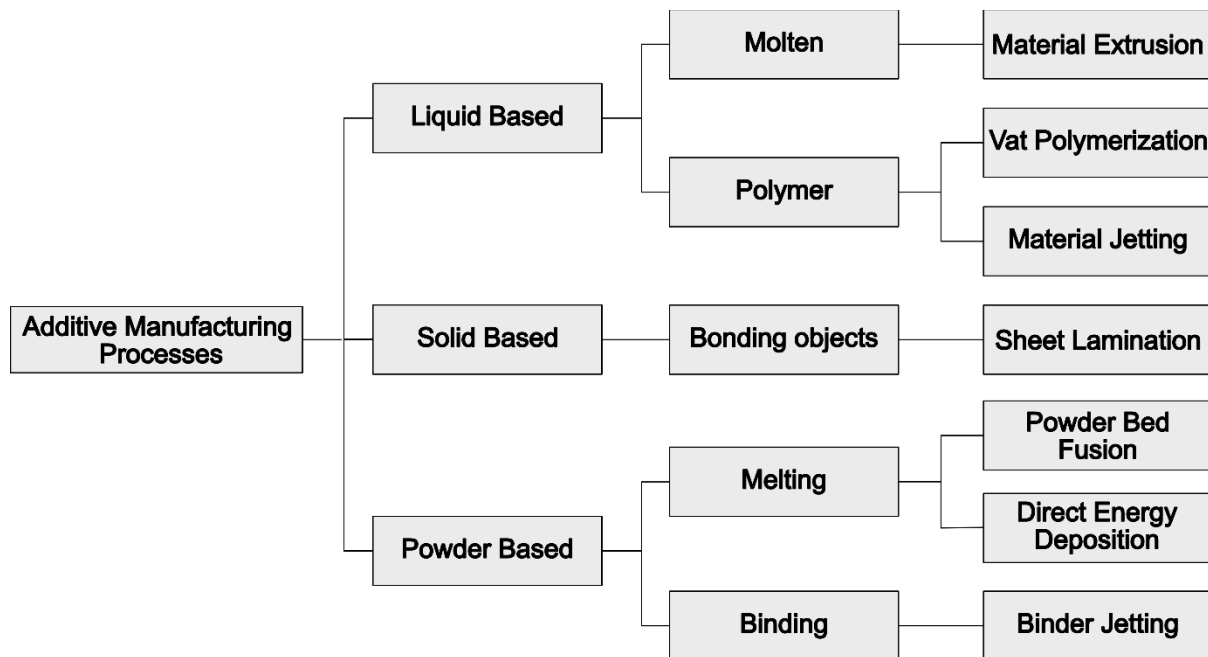


Figure 1 Overview of various additive manufacturing processes [1,14].

## 1.2 Objectives

The aim of this thesis study is to understand the influence of PBF-LB processing conditions on microstructure and the resulting properties of novel high alloyed ferritic stainless steels and medium entropy alloys. The first part of the thesis includes studying the influence of inoculation effect on heterogenous nucleation and as-printed microstructure on ferritic stainless steels with and without inoculants.

The second part of the thesis addresses the influence of PBF-LB process on the microstructure and resulting mechanical properties of two different medium entropy alloys. Specifically, we studied the influence of

1. The interstitial solid solution strengthening of CoCrNi-N medium entropy alloys in as-printed and heat-treated conditions and resulting mechanical response and,
2. The influence of processing conditions on the as-printed microstructure, mechanical properties, and TRIP phenomenon of  $\text{Co}_{45}\text{Cr}_{25}(\text{FeNi})_{30}$  metastable medium entropy alloy.

### 1.3 Research questions

Based on the objectives mentioned in section 1.2, the following research questions were identified and addressed in this thesis study:

*RQ1 What is the influence of in-situ inoculation on the as-printed microstructure of ferritic stainless steel? (Paper I)*

*RQ2 What is the influence of printing parameters on the grain refinement of the inoculated ferritic stainless steel? (Paper II)*

*RQ3 What is the effect of nitrogen doping on the microstructure and properties of CoCrNi medium entropy alloys? (Papers III, IV and V)*

*RQ4 What is the influence of nitrogen doping on the recrystallization kinetics and resulting mechanical properties of the CoCrNi medium entropy alloy? (Paper VI)*

*RQ5 What is the influence of PBF-LB processing on phases stability, resulting mechanical properties for a metastable  $\text{Co}_{45}\text{Cr}_{25}(\text{FeNi})_{30}$  medium entropy alloy? (Paper VII)*





## **2 Powder bed fusion-laser beam**

Among the additive manufacturing techniques in the market today, powder bed fusion (PBF) processes constitute a significant market share [15]. Among the PBF processes, powder bed fusion-laser beam (PBF-LB) is one of the most established, because of its ability to produce net shape components of complex geometries with extremely high precision and with relative ease. This renders PBF-LB more applicable for a variety of industrial domains, such as aerospace, automobile, bio medical, and others where high performance, customized and lightweight parts are needed. The details of the working principle of the typical PBF-LB process, microstructural evolution during the PBF-LB process and influence of the process parameters on the microstructure are discussed in the sections below.

### **2.1 Working principle**

A typical PBF-LB machine consists of a high-power laser, Galvano scanners, powder dispenser, build platform, excess powder collector, and a re-coater. Schematic of the PBF-LB process is shown in Figure 2. The operation sequence of PBF-LB starts with a 3-D computer aided design (CAD) model of the part to be produced. This CAD model of the part is sliced into multiple two-dimensional (2-D) thin slices, also called layers. The information about the CAD design of the 3-D part and the sliced layers is fed to the PBF-LB machine. Based on the information from the sliced 3-D model data, a thin layer (predetermined from the intended layer thickness) of powder is applied on to the build plate. A high-power laser selectively scans the regions on the build plate based on the data from the CAD model, rapidly melting, solidifying, and densifying the scanned regions. The build platform is lowered a distance corresponding to the predetermined layer thickness, and a new layer of powder is recoated from the powder dispenser on the previous layer (already solidified layer). The process of recoating, selective scanning followed by rapid melting and solidification is repeated until the final part is produced. This entire process typically takes place inside a build chamber with an inert atmosphere (most commonly argon). This is done to ensure the oxygen content inside the build chamber is minimum and to avoid formation of any detrimental phases.

### **2.2 Microstructure evolution in PBF-LB**

The rapid melting and solidification events taking place during the PBF-LB process result in local thermal gradients, directional heat flow and high cooling rates which

have considerable influence on the solidification morphology and resulting grain size. Due to the high cooling rates ( $\sim 10^6$  K/s), elemental segregation is confined to very small distances and extremely low as compared to the as-cast materials. This results in unique microstructures which have a direct influence on the resulting mechanical properties of the produced parts. The parts produced through PBF-LB usually tend to have higher strength, but lower ductility and toughness compared to their cast counterparts [14,16]. Like the welding process, the solidification in PBF-LB is governed by two main criteria namely, thermal gradient ( $G$ ) and the solidification speed ( $R$ ). A schematic of the solidification mechanisms as a function of  $G$  and  $R$  are shown in Figure 2. The high cooling rates, along with  $G$  and  $R$ , significantly influence the mode of the solidification microstructure. As  $G$  and  $R$  vary significantly across the melt pool and the printed parts, the resulting microstructure typically combines coarse and fine cellular and dendritic-like structures, depending on the conditions and material being manufactured. This means that solute segregation, resulting from constitutive supercooling ahead of the solidification front, is typically observed during the solidification process.

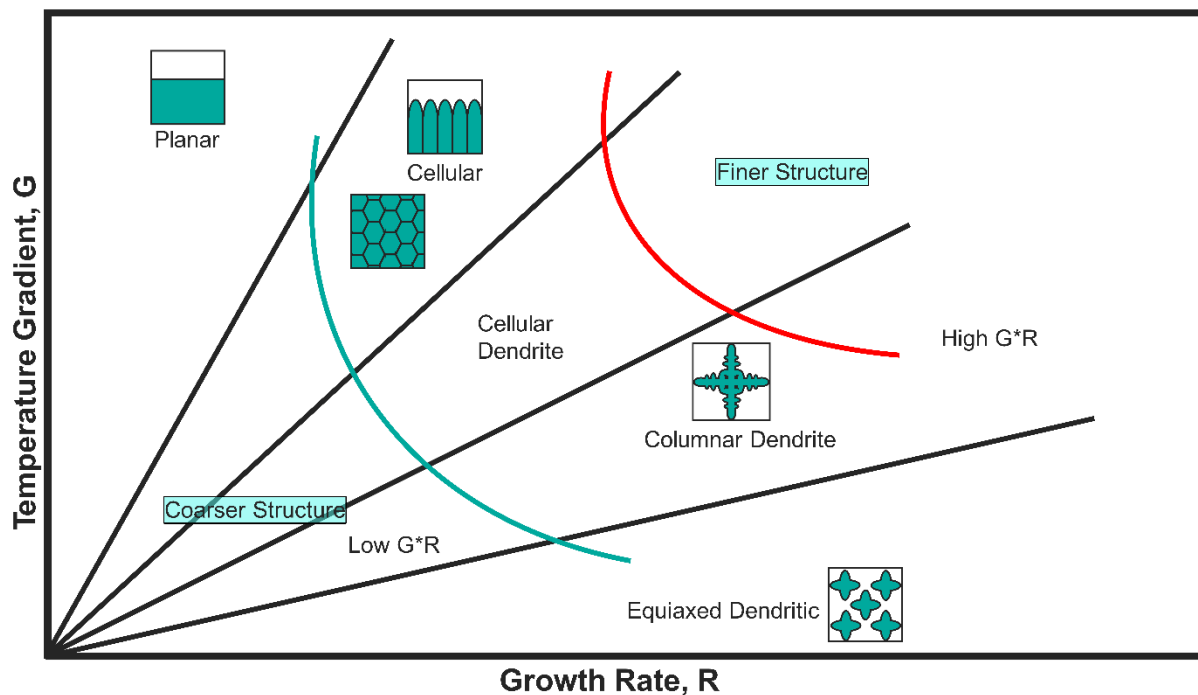


Figure 2 Schematic of the influence of thermal gradient ( $G$ ) and growth rate ( $R$ ) on the solidification mechanism [17].

From the solidification theory, it is known that the grain morphology of the solidified material is influenced by the thermal conditions during the process. Specifically, the ratio of the  $G$  to the  $R$  determines the solidification behaviour and morphology of the

solidified microstructure. In PBF-LB, the high energy laser creates a melt pool that solidifies rapidly as the laser moves away. The solidification starts from the pre-existing grains in the previous layer or the build plate. This means that the new grains grow on top of the old ones, forming columnar structures that span across several layers. This mode of grain growth is known as epitaxial growth. For cubic materials (like BCC and FCC), the columnar grains tend to grow in the  $\langle 100 \rangle$  crystallographic direction, leading to a highly textured material. However, the G/R ratio is not uniform across the melt pool. At the bottom and the edges of the melt pool, where G is high and R is low, the conditions favour columnar grains that grow along the direction of the thermal gradient. At the centre of the melt pool, where G is low and R is high, the conditions favour equiaxed grains that grow in random orientations. Therefore, the solidified material in PBF-LB exhibits a heterogeneous grain structure, often with a mixture of columnar grains and equiaxed grains. A brief overview of the influence of various process conditions and its influence on the microstructure are discussed in the upcoming sections.

## 2.3 Influence of process conditions on the microstructural evolution

Density and microstructure significantly influence the characteristics, properties, and behaviour of alloys. In PBF-LB processes, these attributes are determined by the combination of various processing parameters used during printing. Key parameters include laser power, scanning speed, hatch distance, layer thickness, and scan strategy, as illustrated in Figure 3. These parameters not only define the final densities of the produced parts but also shape the resulting microstructure. This microstructure, in turn, affects the texture, influencing the anisotropy in the mechanical properties of the alloys across different building directions. By adjusting these parameters, one can manipulate the mode of melting (from conduction mode to keyhole mode), which subsequently influences the shape and dimensions of the melt pools and the solidification behaviour. This ultimately determines the microstructure of the manufactured alloys.

### 2.3.1 Influence of printing parameters

Among the above-mentioned PBF-LB parameters, laser power and scan speed play a major role in the solidification dynamics and hence the grain growth. Increasing the laser power is reported to result in the increase in the grain size for titanium, steel, aluminum, and cobalt alloys [18–22]. Materials printed at lower scan speeds are

reported to have larger grains compared to the parts printed at higher scan speeds [19,20,23–27]. Hatch distance has a huge influence on the melting in PBF-LB as it sets the overlap between melt tracks. Any change in the laser power or scan speed needs to be compensated with the hatch distance to achieve full densification. Low laser power or high scan speed need to be compensated with the shorter hatch distance and vice versa for the high laser power and low scan speeds. Though using the high scan speeds results in relatively finer grains inside the melt tracks, using the shorter hatch distance tends to increase the grain size due to the heat build-up by the adjacent tracks [19,23,28]. The magnitude of the above-mentioned parameters also plays a significant role in the resulting residual stresses in the printed parts. For example, longer hatch distance is reported to induce significantly high residual stresses as compared to the shorter hatch distance in Inconel 718 and Ti6Al4V [29,30]. Decrease in scan speed results in lower residual stresses but the lower scan speeds usually need to be compensated by the higher power which result in the opposite effect [31].

Understanding the influence of process parameters on residual stresses is crucial, as these stresses also affect the resulting dislocation densities, which in turn determine the mechanical performance of the alloys. The inherent nature of the layer-by-layer printing process means that the thermophysical phenomena occurring in one layer are repeated in each subsequent layer. This is known as successive thermal cycling (STC). It has been reported that the thermal stresses induced by STC accumulate layer by layer, leading to the generation of dislocations to accommodate these stresses. The cyclic nature of these stresses results in the accumulation of dislocations in a cellular form in energetically favourable locations, which are often the cell walls formed during solidification due to solute segregation (as discussed in Section 2.2) [32–34].

### 2.3.2 Influence of scan strategy

Schematic in Figure 3 shows most common scan strategies used in PBF-LB. Unidirectional and bidirectional scan strategies are the most basic forms of scan strategies. Scan strategy is the pattern that the laser follows while scanning a single layer of powder on the powder bed. This significantly influences the microstructure of the resulting part. If unidirectional or bidirectional scan strategies are used without any scan rotation between the subsequent layers during the printing process, the resulting microstructure is extremely textured and large grains due to the epitaxial growth resulting in strong anisotropy in the mechanical behaviour of the alloy. For example, using unidirectional and bidirectional strategies on 316L is reported to result

in the formation of strong  $\langle 110 \rangle$  texture parallel to the building direction [22,35]. This is because, without any scan rotation, the meltpools perfectly overlap on the pre-existing ones and there is no disruption in thermal gradients resulting in conditions favourable for the epitaxial growth of the columnar grains. However, when the scan rotation between subsequent layers is used, the conditions favourable for the epitaxial growth is minimized resulting in less textured materials. While the scan vectors in unidirectional and bidirectional scan strategies go from edge to edge, stripe and chess board scan strategies divide the area of scanning into multiple smaller islands (as shown in Figure 3c and f). This reduces the temperature inhomogeneity across the scan area resulting in the more uniform distribution of the residual stresses. Using scan rotation along with stripe scan strategy is reported to minimize the texture induced anisotropy by reducing the epitaxial grain growth. Although manipulating the printing parameters could produce smaller grains, due to the complexity of the process conditions the extent to which it refines the grain sizes is limited especially if one aims to produce microstructure with equiaxed grains.

## 2.4 Columnar to equiaxed transition

It is well known that metals and alloys under normal conditions solidify with columnar structure both in casting and PBF-LB as discussed in the sections above. This columnar structure result in the anisotropy of the properties and hence not always desirable, whereas the presence of equiaxed morphology is known to improve the isotropy of mechanical properties of the materials in general [36–38].

As discussed in Section 2.3, one way to achieve the columnar to equiaxed transition (CET) is by manipulating the process parameters and process conditions. Still, even with the manipulation of process parameters, the local heat flow is still directional, therefore the grain growth is still columnar. Another way to address the CET is by using inoculation to increase the number of heterogenous nucleation sites, hence, to promote the CET.

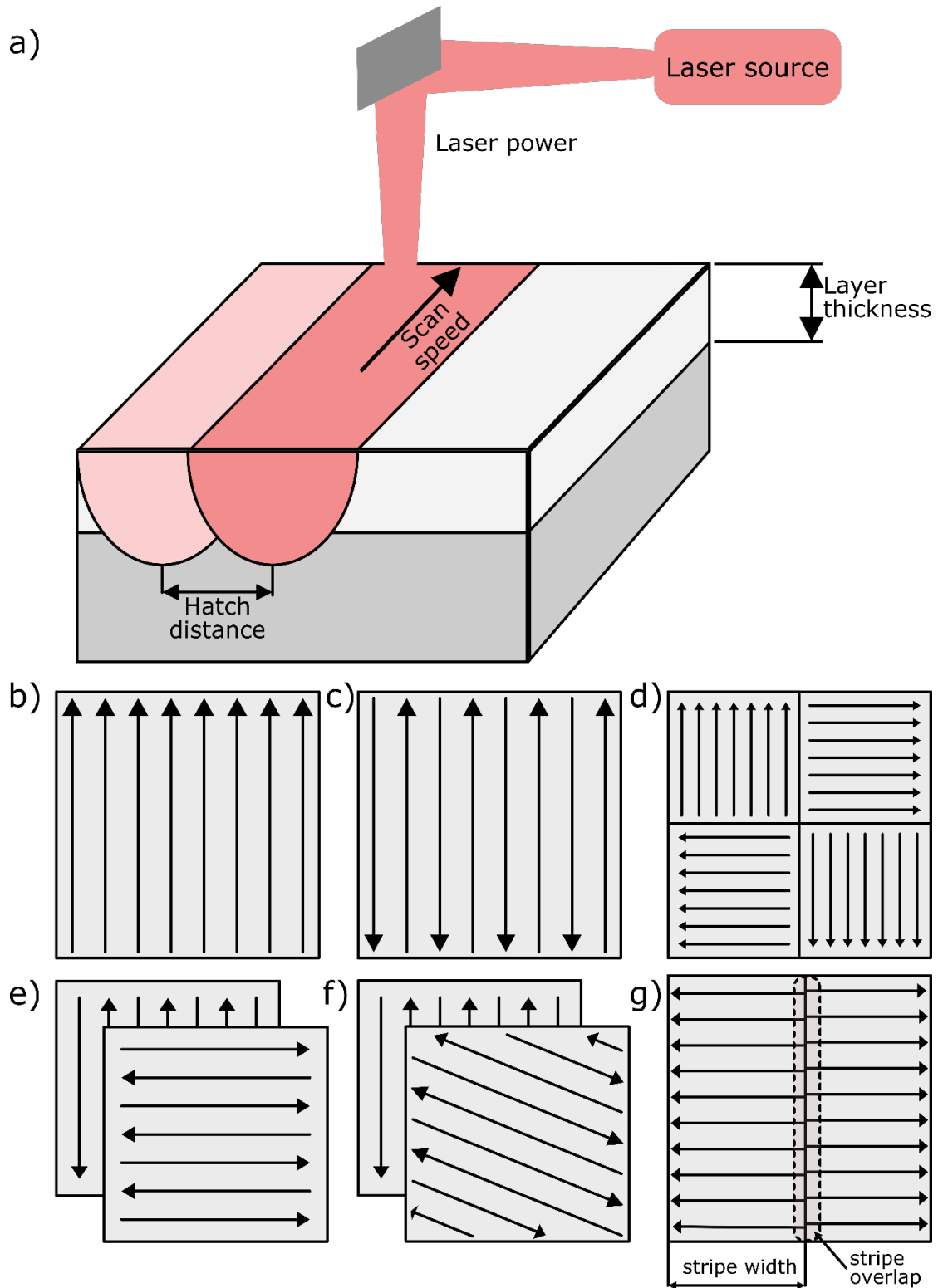


Figure 3 Schematic of a) printing parameters in PBF-LB process and most common scan strategies employed in PBF-LB b) unidirectional scan strategy c) bidirectional scan strategy d) chessboard scan strategy e) 90° rotation between the successive layers f) 67° rotation between the successive layers and g) stripe scan strategy.

### 2.4.1 Inoculation

Solidification in alloys usually proceeds through undercooling which is the process of cooling the melt below the freezing point without the formation of the solid. This undercooling results in the formation of clusters and the cluster on attaining critical size grows into the nuclei. In the case of homogenous nucleation, the degree of undercooling that is required to initiate the solidification could be a few hundreds of degrees, or more specifically about 20% of the melting point in absolute temperature [39,40]. This is rarely possible and in fact, nuclei form at significantly lower undercooling than the conditions required for homogenous nucleation due to the presence of active heterogeneities (solid particles in the melt) paving way for heterogenous nucleation.

One way to accelerate heterogenous nucleation is by the addition of foreign particles called inoculants, which further reduce the degree of undercooling required for the formation of stable nuclei. Inoculation in metals and alloys is the addition of secondary particles to material in its molten state such that the inoculants act as heterogenous nucleating sites for the formation of equiaxed grains, while growth of columnar grains becomes suppressed [36,41–43]. Inoculation is one of the most popular methods to achieve grain refinement due to its simplicity and the approach is widely used [36,44,45]. For any particle to act as an inoculant, it should be able to provide proper wetting of the nucleating alloy. The contact between the inoculant and the matrix is usually treated by a spherical cap model and the equilibrium between the interfacial energies can be expressed as:

$$\gamma_{lp} = \gamma_{sp} + \gamma_{ls} \cos \Theta \quad (1)$$

where  $\gamma_{lp}$ ,  $\gamma_{sp}$  and  $\gamma_{ls}$  are the liquid/particle, solid/particle, and liquid/solid interface energies, respectively, and  $\Theta$  is the contact angle as shown in Figure 4. For an inoculant to be effective, it should satisfy the following requirements:

- i) *it should have higher melting point than the alloy being solidified,*
- ii) *it should be able to initiate freezing at very small undercooling,*
- iii) *number density of the particles in the melt should be high,*
- iv) *the nucleating particles should be larger than a critical size depending on the undercooling of the melt [36,41].*

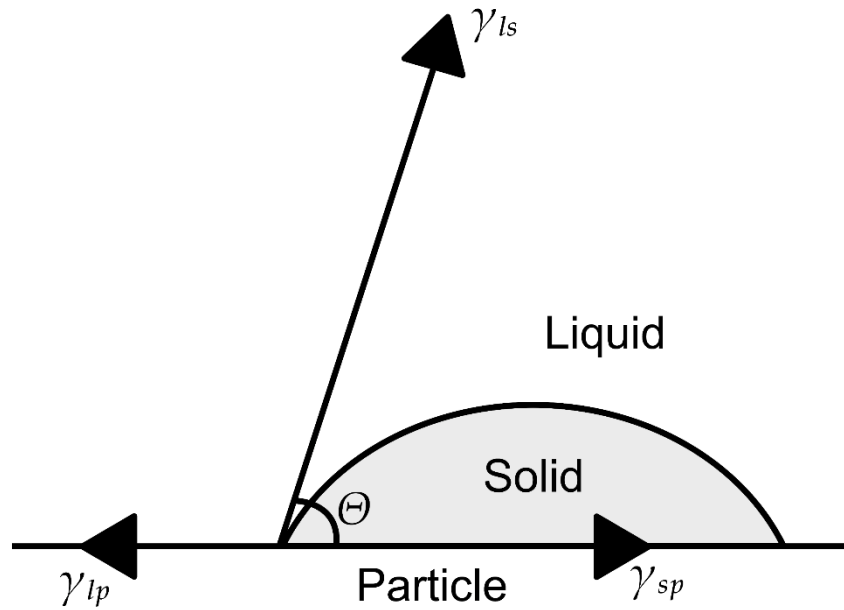


Figure 4 Spherical cap model depicting the equilibrium of interfacial energies between the solid, liquid, and the nucleating particle [36,40].

#### 2.4.2 Grain control by inoculation in PBF-LB

As mentioned in the previous sections, because of the rapid melting and solidification mechanisms which result in complex thermal gradients and solidification velocities, epitaxially grown columnar grains are common in PBF-LB. In many case, these grow across several meltpools along the building direction [35,46,47]. Addition of nucleating particles either in-situ (by alloy design leading to precipitation) or by ex-situ additions to achieve the grain refinement has been studied for materials such as Ti-6Al-4V, Al- alloys, Fe-alloys and HEAs [44,45,48]. Addition of elements such as boron, carbon, tungsten, and compounds such as TiN,  $\text{La}_2\text{O}_3$  in particulate form to the Ti-alloys has proven to be better grain refiners owing to their ability to enhance the constitutive super cooling [49]. Their addition is reported to result in the refinement of prior- $\beta$  grain size, refining the  $\alpha$ -lath size and refinement of  $\alpha$ -grains [48–52]. Potential applications and use cases for the aluminum alloys produced by PBF-LB for the aerospace applications are high, owing to the advantages of the manufacturing route. However, apart from the anisotropy induced by the columnar grains, printing of some of the age-hardenable aluminum alloys such as 6000 and 7000 series is very challenging due to the hot cracking induced by the rapid melting and solidification conditions. Equiaxed grain structure resulting from the heterogenous nucleation with the help of inoculation in these aluminum alloys not only addresses the anisotropy but also addresses the hot cracking due to better distribution of the thermal strain in



the fine grain structures. The grain size refinement in the 6000 and 7000 series aluminum alloys was reported to be achieved by the ex-situ addition of the hydrogen-stabilized zirconium nanoparticles. During solidification, the added nanoparticles react and form  $\text{Al}_3\text{Zr}$  which acted as inoculants for the grain refinement with the aforementioned effect of limiting hot cracking [44]. Similarly, addition of Ti is reported to induce a similar effect on the 2000 series aluminum alloys [53,54]. This was reported to be achieved in-situ by alloy design to incorporate Ti which during solidification reacts with Al to form  $\text{Al}_3\text{Ti}$ , a well-known inoculant for aluminum alloys [36,55].

Among the grain refinement studies for the high entropy alloys produced via PBF-LB, Cantor alloys are the only systems that have been studied [56,57]. Addition of the TiN nanoparticles ex-situ was shown to induce the grain size refinement resulting in change of strong  $\langle 001 \rangle$  texture to random structure. The addition of TiN to this alloy system was reported to improve the yield strength of the alloy but to decrease the ductility. However, the mechanism of grain refinement by the addition of TiN to Cantor alloy system is still unclear and needs further verification [56].

Though austenitic stainless steels (mostly 316L) are one of the widely studied alloys for PBF-LB, the grain refinement was mainly achieved by manipulating the printing parameters. The addition of particles such as MgO and NbO is known to influence the nucleation on undercooling for casting conditions but not much work has been reported for PBF-LB conditions. Ferritic stainless steels, on the other hand, are gaining interest in the PBF-LB community due to their excellent printability and ability to solidify with fine equiaxed grains [58–60]. The TiN is a well-known inoculant for the ferritic steels owing to its low lattice misfit with the ferrite matrix and ability to increase the constitutional supercooling required for the heterogeneous nucleation [61]. Ferritic stainless-steel grade SS441, which is dual alloyed with niobium and titanium, is reported to form TiN in-situ during solidification in the presence of nitrogen [60]. Similarly, Ti-alloyed ferritic steel grades are also reported to achieve excellent printability with a fine equiaxed grain structure [58,59,62].



### 3 Materials

#### 3.1 SS441 ferritic stainless steel

The most researched and used alloys for powder bed fusion – laser beam techniques include austenitic stainless steels, titanium alloys, aluminium alloys, cobalt chrome, nickel base super alloys, and copper-based alloys [25,63–67]. Ferritic stainless steels have received little to no attraction in the field of additive manufacturing (AM). SS441 stainless steel is one of the grades of the ferritic stainless steels which is used in the automobile industry specifically for catalytic convertors. Materials for catalytic convertor applications require excellent thermal fatigue resistance and high temperature strength as the operating temperatures are as high as 900°C. One of the biggest challenges for the utilization of ferritic stainless steels at these temperatures is, however, is due to the depletion of chromium in the form of carbides. SS441 on the other hand is a titanium and niobium dual-stabilized steel, whose carbides are more stable than chromium carbides there by depleting the available carbon for sensitization [68]. However, the presence of niobium poses a challenge by its ability in forming Laves phases which lead to embrittlement and loss of high temperature strength [69,70]. The presence of Laves phase in SS441 is not always detrimental as in case of solid oxide fuel cells (SOFC), where SS441 is used as an interconnector. At the operating conditions of the SOFC's, niobium and titanium rich Laves phase interacts with silicon and prevent the formation of insulating silica layer [71].

##### 3.1.1 Microstructure and mechanical properties

The traditional manufacturing method for SS441 is by casting and hot rolling with an equiaxed microstructure of grain size around 50  $\mu\text{m}$  with the distribution of TiN particles inside the grains and Nb (C, N) particles at the grain boundaries [60,69,70,72]. However, due to the large local thermal gradients and solidification velocities in the PBF-LB process, SS441 is known to undergo cellular solidification with niobium-rich particles accumulated to the cell walls and some titanium-rich particles inside the grains, which themselves can attain average grain size of about 1.6  $\mu\text{m}$  [60]. Upon annealing, the niobium-rich cell walls assist in the formation of Laves phase. The SS441 manufactured through the PBF-LB is shown to exhibit high yield strength (~ 680 – 740 MPa) attributed to the small grain size and cellular solidification structure compared to its wrought counterpart (~ 314 MPa) [60].

Table 1 Chemical compositions in weight percent of the alloy powder grades used in this study.

Alloy	Cr	Si	Mn	Nb	Ti	Ni	N	C	O	P	S	Fe
SS441	19.5	0.9	0.8	0.8	0.3	0.1	0.1	0.03	0.03	0.01	0.007	Balance
Ti-free	18.0	0.7	0.8	-	0.01	0.1	0.1	0.01	0.1	0.01	0.01	Balance
Ti-high	19.5	0.9	0.9	-	0.8	0.2	0.12	0.02	-	0.01	0.01	Balance

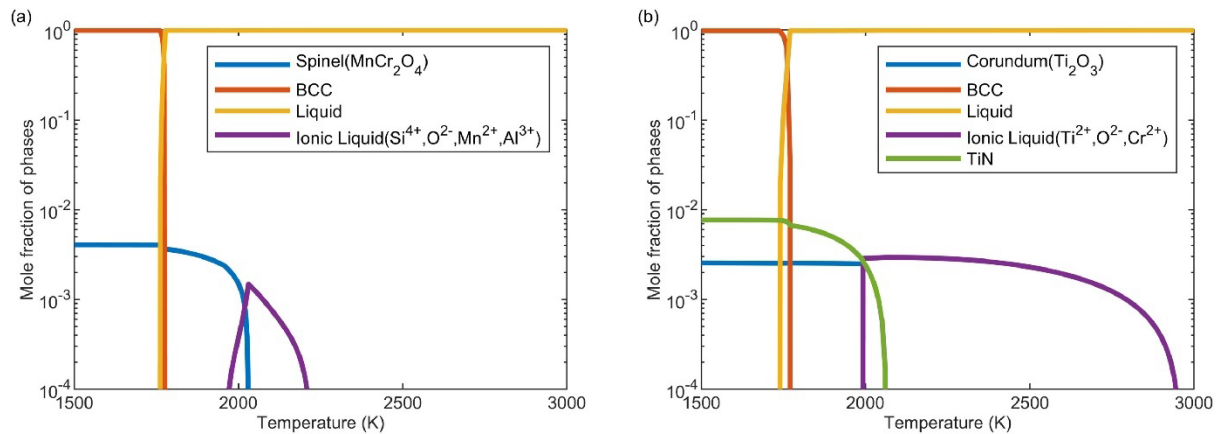


Figure 5 Phase fractions at equilibrium as a function of temperature calculated for the (a) Ti-free and (b) Ti-high as-built compositions listed in Table 1 [62].

In this study, three different variants of pre-alloyed gas-atomized powder based on SS441, were supplied by Kanthal AB, with particle size distribution ranging from 10 to 45  $\mu\text{m}$ . The chemical composition of the stainless-steel powder variants under the present study is mentioned in Table 1. Computational thermodynamic models based on CALPHAD were used for designing 1) to maximize the amount of TiN available during the solidification and 2) to minimize the possibility of formation of detrimental phases such as Laves phase, which would deplete the titanium available to form TiN, see Figure 5.

### 3.2 High entropy alloys and medium entropy alloys

Traditional alloying, the practice that has been around for millennia, involves using a base metal with desirable properties and selectively adding other elements in controlled quantities to enhance these properties. This approach, however, restricts compositional freedom and limits the exploration of phase diagrams, barely scratching the surface of potential alloy combinations. Another challenge is the limited availability of new, stable metallic elements that could serve as the foundation for developing new alloy systems.

As technology continues to advance, there is an increasing need to improve the material properties. For instance, the energy and aerospace industries require materials with improved high-temperature properties, while the transportation sector generally needs lighter and more cost-effective alloys.

In 2004, two research groups, Cantor et al. [73] and Yeh et al. [74], simultaneously addressed this issue by introducing a new concept of alloys called High Entropy Alloys (HEAs). This innovative approach to alloying explores the centre of the multi-element phase diagram, where there is no obvious base element, opening new possibilities in material science by introducing novel alloy systems. The original definition of the HEAs is based on the entropy effect. Yeh et al. [74] hypothesized that for an ideal solid solution (enthalpy of mixing,  $\Delta H_{mix}$  is zero), the free energy of formation of the alloy depends mainly on the entropy part as shown in the equation below:

$$\Delta G_{mix} = -T\Delta S_{mix} \quad (2)$$

where,  $\Delta G_{mix}$  is the Gibbs free energy of mixing,  $\Delta S_{mix}$  is the entropy of mixing and  $T$  is the absolute temperature. Boltzmann's equation for ideal entropy of mixing is given by:

$$\Delta S_{mix} = -R\sum x_i \ln x_i \quad (3)$$

where,  $R$  is the gas constant and  $x_i$  is the mole fraction of the  $i^{th}$  element. If the alloy is an equiatomic alloy with  $n$  elements, the above equation changes to

$$\Delta S_{mix} = -R \ln n \quad (4)$$

Utilizing the equation for the configurational entropy of mixing, we find that the entropy values for equiatomic alloys composed of 4, 5, and 6 elements are  $1.39R$ ,  $1.61R$ , and  $1.79R$ , respectively. From this, we can infer that HEAs were initially defined as alloys containing at least five elements, each with elemental concentrations ranging from 5 to 35 atom percent. When the entropy value exceeds  $1.6R$ , the contribution of the mixing entropy to the total free energy of the system becomes significant enough to counteract the mixing enthalpies associated with the formation of intermetallics and phase separation resulting in the formation of simple and stable solid solution phases. The magnitude of the mixing entropy is used to classify alloys into three categories: low-entropy alloys (traditional alloys), medium entropy alloys (MEAs), and HEAs, as depicted in Figure 6 [75–78].

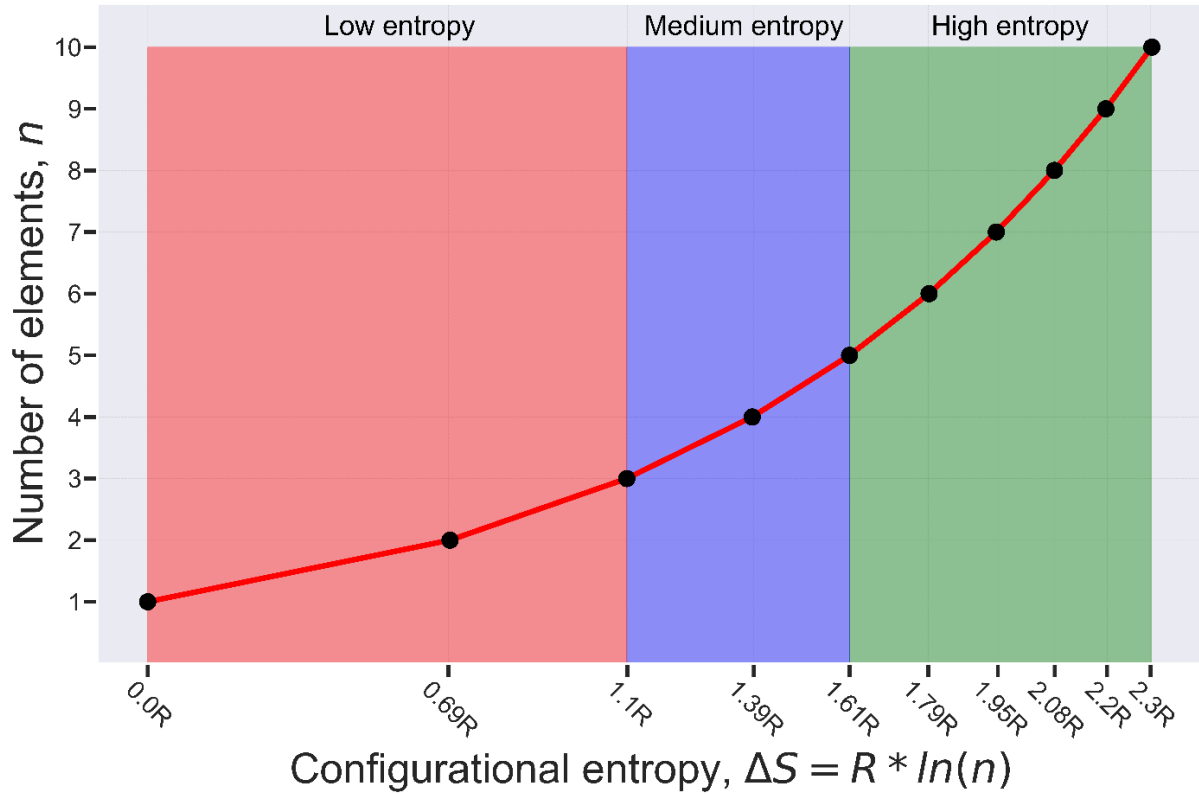


Figure 6 Classification of alloys based on the value of configurational entropy of mixing.

### 3.2.1 Phase formation rules in HEAs

While entropic stabilization can partially explain why some HEAs contain single-phase solid solutions, it does not fully explain the formation of intermetallics, complex compounds and even amorphous phases [79–83]. Zhang et al. [84] and Guo et al. [84,85] tried to explain the phase formation rules by considering the factors such as *enthalpy of mixing* ( $\Delta H_{mix}$ ), *entropy of mixing* ( $\Delta S_{mix}$ ), *atomic size difference* ( $\delta$ ), *electronegativity difference* ( $\Delta\chi$ ) and *valence electronic configurations* (VEC). They concluded that high configurational entropy of mixing is not the only factor that controls the formation and stabilization of the phases in HEAs, and solid solutions can form when,

$$-22 \leq \Delta H_{mix} \leq 7 \text{ kJ/mol},$$

$$0 \leq \delta \leq 8.5 \text{ and}$$

$$11 \leq \Delta S_{mix} \leq 19.5 \text{ J/(K}\cdot\text{mol)}$$

On the other hand, the valence electron configuration (VEC) plays a crucial role in determining whether Face-Centred Cubic (FCC) or Body-Centred Cubic (BCC) solid solutions are formed. It was concluded that VEC greater than 8 favours the formation

of FCC type solid solutions, VEC less than 6.87 favours the formation of BCC solid solutions, and mixture of BCC and FCC solid solutions forms when  $6.87 < \text{VEC} < 8.0$  [84–88]. In addition to the aforementioned parameters influencing the phase stability and formation of various solid solutions in HEAs, researchers have suggested a few more empirical parameters, providing additional insights into phase formation [88–90]. However, a comprehensive understanding of phase stability, especially for solid solution types other than FCC and BCC, remains elusive [87].

Recently the relaxation to the equiatomic rule was also proposed resulting in the HEAs and MEAs with both equiatomic and non-equiatomic compositions which could result in the stabilization of single or multi-phase solid solutions [79,91–101]. This relaxation has further expanded the development of alloys with varying atomic percentages of constituent elements. Some of the examples of MEAs are CoCrNi, CoNiV, CoCrFeNi,  $\text{Ni}_{46}\text{Cr}_{23}\text{Co}_{23}\text{Al}_4\text{Ti}_4$ , etc. Even though these alloys are MEAs, they have shown exceptional phase stability and even superior properties compared to their HEA counterparts [79,102–106].

### 3.2.2 Influence of stacking fault energy (SFE)

Stacking faults are the planar defects that interrupt the ideal stacking sequence of the crystalline planes in crystalline materials. They are categorized into two types: intrinsic and extrinsic stacking faults. The intrinsic stacking faults are formed when a plane of atoms is missing from its ideal stacking sequence (due to the vacancies) while the extrinsic stacking faults are formed when an extra plane of atoms disrupt the ideal stacking sequence (often due to the presence of interstitials). Stacking faults are generated by the dissociation of a perfect dislocation into two partial dislocations. When a dislocation with Burgers vector  $a/2\langle 110 \rangle$  dissociates, it generates two Shockley partial dislocations with Burgers vector  $a/6\langle 112 \rangle$  and the region in between these two Shockley partials is stacking fault. Stacking fault energy (SFE) is the energy associated with the formation of such partial dislocations and it is an intrinsic material property [107–110]. Two main factors that influence the SFE of an alloy are 1) the chemical composition of the alloy [101,111], and 2) the working temperature [112]. The SFE significantly influences the deformation behaviour of the alloys. Alloys are generally categorized based on their SFE and the corresponding deformation mechanisms they exhibit. High SFE alloys primarily deform through slip, while those with a moderate SFE, experience twinning during deformation and hence are also referred to as TWIP alloys. On the other hand, alloys with low SFE, are characterized

by phase transformation upon deformation and hence they are termed as TRIP alloys [100,113,114]. Consequently, SFE plays a crucial role in mechanical behaviour of the alloys and the ability to manipulate SFE allows the design of alloys with tailored mechanical properties [115].

### 3.2.3 Metastability in HEAs and MEAs

As discussed in the previous section, the composition of the alloy plays a crucial role for the SFE which in turn influences the mechanical behaviour. Extremely high compositional complexity of HEAs means that SFE plays an even greater role in the deformation behaviour of the alloys. In case of HEAs, the SFE is also likely to be influenced by the local chemical and structural changes resulting in more complex and competing underlying mechanisms determining their mechanical behaviour [110,111,116]. Due to this fact there is increasing interest in the field of HEAs to design alloys to manipulate SFE resulting in materials with improved strength without compromising the ductility of the alloys, improved damage tolerance and other functional properties [10,98–100,109,113,114,117–121]. One of the most studied HEAs is CoCrFeMnNi, owing to its exceptional strength, damage tolerance and fracture toughness both at room temperature and under cryogenic conditions [112,122]. Liu et al. studied the influence of chemical composition on the SFE and its influence on mechanical properties for alloy system based on CoCrFeMnNi. They concluded that with increasing Co content, the SFE decreases resulting in the increase in the free energy difference between the resulting FCC and HCP phases rendering FCC being more metastable. They also reported that with the increase in the Co content, the deformation mode of the alloys changed from dislocation slip to TWIP and with further increase in the Co content, eventually TRIP with HCP phase transformation upon deformation. This resulted in significant improvement in the mechanical behaviour with yield strength increase from about 640 MPa to 820 MPa and ductility increase from about 52% to 69% when the alloy composition was changed from equiatomic CoCrFeMnNi to  $\text{Co}_{30}\text{Cr}_{20}\text{Ni}_{10}\text{Fe}_{20}\text{Mn}_{20}$  [115].



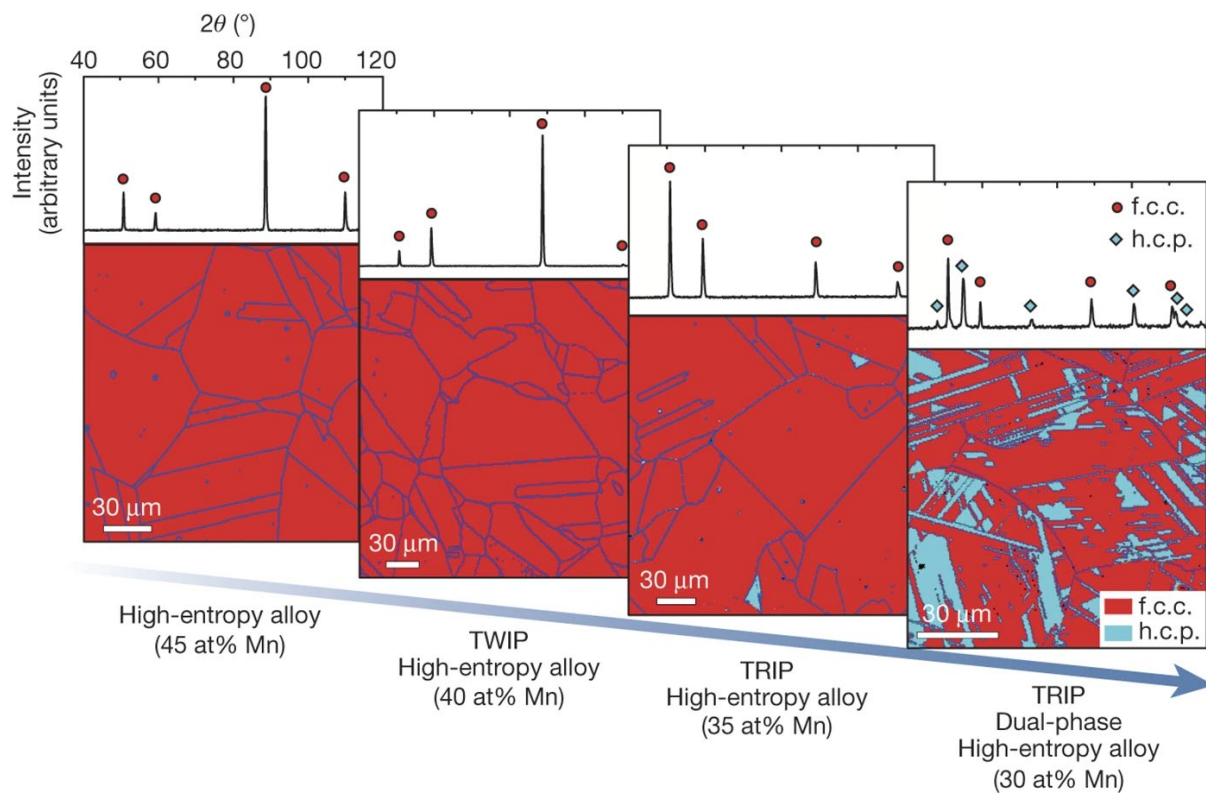


Figure 7 XRD patterns and EBSD phase maps of  $\text{Fe}_{80-x}\text{Mn}_x\text{Co}_{10}\text{Cr}_{10}$  ( $x = 45 \text{ at\%}, 40 \text{ at\%}, 35 \text{ at\%}$  and  $30 \text{ at\%}$ ) HEAs. Taken with permission from [100]

Another such example is  $\text{Fe}_{80-x}\text{Mn}_x\text{Co}_{10}\text{Cr}_{10}$ ; by changing the Mn and Fe concentrations simultaneously introduces the metastability resulting in changing deformation mode from dislocation cross slip to TWIP. Further increase in the Mn content resulted in the alloy with formation of FCC + HCP system, which up on deformation could further undergo TRIP by significant amount of strain hardening [100]. The EBSD phase maps showing the influence of alloy composition on resulting mechanical behaviour of the alloy are shown in Figure 7. A similar change in the SFE and resulting mechanical properties by carefully tuning the composition of the principal elements was observed by many researchers [79,91,97,98,118,123] underlining the potential considerations for SFE as important criteria for designing HEAs. In the coming sections, a brief overview of the alloys used in this study is presented.

### 3.2.4 The CoCrNi MEA

Equiatomic single-phase FCC, CoCrNi is the most widely studied MEA owing to its high strength and ductility, excellent corrosion and oxidation resistance, enhanced hydrogen embrittlement resistance and excellent cryogenic properties [103,106,124–127]. This material is also known to provide high strain hardening due to its ability to undergo deformation twinning upon plastic deformation because of its stacking fault

energy (SFE) [102]. The DFT simulations of CoCrNi proved that metastability of FCC phase resulting in the athermal transformation further strengthening the alloy up on deformation both at room temperature and at low temperatures [128,129].

Addition of nitrogen or carbon as interstitial elements to CoCrNi alloy was observed to further enhance its yield strength without compromising the ductility, high temperature properties and corrosion resistance [130–136]. It has also been reported that addition of carbon and nitrogen as interstitial solid solution strengtheners would increase the SFE of CoCrNi. This results in delayed onset of twinning (so called TWIP effect) resulting in improved yield strength without compromising the ductility [135,137]. Still, once the twinning is initiated in the presence of interstitials, the thickness of the twin lamellae formed was observed to be smaller than those in CoCrNi. The presence of interstitials with the nano-scaled twins can hence possibly act as obstacles for the dislocation movement as well as Frank Read sources for dislocation generation resulting in significantly improved strain hardening response for the alloy [135].

Another significant advantage of the addition of interstitial elements to the HEAs/MEAs in general is their influence on the recrystallization behaviour of the alloys [131,138–141]. Particularly in case of wrought CoCrNi, addition of carbon and nitrogen as interstitials is reported to lead to Cr-rich precipitates resulting Zener pinning effect of the grain boundaries, thereby inhibiting the growth of grains resulting in improved high temperature stability of the alloy.

*Table 2 Elemental compositions of powder and as-printed samples of CoCrNi and CoCrNi-N alloys used in this thesis work.*

Material	Co, wt%	Cr, wt%	Ni, wt%	N, wt%	O, wt%
CoCrNi (Powder)	34.05	29.80	36.10	0.003	0.038
CoCrNi-N (Powder)	34.4	30.70	34.60	0.18	0.04
CoCrNi (As-printed)	34.05	29.80	36.10	0.002	0.038
CoCrNi-N (As-printed)	34.48	30.76	34.6	0.12	0.04

Two different variants of equiatomic CoCrNi MEAs were used in the present study. One variant was prealloyed with nitrogen (CoCrNi-N) and the other variant was

without any nitrogen. In both cases, pre-alloyed spherical powder with a D90 of 45  $\mu\text{m}$  for both the variants were supplied by Höganäs AB, Sweden. The elemental compositions of both CoCrNi and CoCrNi-N, powder, and as-printed samples used in this thesis work are presented in the Table 2.

### 3.2.5 Non-equiatomc, metastable MEAs

As discussed in section 3.2.3, introducing metastability induced by SFE into the alloy design further expands the scope of MEAs resulting in non-equiatomc compositions. One such alloy system is based on the equiatomc CoCrFeNi MEA [117]. Wei et. al. showed that for  $\text{Co}_x\text{Cr}_{25}(\text{FeNi})_{75-x}$ , by changing the atomic fractions of Co, Fe and Ni simultaneously, the SFE is lowered destabilizing the FCC. This in turn resulted in the change in mechanical response of the alloys with change in the deformation response of the alloy. The influence of the composition on  $\text{Co}_x\text{Cr}_{25}(\text{FeNi})_{75-x}$  system on SFE and the resulting phase stability of the FCC and HCP phases is shown in Figure 8.

The MEA used in the present study is of composition  $\text{Co}_{45}\text{Cr}_{25}(\text{FeNi})_{30}$  which is single phase metastable FCC alloy (when manufactured using wrought metallurgy) and is known to undergo martensitic transformation (HCP) through TRIP on deformation. Our aim is to study the influence of various factors on the mechanical properties of such alloy, and the TRIP effect, when fabricated via PBF-LB. Specifically, the thesis study has included the impact of PBF-LB processing conditions on the as-printed microstructure and phase fractions and the resulting the nanoscale hexagonal close-packed (HCP) phase on TRIP behaviour. Employing in-situ HEXRD and comprehensive microstructural characterization, the study addressed the load distribution associated with phase transformation during tensile deformation of the alloy. The pre-alloyed spherical powder of the non-equiatomc  $\text{Co}_{45}\text{Cr}_{25}(\text{FeNi})_{30}$  with D90 of 45  $\mu\text{m}$  supplied by Höganäs AB was used in this investigations.

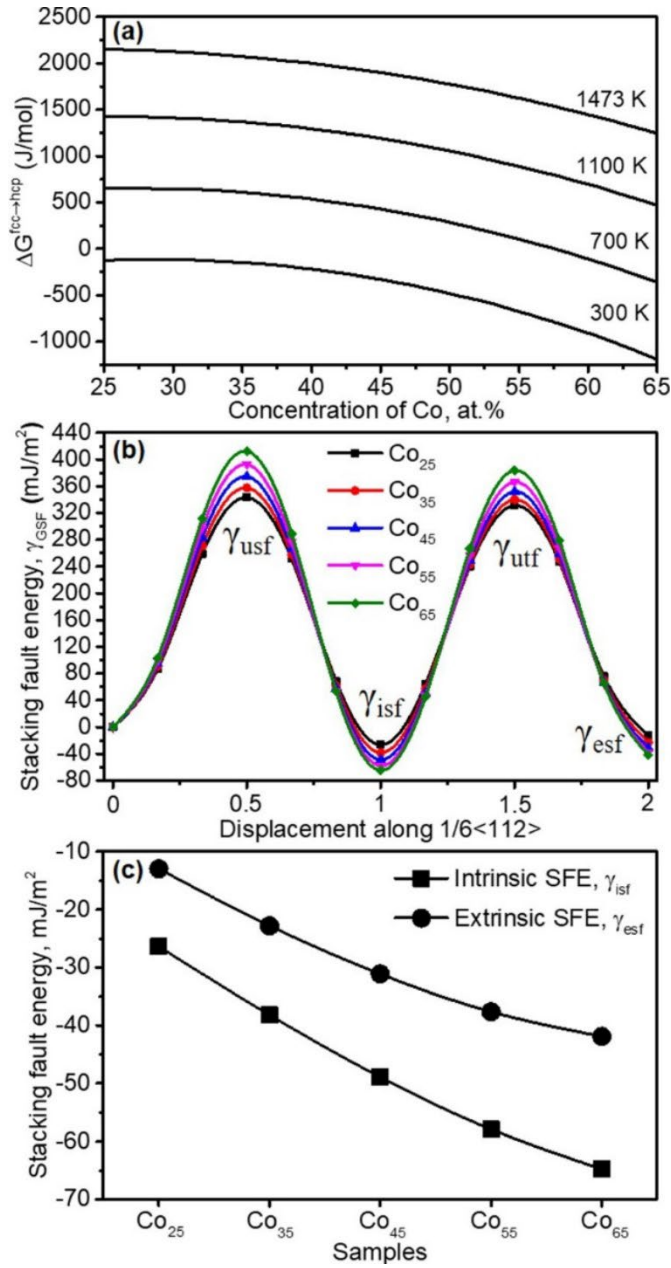


Figure 8 Influence of composition on (a) The  $\Delta G^{\text{fcc} \rightarrow \text{hcp}}$  of  $\text{Co}_x\text{Cr}_{25}(\text{FeNi})_{75-x}$  ( $x$ : 25~65) HEAs calculated by Thermo-Calc; (b) generalized-stacking fault energy of  $\{111\}\langle 112 \rangle$  slip and (c) the intrinsic and extrinsic stacking fault energies of the HEAs at 0 K calculated by DFT. reprinted by permission of Informa UK Limited, trading as Taylor & Francis Group, [www.tandfonline.com](http://www.tandfonline.com), from [117].

## 4 Methods

### 4.1 Powder bed fusion-laser beam

All the materials presented in this study are produced using EOS M100 PBF-LB machine equipped with 200W Yb-fiber laser with a spot diameter of 40  $\mu\text{m}$ . This machine features a circular build plate of 100 mm in diameter and with a maximum build height of 95 mm. Prior to the printing process, the machine is purged with 5N purity Argon gas to reduce the oxygen level in the build chamber to below 1000 ppm. All the bulk samples for the alloys presented in the study were produced using 20  $\mu\text{m}$  layer thickness, with a stripe scan strategy of 5 mm stripe width and a stripe overlap of 0.1 mm and with 67° scan rotation between subsequent layers.

Single scan tracks for all the three ferritic stainless-steel variants of 8 mm length were printed at a laser power of 110W, at a layer height of 20  $\mu\text{m}$  and at scan speeds of 600, 800, and 1200 mm/s on the substrates of 10 x 10 x 5 mm<sup>3</sup> of the same material as of single tracks.

Mixing of the alloys powder with nano-particles for selected trials was performed using two different techniques. Two different volume fractions of 80 nm size TiN particle were added to pre-alloyed CoCrNi powder. Mixing of 0.5 wt% of TiN particles was performed for 3 hours using the rotary tumbler placed inside a glove box under pure nitrogen. Mixing of 5 wt% TiN nanoparticles was performed using the ball milling process in ambient atmosphere with powder to ball ratio of 1:5 for 15 minutes. After ball milling, the mixed powder was sieved with -63  $\mu\text{m}$  mesh to remove any coarse powder and agglomerates formed during the mixing processes. The mixed powder samples were then subjected to extensive DOE to obtain the optimum processing parameters and to achieve densities >99.5%.

### 4.2 Metallographic preparation

Metallography is the study of physical structures and components of metallic materials. The goal of metallography is to examine and analyse the microstructure, focussing on the microstructural features such as grains, inclusions, and phases present in the metallic materials. Metallographic sample preparation refers to the techniques used, and the steps involved in preparation of samples for the metallography.

Metallographic sample preparation of the powder samples was performed by mixing small quantities of powder with PolyFast (Struers), a conductive mounting resin followed by hot mounting with Citopress-20 (Struers). The as-printed samples of ferritic stainless steels and CoCrNi-N MEA were also mounted in the same way as mentioned above. The mounted samples were then carefully ground using 320 grit SiC emery sheet to attain a flat surface. The ground samples were then subjected to mechanical polishing using 9  $\mu\text{m}$ , 3  $\mu\text{m}$  and 1  $\mu\text{m}$  suspended diamond solutions in sequence. These steps were followed by final polishing using colloidal suspension of silica particles ( $\sim 50\text{ nm}$ ) on an to attain a mirror like surface finish. The etching of the as-printed samples of CoCrNi-N MEAs was performed using diluted aqua regia (1:3 volume mixture of nitric acid and hydrochloric acid) to reveal the cellular solidification structure.

Heat treated samples of CoCrNi and CoCrNi-N MEAs and the as-printed samples of  $\text{Co}_{45}\text{Cr}_{25}\text{Fe}_{15}\text{Ni}_{15}$  alloy were prepared for metallography using the electrochemical polishing. The samples were initially ground with SiC emery sheets carefully starting with 500 grit all the way up to 4000 grit to get a flat surface and surface. The CoCrNi-N MEAs were subjected to electrochemical polishing using 10% perchloric acid in methanol as an electrolyte, while  $\text{Co}_{45}\text{Cr}_{25}\text{Fe}_{15}\text{Ni}_{15}$  alloy was prepared using Struers A2 electrolyte to attain a stress-free, mirror like surface finish.

### 4.3 Optical microscopy

Optical microscopy (OM) is one of the most basic, yet most useful tools in metallographic characterization. The OM uses visible light as the light source which when reflected from the sample surface, passes through a set of lenses to magnify, and form an image. Although modern microscopes have adapted a more complex design to improve the resolution and contrast of the image down to a few micrometres, the basic principle of the imaging remains the same. It is essential to note that the resolution of OM is limited due to the restricted wavelength of the visible light. This limitation is called as Abbe diffraction limit which is that the smallest resolvable limit between two points for a conventional microscope can never be smaller than the half of the wavelength for the visible light [142].

### 4.4 Scanning electron microscopy

Scanning electron microscope is one of the most resourceful tools in the field of materials science. The main difference between the OM and scanning electron

microscope (SEM) is the source of imaging, where SEM uses accelerated beam of electrons (usually between 1 keV and 30 keV). The electrons generated at cathode are focused into a spot on to the surface of the sample using a set of condenser lenses. While both visible light and electrons are part of the electromagnetic spectrum, the wavelength of the visible light is between 400 nm and 700 nm, whereas the wavelength of the electrons varies from 0.006 nm to 0.03 nm (for the acceleration voltage between 1kV and 30 kV). This results in a theoretical spatial resolution to about 0.02 nm for an electron microscope. Though the theoretical limit is significantly high, it is limited due to the electron optics reaching a practical limit of around 0.2 nm [135]. Another major difference between OM and SEM is that the electrons are strongly scattered by gases than the visible light. Hence, it is required to maintain a vacuum level of at least  $10^{-7}$  atmospheric pressure inside an electron microscope. While the lenses in the optical microscope have refractive index, which contribute to the limited resolution of the optical microscopes, the “lenses” in the electron microscopes are essentially magnetic fields and hence there is a negligible change of the refractive index as the electrons pass through each magnetic lens.

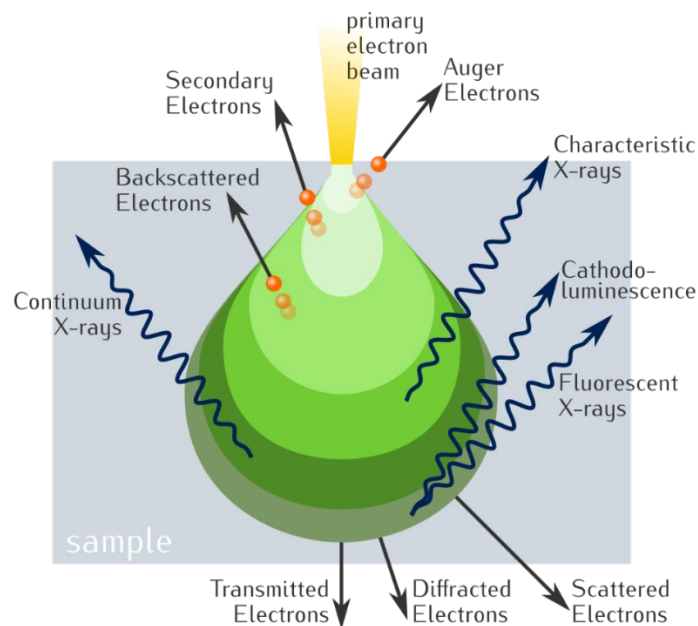


Figure 9 Origin and information of secondary electrons, backscattered electrons, Auger electrons, X-rays in the diffusion cloud for normal incidence of primary electrons [143].

When accelerated, high energy electrons interact with the material, they do so within the sample to a depth of a few micrometres (also called interaction volume) depending on the accelerating voltage and the density of the sample. The interaction between the electron beam and the sample produces elastic and inelastic collisions with the atoms

of the material and results in scattering of electrons with a wide range of energies. Depending on the type of interaction, different signals like secondary electrons (SE), backscattered electrons (BSE), diffracted backscattered electrons (EBSD), characteristic and continuum X-rays, and heat are generated. These signals are collected by one or more types of detectors. Images are generated from these collected signals and are then displayed on the screen. The representative electron-material interaction is shown in Figure 9.

Microstructural characterization of both the printed bulk samples and the powder was performed using LEO Gemini 1550 and LEO Gemini 450 field emission gun scanning electron microscopes (FEGSEM). Energy dispersive X-ray spectroscopy (EDS) was performed to analyse the elemental composition of various phases in the microstructure using X-Max EDS detector. Electron back scattered diffraction (EBSD) and transmission Kikuchi diffraction (TKD) were performed to understand the crystallographic orientation of the printed samples with respect to various building directions using Nordlys II and symmetry detectors by Oxford Instruments. The analysis of the EBSD data was performed using MTEX, an opensource MATLAB toolbox [144].

#### 4.5 Transmission electron microscopy

Similar to SEM, transmission electron microscopy (TEM) is also one of the most indispensable tools in the field of materials science. The operating principle of TEM is similar to the SEM in the sense that it uses high energy electron beam as the energy source to visualize the details of the materials. However, one significant difference is that the acceleration voltage of the electrons is typically in the range of 100 – 300 kV and the TEM uses the electrons that are transmitted through the materials. Using TEM, it is possible to achieve resolution that ~100 times higher than SEM. Hence it is possible to reveal crucial details such as crystal structure, qualitative information about the dislocation densities and etc [145].

Two most common imaging modes used in TEM are bright field and dark field imaging modes. As the electrons interact with the sample, the interaction results in various scattering phenomenon. In the bright field (BF) mode, the unscattered (transmitted) electrons are detected by the aperture while the scattered electrons are excluded. This results in the images with dark regions from where the electrons are scattered while the regions of the materials where the electrons are unscattered appear



bright. In darkfield (DF) mode, the unscattered electron beam is excluded from the aperture, while the scattered electrons are detected [145].

In the current research work, samples for TEM were prepared by using Electrical Discharge Machining (EDM) to extract samples that were 3 mm wide and roughly 1.2 mm thick. These extracted samples were then thinned down to a thickness of approximately 100  $\mu\text{m}$  by sequential grinding with minimal pressure on SiC emery sheets. Following this, the thinned samples underwent ion slicing with a JEOL EM-09100IS ion slicer, which used a low-energy argon ion beam at a 5-degree angle to remove material. The BF and DF imaging and EDS analysis were conducted in the Scanning TEM (STEM-EDS) mode using a JEOL-JEM 2100F.

#### 4.6 X-ray diffraction

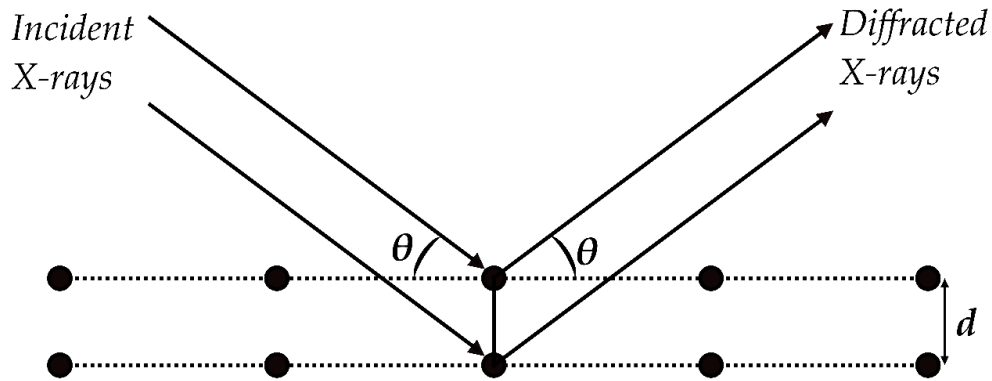


Figure 10 Schematic representation of the principle of X-ray diffraction [146].

The X-ray diffraction (XRD) is one of the most used techniques to determine the phase information, crystallinity, and texture of the materials. When X-rays from a monochromatic source of wavelength,  $\lambda$ , are impinged on to a crystalline material, the interaction results in the constructive interference as shown in Figure 10 which can be described/determined by the Bragg's law as mentioned below:

$$n\lambda = 2 * d * \sin\theta \quad (5)$$

where  $d$  is the interplanar spacing,  $\theta$  is the diffraction angle and  $n$  is the order of diffraction. The peak positions in XRD patterns represent the miller indices ( $hkl$ ) of the plane at which the constructive interference occurs [139]. The lattice parameter for cubic materials could be obtained by using the equation given below.

$$\frac{1}{d_{hkl}^2} = \frac{h^2 + k^2 + l^2}{a^2} \quad (6)$$

where  $a$  is the lattice parameter for the materials under investigation.

Lab-scale XRD techniques used X-ray tubes which produce X-rays by the interaction of accelerated electrons with a metal target as an anode (for example, Co, Cu, Cr etc.). The intensity of the X-rays produced using the lab scale X-ray sources is low and the wavelength is also fixed which depends on the anode material. In this study, the phase characterization of the materials was performed using Bruker AXS D8 Advance diffractometer equipped with a Cr K $\alpha$  source ( $\lambda = 2.28970 \text{ \AA}$ ) operated at 35 kV and 40 mA.

#### 4.7 High energy X-ray diffraction (HEXRD)

Unlike lab-scale XRD, synchrotron X-rays are produced by cyclic accelerators where the charged particles such as electrons travel at relativistic speeds. As these charged particles travel at high speeds under vacuum and are forced to change the direction under the influence of magnetic fields, they emit radiation known as synchrotron radiation. This emitted radiation extends over a broad range of the electromagnetic spectrum, from infrared light to X-rays [147]. This synchrotron radiation is incredibly bright and highly collimated, making it an excellent source of X-rays for advanced analytical techniques. The high intensity of synchrotron radiation allows for the collection of more detailed data in less time compared to lab-scale XRD and thus can be tailored to the specific needs of the experiment by using various beamline components, such as monochromators and mirrors [148]. This flexibility allows a wide variety of experiments, from high-resolution diffraction studies to detailed spectroscopic analyses.

The principle for the diffraction of the X-rays has already been discussed in the previous section. When the high energy X-rays interact with a sample with material with large number of crystallites randomly oriented in space, the constructive diffraction of the X-rays follow Braggs law of diffraction. The wavelength of the X-rays can be determined by Planck's law, given by:

$$E = \frac{hc}{\lambda} \quad (7)$$

where:

-  $E$  is the energy of the photon,

- $h$  is Planck's constant,
- $c$  is the speed of light, and
- $\lambda$  is the wavelength of the X-ray

the wave vector for the scattered radiation,  $k$  is given by the equation:

$$k = \frac{2\pi}{\lambda} \quad (8)$$

and the scattering vector in reciprocal space (as shown in Figure 11),  $q$  is given by the equation:

$$q = 2k \sin(\theta) \quad (9)$$

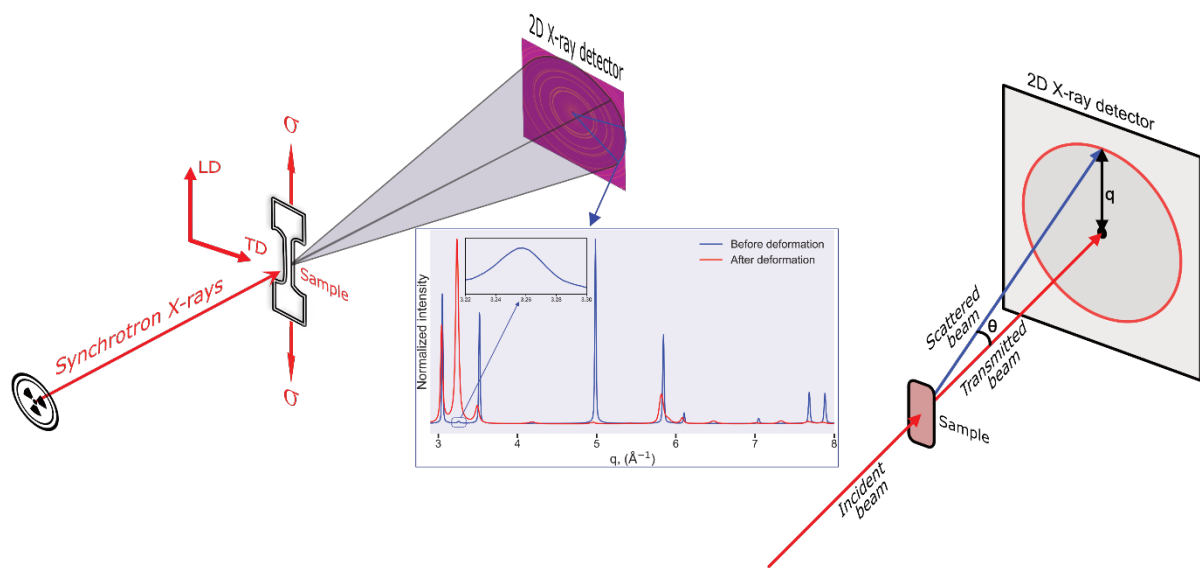


Figure 11 Schematic of the experimental set up for the in-situ tensile tests performed using HEXRD.

In-situ HEXRD tensile tests were performed on  $\text{Co}_{45}\text{Cr}_{25}(\text{FeNi})_{30}$  samples in the as-printed state to understand the deformation behaviour of the as-printed microstructure which consists of metastable FCC and nano scaled HCP phase formed due to the high cooling rates of the PBF-LB process. Miniature dogbone shaped specimens of gauge length 7 mm and thickness 1.2 mm were extracted using EDM from the as-printed samples. The extracted samples were carefully ground and polished using 50 nm silica solution to remove any deformation layer formed during the grinding stage. The tensile tests were performed in displacement control mode at an equivalent strain rate of  $2.5 \times 10^{-4} \text{ s}^{-1}$  to a maximum nominal strain of 40%. The in-situ diffraction experiments during deformation were performed at 90 keV and a spot size of  $150 \mu\text{m} \times 150 \mu\text{m}$ . The 2D diffraction patterns were obtained at a time resolution of 1 second during the deformation process. The schematic of the experimental setup is shown in the Figure 11. The 2D diffraction images were integrated across the

loading direction (LD) and transverse direction (TD) along the azimuthal ranges of  $\pm 10^\circ$  around each direction, to acquire the 1D diffraction patterns using PyFAI [149], an open-source, Python-based module for azimuthal integration [149]. The instrument calibration of the diffraction setup was performed using  $\text{CeO}_2$  (SRM 674b NIST standard). The curve fitting was performed on peaks observed in the integrated 1D patterns using an in-house developed Python-based code using lmfit library [150]. Single peak fitting was performed by identifying the peak centres and for all the peaks in a 1D pattern followed by iterative fitting of all the identified peaks using pseudo-Voigt function. This iterative peak fitting was then repeated on all the acquired 1D patterns in both transverse (TD) and loading directions (LD). Post fitting, the peak parameters such as, actual peak centres ( $q$ ), peak heights, full width at half maximum (FWHM) and other required parameters were extracted. Based on these parameters, the change in  $q$  was converted to lattice parameters. The  $d_{(hkl)}$  values for the detected reflections were determined using:

$$d_{(hkl)} = \frac{2*\pi}{q} \quad (10)$$

Where  $d_{(hkl)}$  is the lattice constant for the (hkl) reflection. The lattice strain measurements for the detected reflections were performed using:

$$strain = \frac{d_0 - d}{d} \quad (11)$$

where,  $d_0$  is the lattice spacing for the reflections in the initial state and  $d$  is the lattice spacing at the stressed state. It was assumed that, in the initial state, any residual stresses were relaxed during the sample preparation stage.

Rietveld refinement was performed on the extracted 1D profiles using the GSAS II [151] software. The initial refinement was performed on the lattice parameters and texture distribution of the final profile, considering both HCP and FCC phases. The phase fractions were estimated from EBSD results, and the peak broadening was fitted using the isotropic macrostrain model. Sequential refinements were performed on all test profiles, starting from the final profile at 40% normal strain. During the sequential refinement, the phase fractions, micro strains, hydrostatic and elastic strains, and texture parameters were refined.

## 4.8 Hardness

The hardness of a material, defined as the *resistance of the material to deformation* and is one of the most fundamental properties to assess the mechanical behaviour of the materials. Vickers hardness is one of the indentation hardness techniques which uses a diamond indenter shaped in the form of an inverted pyramid with 136° angle between the opposite faces. Once the material is indented using a predetermined load (L), the length of the diagonals is measured, and the hardness is calculated using the following equation:

$$HV = \frac{L}{A} = \frac{1.8544L}{d^2} \quad (12)$$

where d is the average length of the two diagonals of the indent.

Vickers hardness measurements for the materials used in the study were performed using Struers Durascan-70 G5 at 5 kgf load for 15 s of dwell time. The hardness values were taken in both building and transverse directions of the printed samples to measure the anisotropy with respect to different directions.

## 4.9 Tensile testing

Tensile tests were performed on both as-printed and heat-treated samples presented in this study to understand the mechanical response of the resulting microstructures.

Tensile samples for both the as-printed and heat-treated states of CoCrNi-N alloys were prepared using wire arc EDM, with a gauge length of 8 mm, a thickness of 1.2 mm, and a width of 2 mm within the gauge section. The extracted samples were the carefully ground using SiC emery sheets starting from 800 grit all the way up to 4000 grit to attain a flat surface. Tensile tests were conducted using the SHIMADZU AG-100kN Xplus machine in displacement control mode, corresponding to a strain rate of  $1 \times 10^{-3} \text{ s}^{-1}$ . The deformation during the tensile tests was recorded using a high-resolution camera, capturing images at 5 frame per second (fps). Strain analysis was performed on the acquired images using digital image correlation (Vic-2D, Correlated Solutions). To ensure consistency in the observed tensile properties of the alloys, at least three samples were tested for all the selected conditions.

Tensile samples of gauge length 4 mm, 1.2 mm thickness and a width of 2 mm were extracted using wire arc EDM from as-printed samples of  $\text{Co}_{45}\text{Cr}_{25}(\text{FeNi})_{30}$  for ex-situ testing to obtain the bulk mechanical properties. At least three samples were tested in

displacement control mode corresponding to a strain rate of  $2.5 \times 10^{-4} \text{ s}^{-1}$  for each condition.

#### 4.10 Thermodynamic calculations

Thermodynamic calculations were performed using Thermo-Calc, a commercial CALPHAD (CALculation of PHase Diagram) software, using TCHEA4 database for HEAs and TCFE10 database for ferritic steels. With the help of thermodynamic calculations, the potential phase fractions for the alloys used in this study were predicted and the alloy compositions for ferritic stainless steel were tweaked accordingly to reduce the probability of formation of detrimental phases.

Scheil solidification simulations were performed to predict the solidification pathway for the alloys and obtain an understanding about the elemental segregation during solidification for various alloys presented in this study. Precipitation calculations were performed to understand the heat treatment response of the CoCrNi-N MEAs and to predict the formation of nitrogen rich phases which could deplete the interstitial nitrogen and hence be detrimental for the properties of the alloys.

## 5 Summary of results

### 5.1 Inoculation in ferritic stainless steels

Three different variants of ferritic stainless steels based on SS441 were used in order to i) maximise the amount of titanium and nitrogen available for the formation of TiN particles prior to the solidification of ferrite matrix and ii) minimize the formation of intermetallic phases Laves ( $\text{Fe}_2(\text{Ti},\text{Nb})$ ) and  $\sigma$ -phase which could potentially be detrimental to the mechanical performance of the materials (Table 1 and Figure 5 ). All the three materials were printed with the same set of printing parameters and the orientation maps obtained from EBSD analysis of the as-printed materials x-y and x-z orientations are shown in the Figure 12 below.

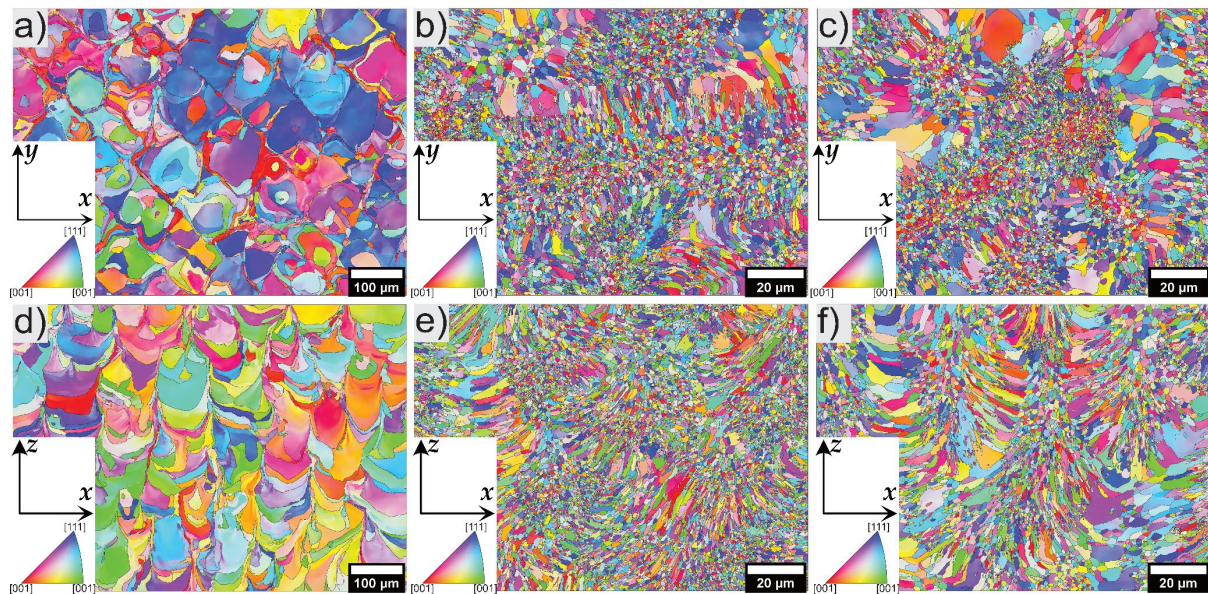


Figure 12 EBSD orientation maps of Ti-free (a, d), SS441 (b, e), and Ti-high (c, f) materials in x-y and x-z orientations[152].

Comparing all the three materials with respect to different building directions, it is clear that SS441 and Ti-high materials showed completely different microstructure compared to the Ti-free material. The Ti-free material has epitaxially grown large columnar grains as viewed along the x-z orientation and similar large grains spanning across few scan tracks as seen from the x-y orientation, which is typical to for PBF-LB process conditions. For SS441 (Figure 12 b, e) and Ti-high variant (Figure 12 c, f), the microstructures show mixture of fine equiaxed grains and some long columnar grains. The average grains sizes measured from EBSD data for Ti-free material is  $\sim 14 \mu\text{m}$  whereas for both SS441 and Ti-high materials the average grain size is  $\sim 1 \mu\text{m}$ . Figure 13 shows the inverse pole figure for the Ti-free variant, SS441 and the Ti-high variant.



The influence of titanium content is also clear in terms of the texture between these two materials with Ti-free materials showing  $\langle 001 \rangle$  preferred orientation in building direction, while SS441 and Ti-high materials show  $\langle 111 \rangle$  preferred orientation. This difference in texture indicates difference in the solidification behaviour between Ti-free variant compared to S441 and Ti-high variant. It should be noted that the overall macroscopic thermal gradient is the same, but locally the solidification behaviour is different.

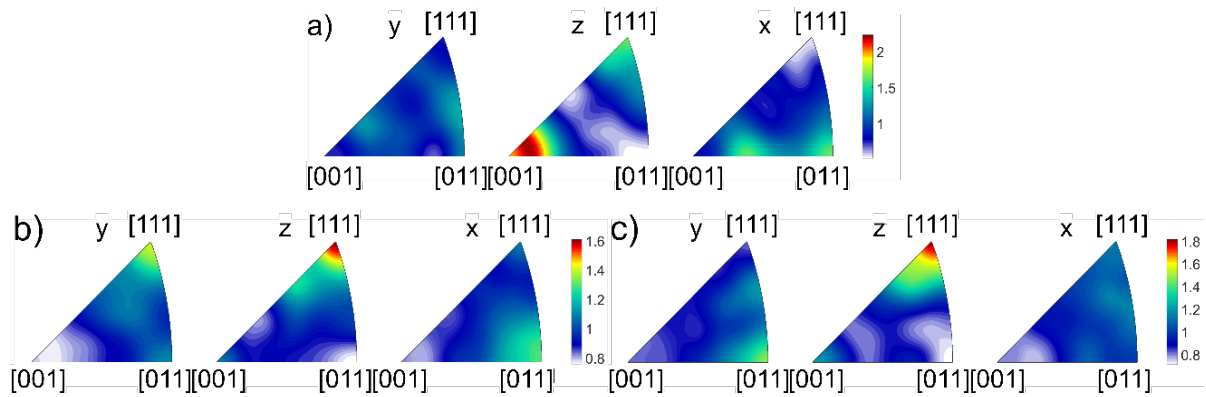


Figure 13 Inverse pole figures for a) Ti-free, b) SS441 and c) Ti-high materials in x-z orientation [152].

For an inoculate to be effective, this should have:

- i) low lattice mismatch with the matrix and
- ii) should be able to induce wetting of the nucleating solid effectively [36].

Apart from the above-mentioned points, for an inoculant to be effective, number density and size of the inoculant particles are also of utmost important [41,43]. Titanium nitride is known to be one of the most effective inoculates for the ferritic steels due to low lattice mismatch and better wetting of the ferrite in the cast alloys [61,153,154].

Microstructural analysis revealed distribution of various particle in all the three materials (Figure 14 a, b, c). The EDS analysis of particles in Ti-free (Figure 14 d) material revealed the presence of spherical Al-Si oxides. The SS441 and Ti-high materials (e and f) showed distribution of pure nitrides of titanium and core-shell structured oxy-nitrides with aluminium-rich oxide core and titanium nitride shell. Though there is a clear influence of titanium addition on the solidification behaviour and grain refinement of these alloys, a mixture of columnar and equiaxed grains is observed in for both SS441 and Ti-high variant.



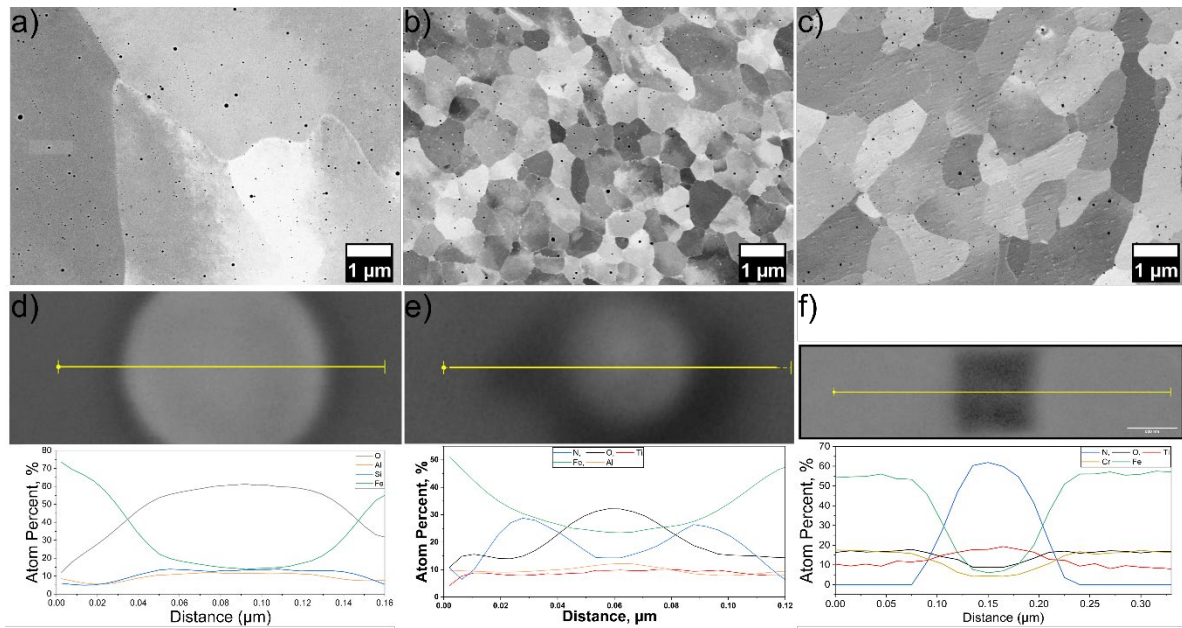


Figure 14 SEM backscattered electron images of a) Ti-free b) SS4541 and c) Ti-high material showing distribution of particles inside the matrix and EDS analysis of the particles in d) Ti free material showing Al-Si oxides, e) core-shell type oxy-nitride particles and f) Pure nitride particles in SS441 and Ti-high materials[152].

In order to get a better understanding of the efficiency of the TiN as an inoculant for the PBF-LB process conditions, it is necessary to get an understanding of the distribution of TiN particles inside the matrix. Automated feature analysis of the particles combined with EDS was performed for the equiaxed and columnar regions of for SS441 and Ti-free materials and the size distribution is shown in Figure 15. It is clear from Figure 15a that the number of particles in the equiaxed region are much higher than that for the columnar region. Though the average size of particles in both equiaxed and columnar region is very similar being  $\sim 39$  nm, the number density of particles in columnar region is  $0.3 \mu\text{m}^{-2}$  whereas for the equiaxed region it is  $1.2 \mu\text{m}^{-2}$ . If we consider the solidification at melt pool scale, at the bottom of the melt pools,  $G$  is high, and  $V$  is low resulting in conditions favourable for columnar growth. In order to promote CET in this columnar regions, the required number density and size of the inoculating particles must be higher to achieve undercooling required to promote the formation of equiaxed grains. At the centre of the meltpools on the other hand,  $G$  is low, and  $V$  is high. A schematic of different thermal conditions within one meltpool and its resulting influence on the grain morphology is presented in Figure 15b. The conditions are more favourable for the formation of equiaxed grains. Also, at the centre of the melt pools, the alloy stays molten for relatively longer periods compared to the edges of the meltpools, thereby providing more time for the nucleation and growth of inoculant particles resulting in the equiaxed grains.

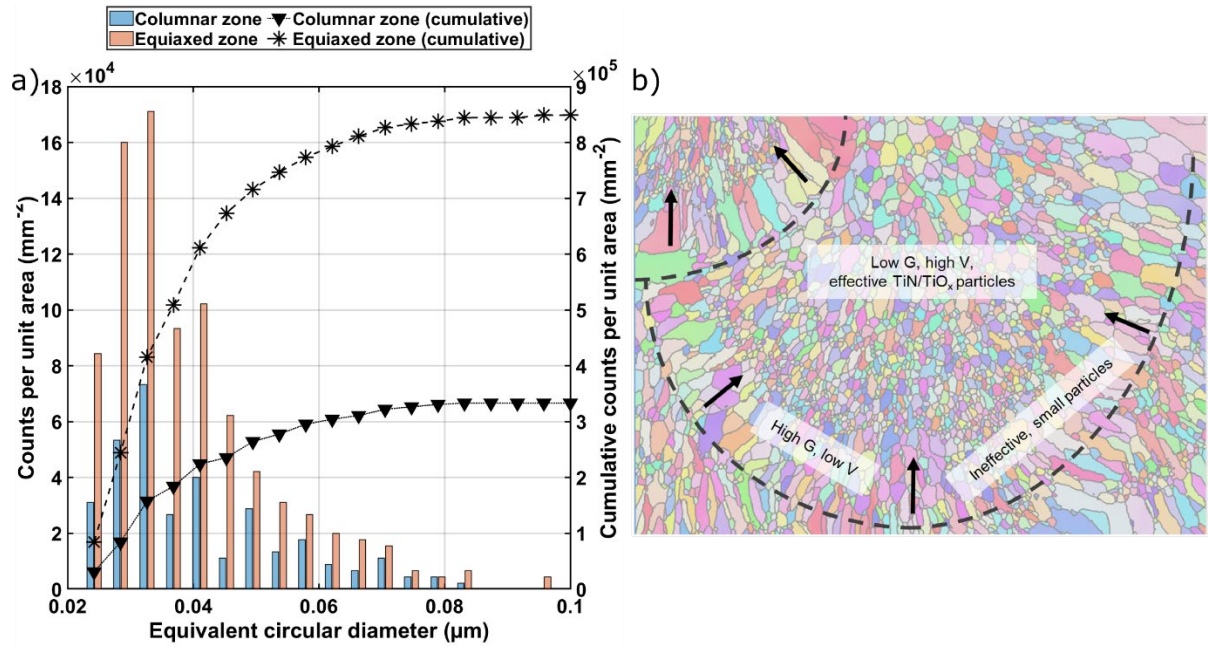


Figure 15 a) Particle size distributions obtained from feature analysis showing the size distribution of particles in columnar and equiaxed region[152] and b) Schematic showing the difference in the  $G$  and  $V$  at different regions of the melt pools that influence the grain morphology[13].

## 5.2 Influence of printing parameters on microstructure of ferritic stainless steels

As mentioned in the previous section, the concept of in-situ inoculation has been very effective in terms of influencing the solidification conditions resulting in the 10-fold reduction grain size for the inoculated materials. However, the microstructure still consists of mixture of equiaxed and columnar grains. It is well reported that in PBF-LB, manipulation of process parameters alone could result in the formation if equiaxed grain structures [18–20]. Specifically, either increase in laser power or increase in scan speed are reported to influence the resulting  $G$  and  $V$  during the solidification within the melt pools resulting in the reduction of grain size. In order to understand the influence of the printing parameters on the resulting grain morphology, 10-layer high single tracks were printed at scan speeds of 600 mm/s, 800 mm/s and 1000 mm/s at a constant laser power of 110W and layer thickness of 20 μm for the Ti-free, SS441 and Ti-high materials. The resulting grain size distribution of single tracks in comparison with the bulk materials is shown in Figure 16.

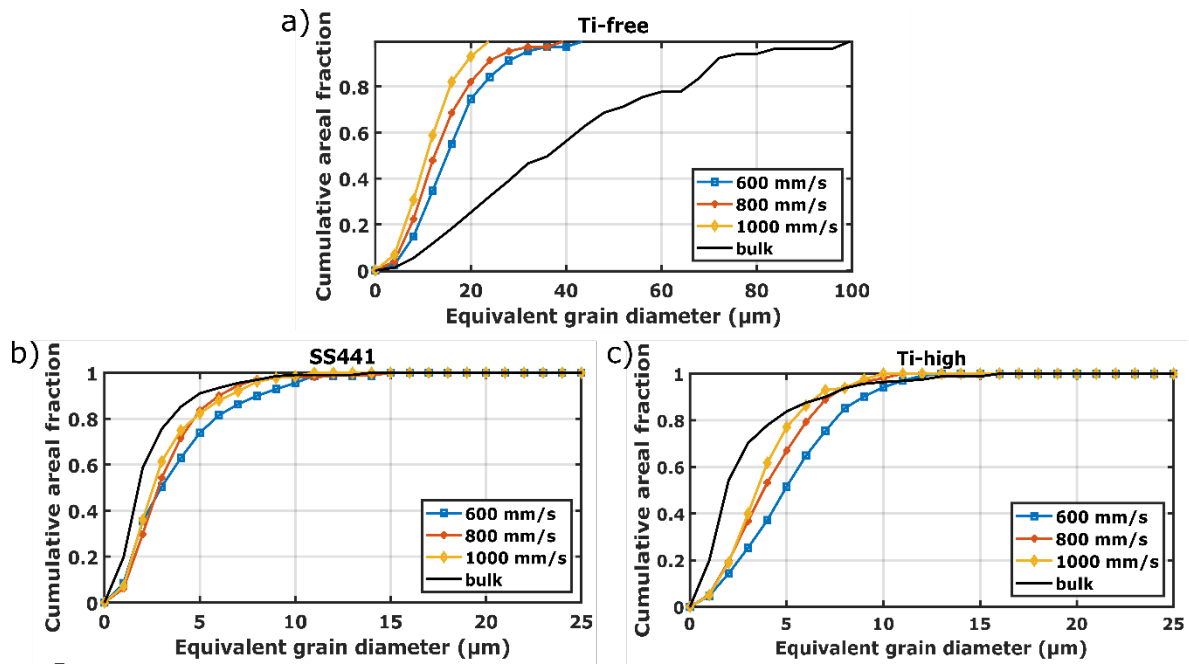


Figure 16 Grain size distribution plots for a) Ti-free, b) SS441 and c) Ti-high materials showing the distribution of grain size as a function of scan speeds in single tracks in comparison with the bulk samples of their respective materials[152].

A similar trend is observed from the grain size distribution plots for the single tracks for all the three materials. Tracks printed at high scan speeds showed finer grain size distributions relative to the tracks printed at the low scan speeds. With the variation in the scan speeds, the amount of energy input into the material during the printing varies. At constant laser power, slower scan speeds result in larger heat input per unit time resulting in formation of keyhole shaped meltpools and hence slower cooling rates during solidification and with increase in scan speeds the cooling rate also increases. Higher cooling rates result in the formation of finer grain morphologies. However, printing at higher scan speeds also result in formation of narrow tracks which needs to be compensated by reducing the hatch distance.

Comparing the grain sizes between single tracks and bulk samples, bulk samples of Ti-free material showed coarser grain size distribution compared to its single tracks. This is because, in the absence of the inoculation in Ti-free material, the remelting due to the layer-by-layer printing results in the epitaxial growth of columnar grains which is typical in PBF-LB. However, for SS441 and Ti-high materials, grain size distribution in bulk samples is observed to be finer compared to the all the single tracks. This is because, the remelting which is a result of both layer-by-layer bulk printing and the consecutive hatches provides sufficient time for the nucleation and growth of

inoculant particles in terms of their size and number density resulting in reduced undercooling required for CET.

### 5.3 Influence of nitrogen doping on microstructure and properties of CoCrNi medium entropy alloy

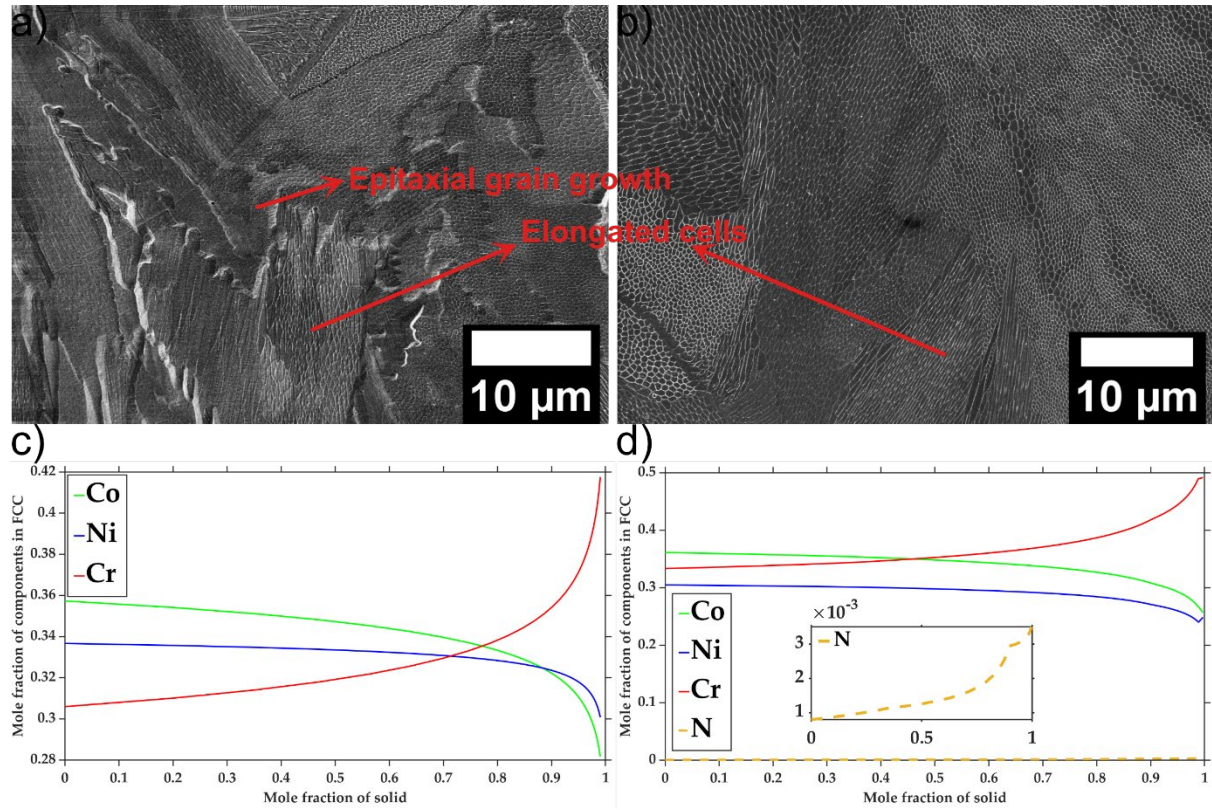


Figure 17 a) As printing microstructure of a) CoCrNi and b) CoCrNi-N MEA showing the cellular solidification structures and Scheil solidification simulations showing elemental segregation for c) CoCrNi and d) CoCrNi-N along with magnified inset for nitrogen segregation.

Influence of nitrogen addition to CoCrNi with an aim of achieving interstitial solid solution strengthening from nitrogen, and its influence on the microstructure, room temperature mechanical properties and corrosion and passivation behaviour was studied. Two different alloys, one with pre-alloyed nitrogen and another without nitrogen was studied and the elemental compositions of alloy powder and as-printed samples for both alloy variants are shown in Table 2. No detrimental phases were observed in the as-printed samples and microstructural analysis revealed cellular solidification structure in both CoCrNi and CoCrNi-N (Figure 17 a and b, respectively). Scheil solidification simulations predicted elemental segregation of chromium in CoCrNi (Figure 17 c) and nitrogen along with chromium into the cell walls in the CoCrNi-N MEA (Figure 17 d).



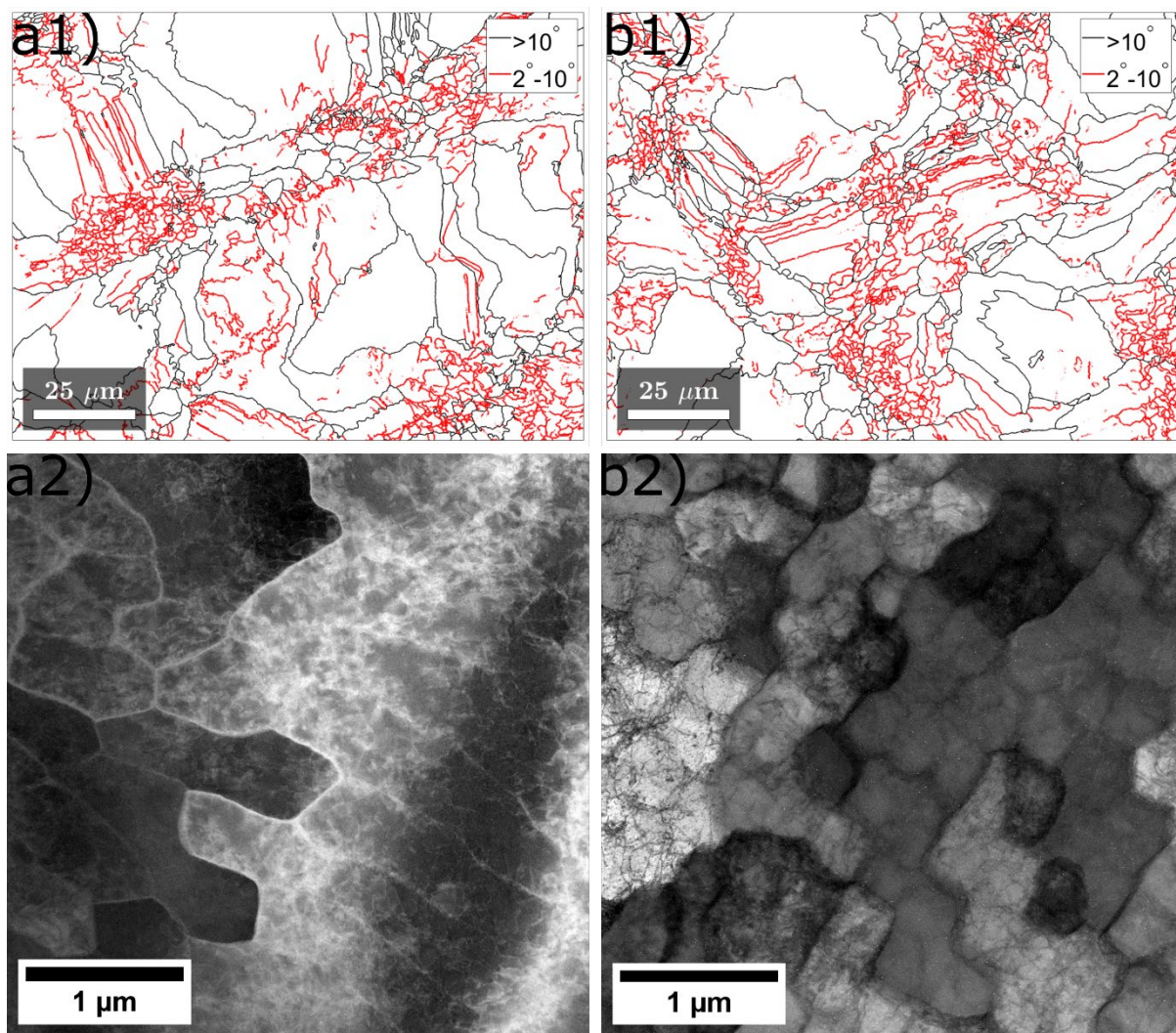


Figure 18 a1 and b1) EBSD grain boundary maps of as-printed CoCrNi and CoCrNi-N, respectively, showing the distribution of low angle ( $2^{\circ}$ - $10^{\circ}$ , marked in red) and high angle grain boundaries ( $>10^{\circ}$ , marked in black), STEM bright field images of a2) CoCrNi and b2) CoCrNi-N alloys showing the network of dislocation cells.

Along with the cellular solidification structure, STEM and EBSD analysis revealed the presence of high density of dislocation cells as shown in Figure 18 a2 and b2. This formation of this high density of dislocation cells is also an inherent characteristic of PBF-LB owing to the subsequent thermal cycling arising from the printing layer by layer building process. Figure 18 a1 and b1 shows the grain boundary maps plotted from the EBSD data for CoCrNi and CoCrNi-N, respectively. High angle grain boundaries with misorientation greater than  $10^{\circ}$  are indicated by black lines and the low angle boundaries with misorientation angles between  $2^{\circ}$  and  $10^{\circ}$  are indicated by the red lines; the density of the latter correspond closely to the cellular dislocation colonies. Within the cellular dislocation colonies, the change in misorientation is observed to be less than  $2^{\circ}$ . The STEM bright field images of such colonies in both CoCrNi and CoCrNi-N revealed the presence of dislocation cells (see Figures 18 a2

and b2). This hierarchical structure with varying degree of misorientation and high density of dislocation cells arise from the subsequent thermal cycling inherent in the layer-by-layer printing process [155–158]. This thermal cycling induces local thermal stresses in the alloy, contributing to the formation of dislocations within the cellular microstructure. The observed hierarchical microstructures were similar for both CoCrNi and CoCrNi-N as both alloys were printed using the same printing parameters. Hence, the pre-alloying with nitrogen does not induce any significant influence on dislocation density obtained during the printing process.

Thermodynamic calculations for CoCrNi-N predicted that nucleation of Cr<sub>2</sub>N should happen between 800 and 1200°C. To understand the nucleation behaviour of Cr<sub>2</sub>N which could potentially deplete the nitrogen as an interstitial strengthener, as-printed samples were therefore heat-treated for 30 mins at different temperatures ranging between 800 and 1200°C. The as-printed material does not show the presence of any secondary phase particles (see Figure 19a and Figure 20a) apart from some primary oxides that were formed during the printing process or possibly originating from the metal powder. After heat treatment at 800°C, the nucleation of particles was observed mainly at the cell boundaries in both CoCrNi and CoCrNi-N (see Figure 19b and Figure 20b, respectively). Particles were observed to grow with increase in the heat treatment temperatures for both CoCrNi and CoCrNi-N samples (see Figure 19 c-d and Figure 20 c-d) with no significant influence on the general microstructure of the alloy. The samples heat treated at 1200°C, showed recrystallized microstructure with particles of different morphologies (see Figure 19e and Figure 20e). The EDS analysis of the particles revealed that all the particles are chromium-rich oxides, while no nitrides were observed (Figure 21 a-c). Though the nucleation of Cr<sub>2</sub>N precipitates was predicted by the thermodynamic calculations and has also been experimentally observed in wrought alloys [139], these were not observed for the alloys manufactured using PBF-LB. This could be because the driving force required for the diffusion of the elements is lower as compared to the cold rolled specimens due to the lower stored energy coming from lower dislocation densities. Still, it is clear that the heat treatment as such seem to trigger the formation of small internal oxides, that were not observed in as-printed condition.

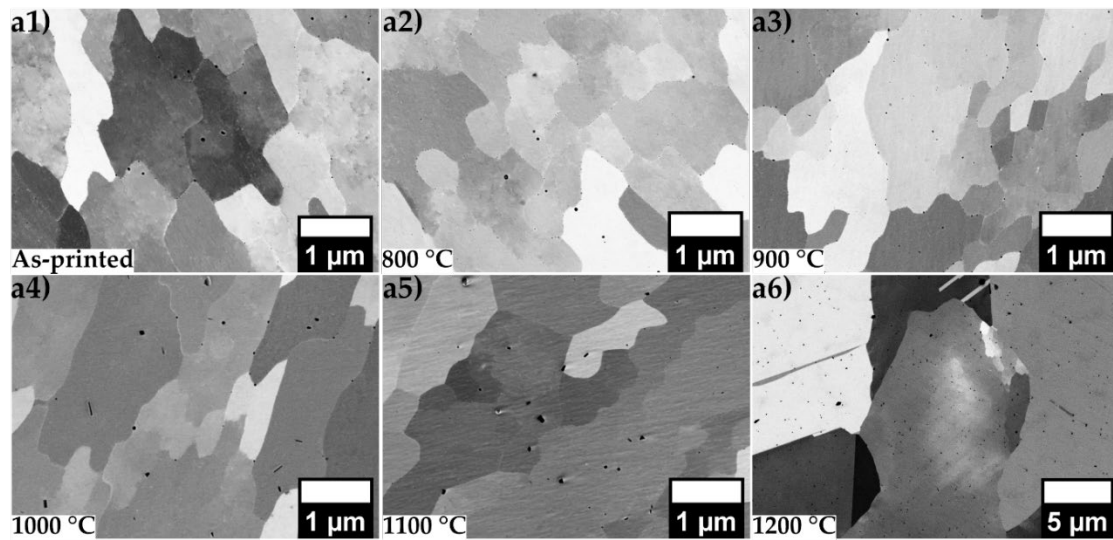


Figure 19 SEM back scattered electron images of CoCrNi samples in a1) as-printed state, a2-a6) heat-treated at 800, 900, 1000, 1100 and 1200°C.

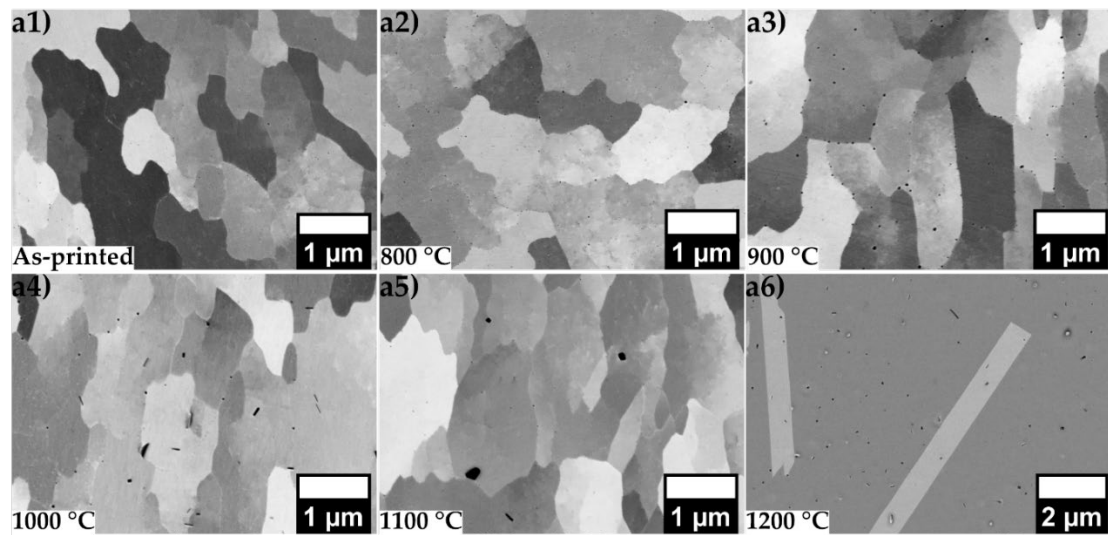


Figure 20 SEM back scattered electron images of CoCrNi-N samples in a1) as-printed state, a2-a6) heat-treated at 800, 900, 1000, 1100 and 1200°C.

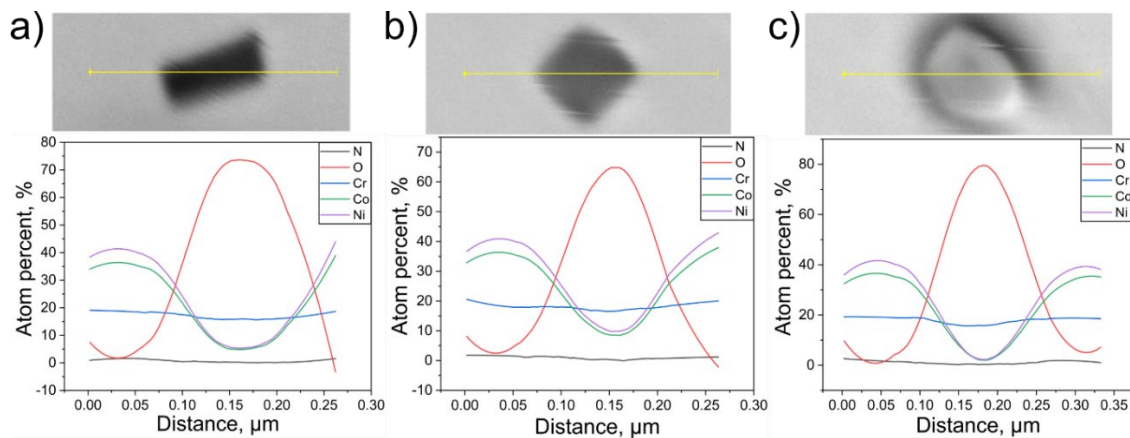


Figure 21 SEM- EDS analysis of particles in the CoCrNi-N that was heat-treated at 1200°C.



### 5.3.1 Properties of CoCrNi and CoCrNi-N MEAs

Figure 22a shows the as-printed tensile properties of CoCrNi and CoCrNi-N and a table summarizing the mechanical properties measured from the tensile tests. Addition of nitrogen to the CoCrNi led to significant improvement in both yield strength and ultimate tensile strength of the alloy in both the printing directions albeit with slight loss in ductility. Hardness of the as-printed and heat-treated samples showed ~35 HV hardness difference between CoCrNi-N and CoCrNi samples (Figure 22b). Significant drop in the hardness was observed post recrystallization in both the alloys after heat treatments at 1200°C. Based on the microstructural analysis and relative difference in the hardness in as-printed and heat-treated samples between both CoCrNi and CoCrNi-N MEAs, it could be inferred that nitrogen is stable as an interstitial.

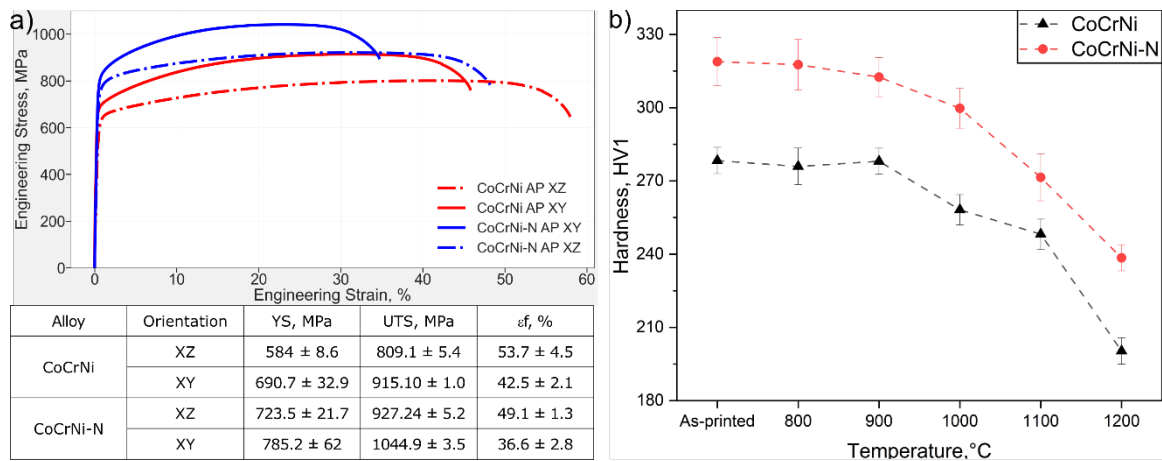


Figure 22 a) Engineering stress strain curves of CoCrNi and CoCrNi-N in as-printed state and b) hardness plots of as-printed and samples heat treated for 30 minutes at various temperatures for CoCrNi and CoCrNi-N MEAs and the table summarizing the tensile properties of the as-printed samples.

The TiN nano particles with average particle size of 80 nm were added to CoCrNi alloy in order to enable a metal matrix composite like strengthening of the alloy produced through PBF-LB. The process of mixing did not show any negative influence on the flow behaviour and final particle size distribution with 0.5 wt% TiN addition while the further increase in the TiN fraction to 5 wt% showed a bimodal distribution with a small secondary peak observed around 2 and 8  $\mu\text{m}$  indicating the agglomeration of the TiN nano particles. The addition of 0.5 wt% of TiN did not have any significant influence on the relative density, which was measured to be >99.9%. With increase in the TiN content to 5 wt%, the resulting maximum final relative density of 99.6% was achieved. The influence of this agglomeration observed for the powder with 5 wt% TiN addition can be seen in the average TiN particle size in the



as-printed microstructures. The average TiN particle size in the as-printed microstructure for 0.5 TiN addition is about 80 nm (similar to the original size of the TiN particles) while the average TiN particle size for 5 wt% TiN addition is about 140 nm. The difference between the as-printed states of CoCrNi and various TiN additions can be clearly seen in Figure 23 a-c. The mechanical response of the TiN addition to the CoCrNi alloy was studied using hardness measurements as shown in Figure 23d. With 0.5 wt% TiN addition, increase in hardness of ~30 HV1 was observed as compared to the as-printed state of CoCrNi. This level of hardness increase is similar to that observed with the 0.11 wt% nitrogen addition by pre-alloying, see Figure 22. With further increase in the TiN content to 5 wt%, the hardness value increased to 357 HV1, which is ~80 HV higher than the CoCrNi in as-printed state. These results demonstrate that PBF-LB can be a promising technique to manufacture MMC-based alloys with improved mechanical properties.

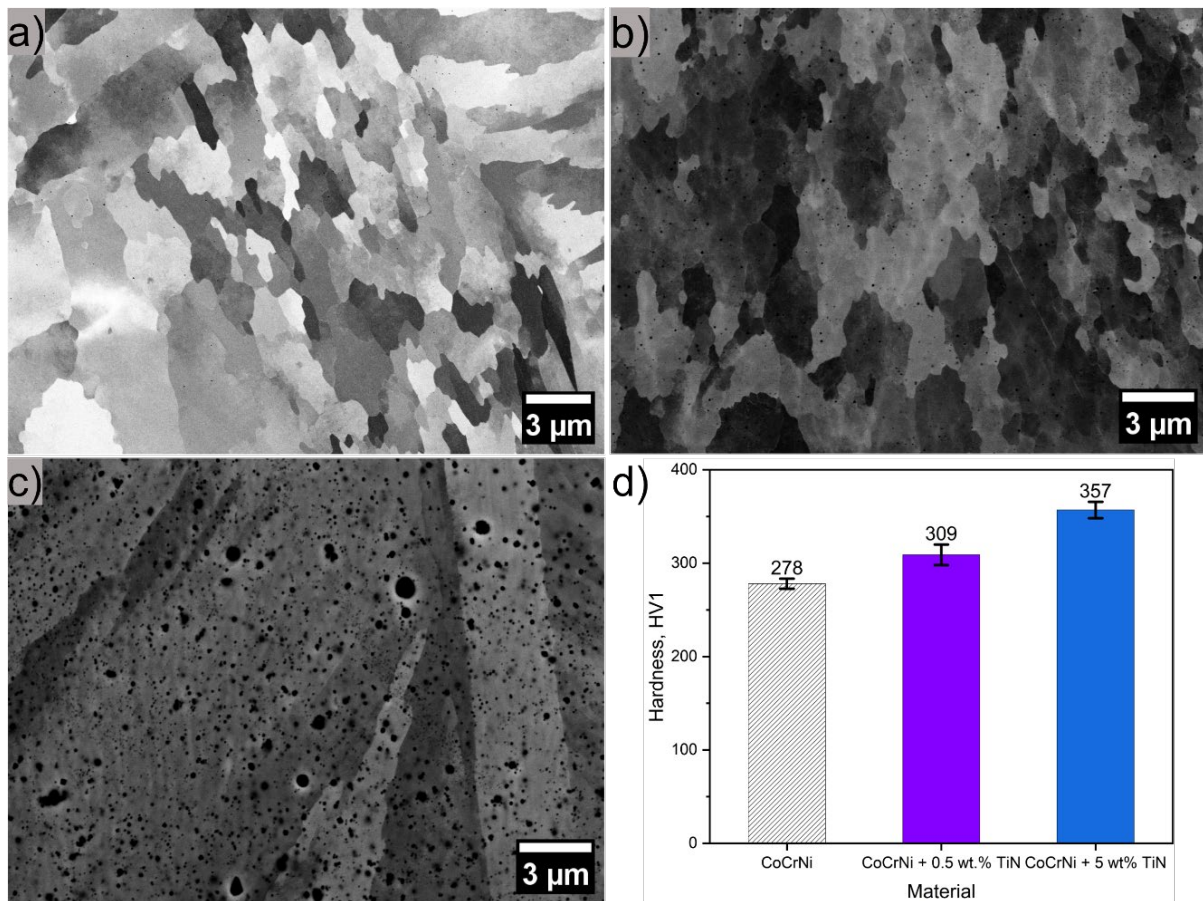


Figure 23 SEM backscattered electron images of as-printed samples of a) CoCrNi, b) CoCrNi -0.5 wt% TiN and c) CoCrNi -5 wt% TiN samples and d) PSD of TiN particles in both TiN containing materials as measured from the feature analysis[159].

### 5.3.2 Corrosion and passivation behaviour of CoCrNi and CoCrNi-N MEAs

The corrosion properties of CoCrNi and CoCrNi-N MEAs were measured using potentiodynamic polarisation measurements in 0.5 M H<sub>2</sub>SO<sub>4</sub> and 0.5 M H<sub>2</sub>SO<sub>4</sub> + 3 wt.% NaCl. The alloys were benchmarked against 316L manufactured using PBF-LB as well wrought 316L. In both the acidic and saline environments, MEAs showed better corrosion resistance when compared to 316L (see Figure 24 a and b). Both alloys when tested in 0.5 M H<sub>2</sub>SO<sub>4</sub>, showed pseudo passivation behaviour but when tested in 0.5 M H<sub>2</sub>SO<sub>4</sub> + NaCl showed clear passivation behaviour.

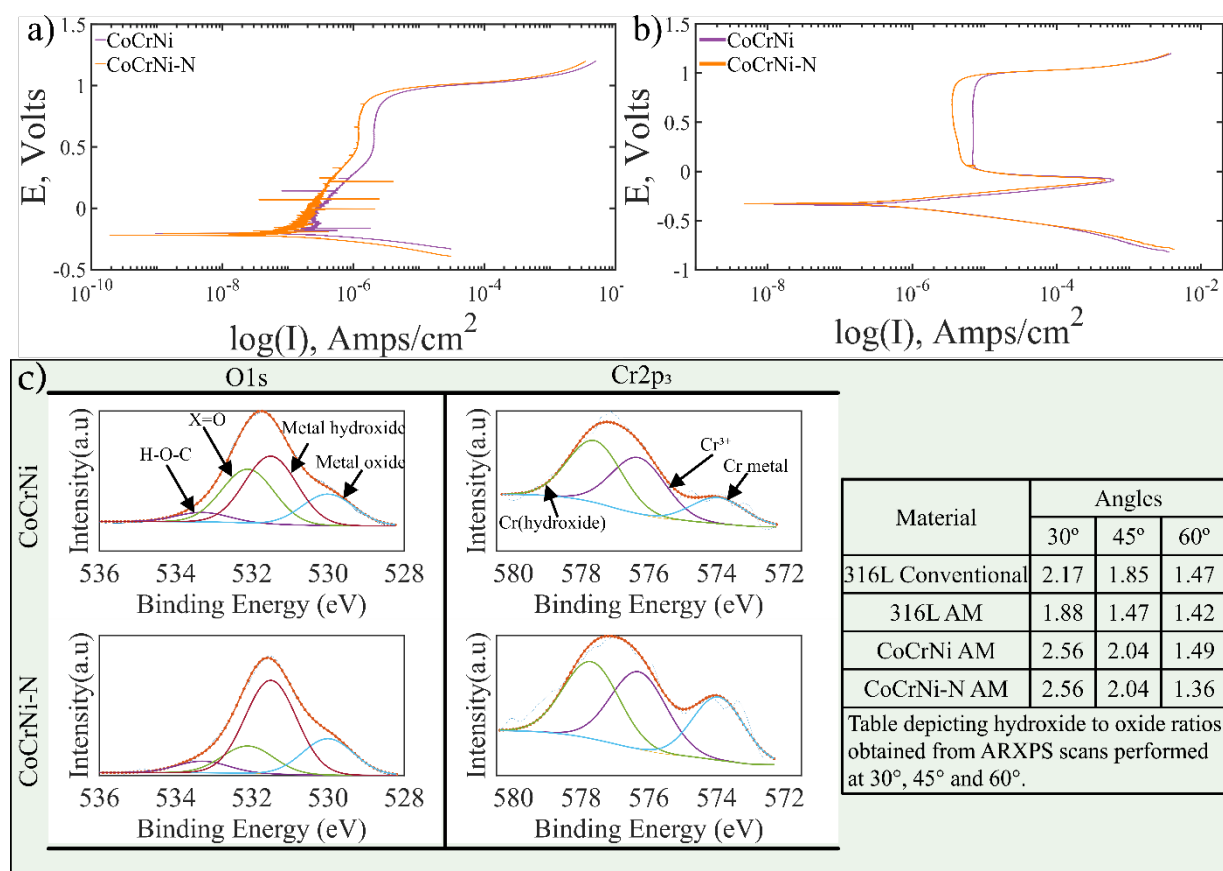


Figure 24 Potentiodynamic polarization plots for CoCrNi and CoCrNi (a) 0.5 M H<sub>2</sub>SO<sub>4</sub> (b) 0.5 M H<sub>2</sub>SO<sub>4</sub> + 3 wt.% NaCl (c) ARXPS spectra for CoCrNi and CoCrNi-N showing the original spectra and curve fitting for O1s and Cr2p<sub>3</sub> peaks performed at a take-off angle of 60°, and a table depicting the hydroxide to oxide ratios obtained from AR-XPS scans performed at 30°, 45° and 60° and X in the O1s peak corresponds to fitting of both C=O and S=O[136].

To understand the passivation behaviour, angle-resolved XPS (ARXPS) was performed with take-off angles 30°, 45° and 60° on both CoCrNi and CoCrNi-N samples. This was done after the passivation in 0.5 M H<sub>2</sub>SO<sub>4</sub> + 3 wt.% NaCl between the -0.5 (vs. E<sub>OCP</sub>) and 0.5V (vs. E<sub>OCP</sub>). The idea behind this is that having a passive condition would not significantly change the surface when handled in air prior to XPS

analysis. The results of curve fitting performed for the Cr2p<sub>3</sub> and O1s spectra along with depicted hydroxide to oxide ratios acquired with take-off angle 60° are shown in Figure 24c. The absence of cobalt and nickel peaks at any take-off angle suggests that the passive film is composed of Cr-oxide. Also, since neither Ni nor Co is shown in metallic state as well, this tells that the passive film is sufficiently thick to conceal the presence of these elements. The Cr peaks in oxide state were observed for both CoCrNi and CoCrNi-N alloys, confirming that the passive film is Cr-based, and this is expected to contribute to the corrosion resistance of alloys. While nitrogen in the alloy could be expected to enhance corrosion resistance of CoCrNi owing to passive film with a lower hydroxide-to-oxide ratio[134], the ARXPS data revealed similar hydroxide-to-oxide ratios for both CoCrNi and CoCrNi-N alloys, even with 0.11 wt% nitrogen present in the as-printed state. In conclusion, when compared to conventional as well as PBF-LB 316L, both MEAs exhibited significantly superior passivation behaviour, leading to improved corrosion resistance.

#### 5.4 Recrystallization behaviour of CoCrNi-N MEA

In order to understand the high temperature and long-term stability of nitrogen as an interstitial and the stability of the as-printed microstructure of the nitrogen-containing alloy in particular, long-term isothermal heat treatments were performed for both alloys at temperatures of 800, 900 and 1000°C for 24, 48, 96 and 192 hours. After heat treatments at 800°C, even after 192 hours, no difference in microstructure was observed when compared to the as-printed state. However, both CoCrNi and CoCrNi-N showed very high-density of fine oxide particles distributed across the matrix. These were not observed in the as-printed conditions. In case of CoCrNi-N, we also observed that there was the precipitation of ~1 µm sized particles rich in Cr and N across the grain boundaries after heat treatments at 800°C for 192 hours.

Figure 25 shows the BSE SEM images of the CoCrNi (see Figure 25 a1 -a4) and CoCrNi-N (see Figure 25 b1 -b4) samples heat treated at 900°C for different heat treatment times. After heat treatment at 900°C for 24 hours, no significant changes were observed in the microstructures of both CoCrNi and CoCrNi-N alloys. Both alloys showed high density of oxide particles, similar to the results at 800°C. However, when heat treated for 48 and 96 hours, recrystallized grains were observed in both alloys. The CoCrNi variant showed a significantly higher fraction of recrystallized grains compared to the CoCrNi-N variant. Recrystallization was first observed in both alloys

after 48 hours at 900°C and the fraction of recrystallized grains increased with longer heat treatment times (up to 192 hours). The EBSD analysis of both alloys heat treated at 900°C for 192 hours showed significant differences in the fraction of recrystallized grains, with CoCrNi showing a significantly higher fraction than CoCrNi-N. The recrystallized fractions measured from the EBSD analysis for the heat treatments at 800, 900 and 1000°C for all the heat treatment times are summarized in Figure 27. In CoCrNi-N, segregation and formation of Cr and N rich phases was observed at the grain boundaries with size of approximately 10  $\mu\text{m}$ .

Further increase in the heat treatment temperature from 900°C to 1000°C, CoCrNi-N showed lower recrystallization fractions as compared to CoCrNi similar to the previous observations. Though the difference in the recrystallization fractions among both the alloys is less significant as compared to the heat treatments after 900°C, the consistently low recrystallization fractions in CoCrNi-N suggest that nitrogen has significant influence on the recrystallization behaviour.



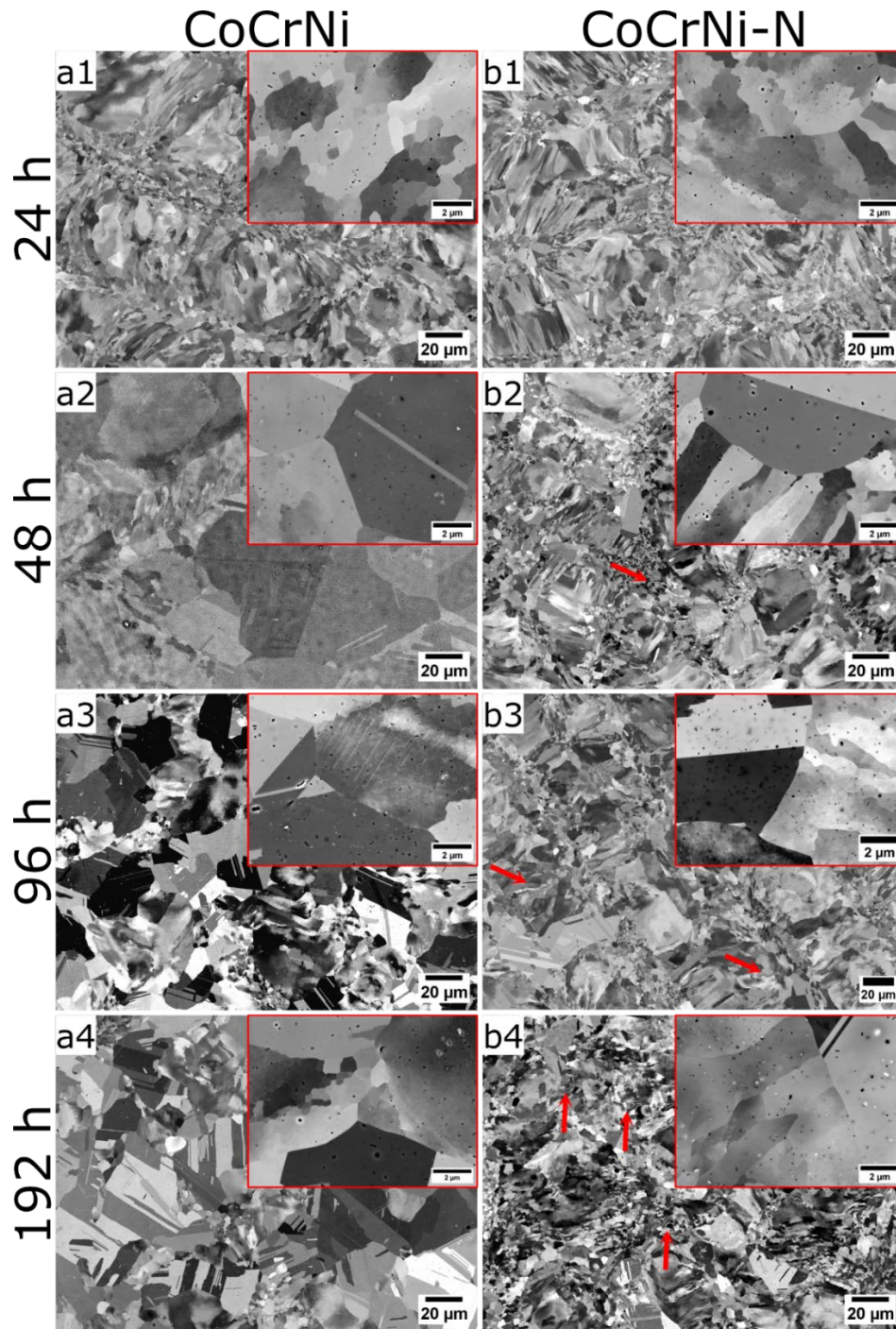


Figure 25 Backscattered electron images along with high magnification insets of samples heat treated at 900°C for 24, 48, 96 and 192 hours, for CoCrNi (a1-a4) and CoCrNi-N (a1-a4), respectively. Red arrows indicate the Cr-rich nitrides in after heat treatments.

Presence of oxide particles observed after heat treatments in both the alloys suggests that Zener pinning mechanism could also play a crucial role in retarded recrystallization kinetics. This is further supported by the STEM bright field image of CoCrNi-N alloy heat treated at 900°C for 192 hours (Figure 26a), which showed the bulging of the grain boundary between recrystallized and non-recrystallized grain. Feature analysis using SEM was performed on both the alloys heat treated at 900°C

for 192 hours to quantify the fraction of oxide particles in both the alloys and the results are as shown in Figure 26. From the particle size distributions (see Figure 26b), CoCrNi showed higher number density of oxide particles than CoCrNi-N with similar average particle size about  $\sim 60 \pm 30$  nm. This indicates that although Zener pinning could play a crucial role in hindering the recrystallization behaviour, the difference in number density of the particles between the alloys suggested solute drag effect caused by nitrogen enrichment at the grain boundaries could be dominant over the Zener pinning effect.

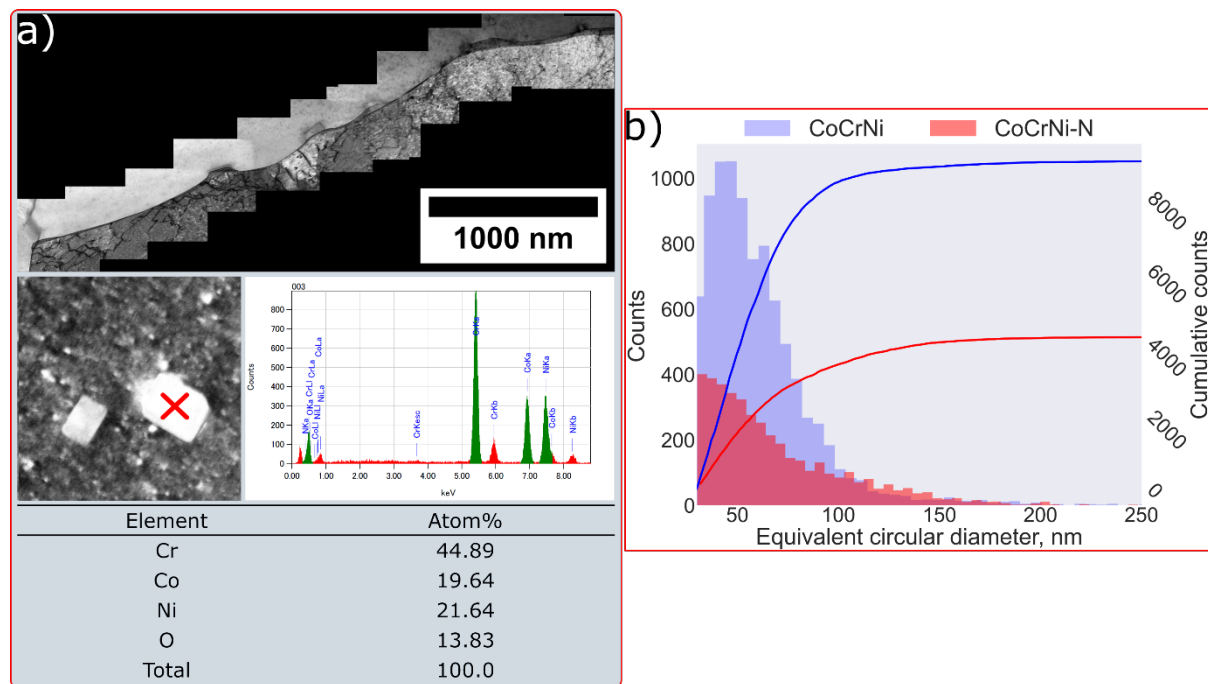


Figure 26 a) STEM bright field image of CoCrNi-N heat treated at 900°C for 192 hours, showing the recrystallized grain boundary, and TEM-EDS on the particles observed and b) feature analysis of oxide particles showing the distribution of particles in CoCrNi and CoCrNi-N heat treated at 900°C for 192 hours.

Table 3 summarizes the mechanical properties of both CoCrNi and CoCrNi-N obtained from the tensile tests performed at different heat treatment conditions. Both alloys showed a decrease in yield strength compared to the as-printed state after heat treatment at 800°C, with CoCrNi having a yield strength of about 650 MPa and CoCrNi-N having a yield strength of about 710 MPa. This decrease in yield strength is attributed to a combination of stress relieving and recovery, as no significant microstructural changes were observed. After heat treatment at 900°C for 24 hours,  $\sim 100$  MPa further decrease in the yield strength was observed for CoCrNi while less than 35 MPa decrease in yield strength was observed for CoCrNi-N. This difference in yield strength is consistent with the observed differences in recrystallized grain fractions between the alloys. Further increasing the heat treatment time to 192 hours

at 900°C resulted in the decrease of approximately 140 MPa in yield strength of CoCrNi, while CoCrNi-N only showed a decrease of approximately 50 MPa. This correlates well with the observed differences in recrystallization fractions between the alloys after heat treatments at 900°C. Similar differences were also observed after heat treatment at 1000°C. and hence CoCrNi-N showed consistently higher yield strength as compared to the CoCrNi for all the heat treatment times. In comparison to yield strength, the ultimate tensile strength (UTS) showed greater stability in response to heat treatment. This is because recrystallization reduces the dislocation density in the materials. Upon deformation, the alloys have the ability to work harden by generating dislocations, resulting in higher UTS values. Also with increasing heat treatment temperature, the elongation to fracture is significantly high, and hence can adopt higher UTS (undergo more work hardening).

*Table 3 Summary of mechanical properties of CoCrNi and CoCrNi-N alloys from the tensile tests performed on the selected heat treatment conditions.*

	CoCrNi			CoCrNi-N		
	YS (MPa)	UTS (MPa)	Elongation (%)	YS (MPa)	UTS (MPa)	Elongation (%)
<b>800°C 24 hours</b>	649	927	39.3	710	1002	38.0
<b>900°C 24 hours</b>	544	855	50.0	677	984	40.4
<b>900°C 192 hours</b>	407	824	54.3	588	932	37.8
<b>1000°C 24 hours</b>	388.30	822.66	51.18	493.6	925.90	51.18
<b>1000°C 192 hours</b>	340.03	808.05	64.71	445.6	873.22	61.11

The change in hardness as a function of heat treatment temperature and time along with the corresponding recrystallization fractions are presented in Figure 27a and b for CoCrNi and CoCrNi-N, respectively. After heat treatments at 800°C, both alloys did not show any change in the microstructure as a function of time and hence no significant change in the hardness was observed for both the alloys.

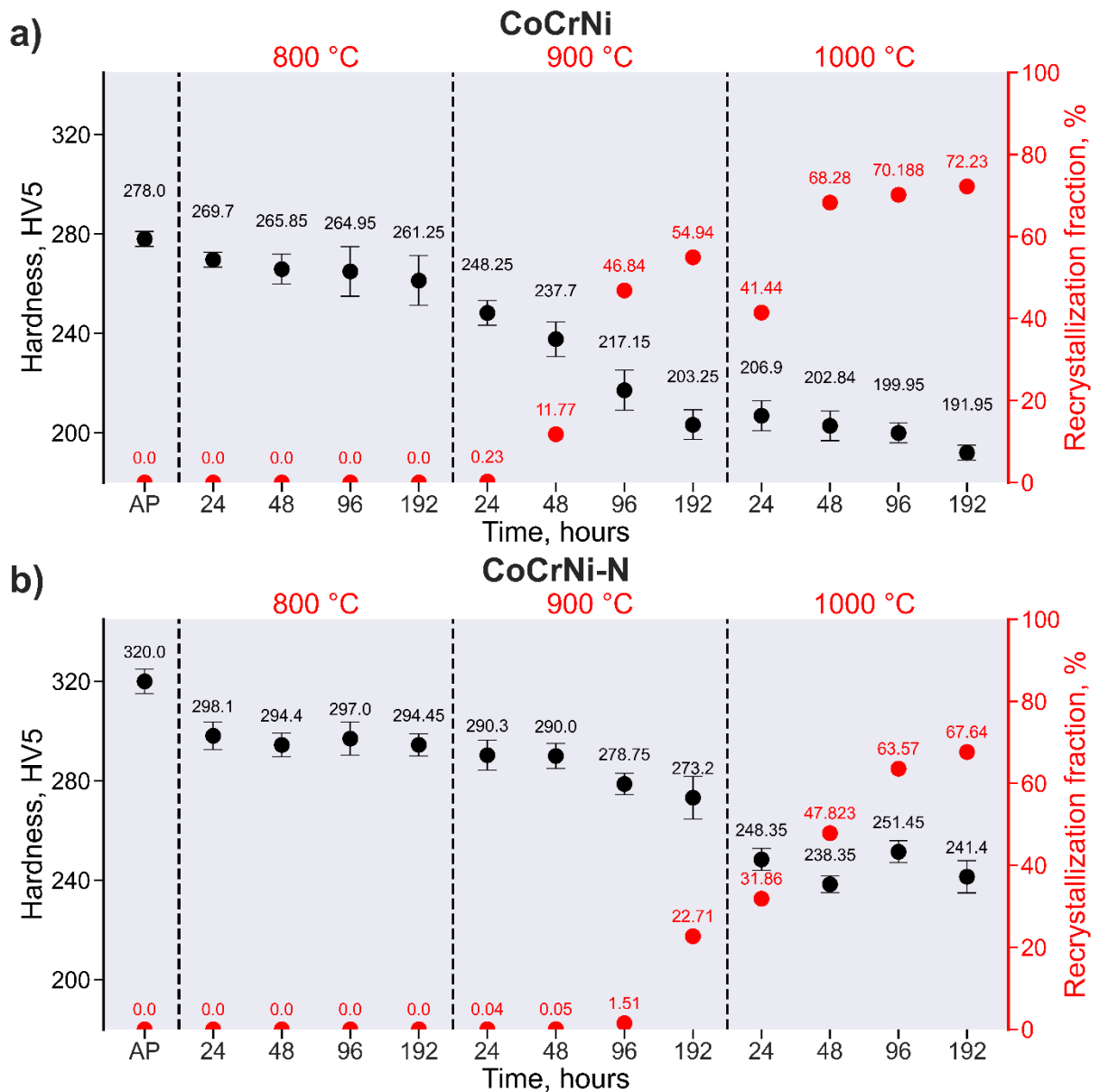


Figure 27 Hardness response and recrystallization fractions for a) CoCrNi and b) CoCrNi-N as a function of heat treatment time and temperatures.

After heat treatments at 900°C, as CoCrNi started to recrystallize, the change in the hardness was clearly evident with the increase in the heat treatment duration. CoCrNi-N on the other hand showed stronger resistance to recrystallization and did not show any change in the hardness even after heat treatments up to 48 hours. After 96 hours at 900°C, when the recrystallization fraction increased to 1.5%, a slight decrease in the hardness value to 278 HV5 was observed, and the hardness further decreased to 273 HV5 after 192 hours. These differences in hardness between CoCrNi and CoCrNi-N even after prolonged exposure at high temperatures showed the significance of interstitial solid solution strengthening. At 1000°C, the recrystallization kinetics was significantly faster than at 900°C, and there was a significant decrease in



hardness for both alloys compared to samples heat treated at 900°C for the same durations. The difference in hardness between both alloys was still clearly evident with CoCrNi-N showing a higher hardness.

### 5.5 Microstructure and mechanical behaviour of $\text{Co}_{45}\text{Cr}_{25}(\text{FeNi})_{30}$ non-equiatomic medium entropy alloy

The influence of high cooling rates inherent to PBF-LB on as-printed microstructure, phase fractions and resulting mechanical properties of a  $\text{Co}_{45}\text{Cr}_{25}(\text{FeNi})_{30}$  metastable MEA were studied. Figure 28a below shows the SEM-BSE image of the as-printed microstructure which showed a significant density of band-like features. Closer observations revealed a high density of cellular dislocations which are typical to PBF-LB along with the dislocation substructures. As-printed material showed strong (110) texture parallel to the building direction (see Figure 28c). The TKD analysis shown in Figure 28b, on the as-printed sample, indexed these band-like features as the HCP phase, suggesting the martensitic transformation due to the inherently high cooling rates during the PBF-LB process.

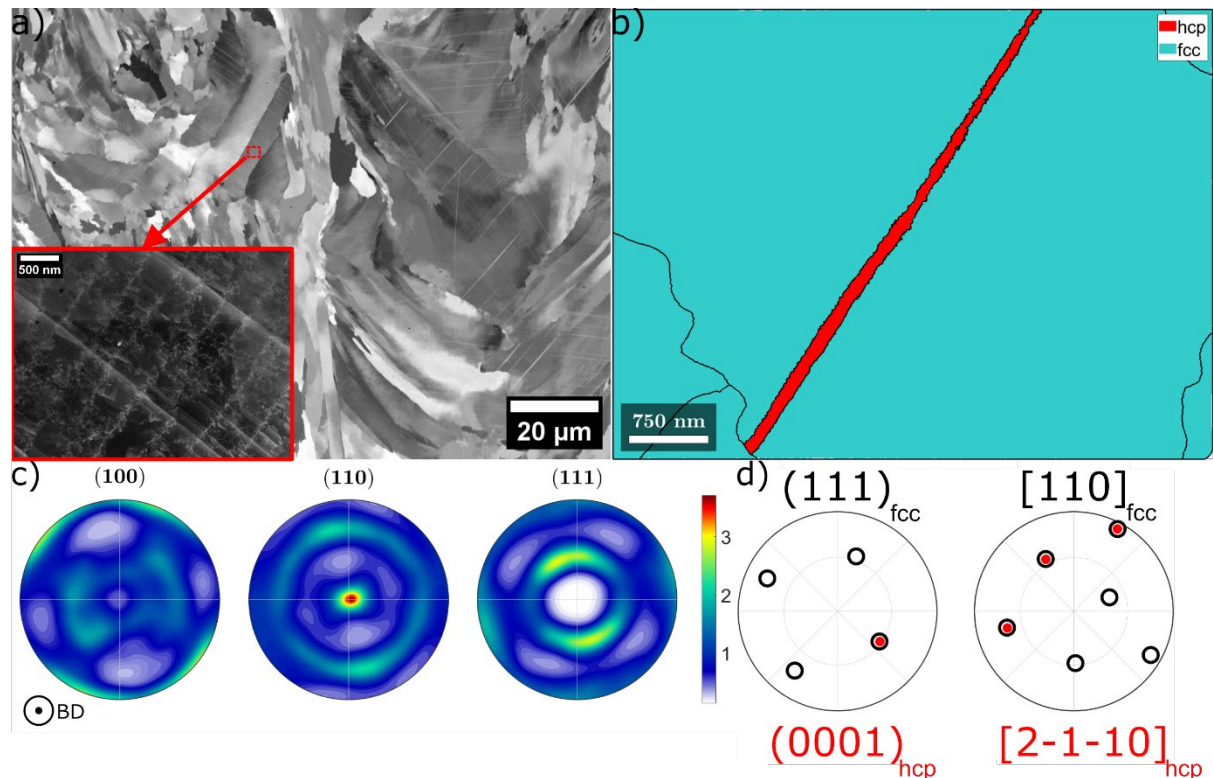


Figure 28 a) SEM-BSE image of the as-printed sample along with the high magnification ECCI image of the inset marked in red showing high density of dislocation sub structures along with HCP phase and dislocation cells, b) TKD phase map showing the presence of nano-scaled HCP phase, c) pole figures obtained from EBSD analysis showing (110) texture parallel to building direction and d) Pole figures of the FCC and HCP phase showing the S-N orientation relationship  $(111)_{\text{fcc}}/(0001)_{\text{hcp}}$  and  $[110]_{\text{fcc}}/[2-1-10]_{\text{hcp}}$ .

The HCP phase was observed in the samples obtained from both vertical and horizontal cross sections of the as-printed sample. Corresponding pole figures of the FCC and HCP phase revealed that the athermal martensite observed in the as-printed sample followed the  $(111)_{\text{fcc}}// (0001)_{\text{hcp}}$  and  $[110]_{\text{fcc}}// [2-1-10]_{\text{hcp}}$  orientation relationship, which is the Shoji-Nishiyama (S-N) orientation relationship as shown in Figure 28d.

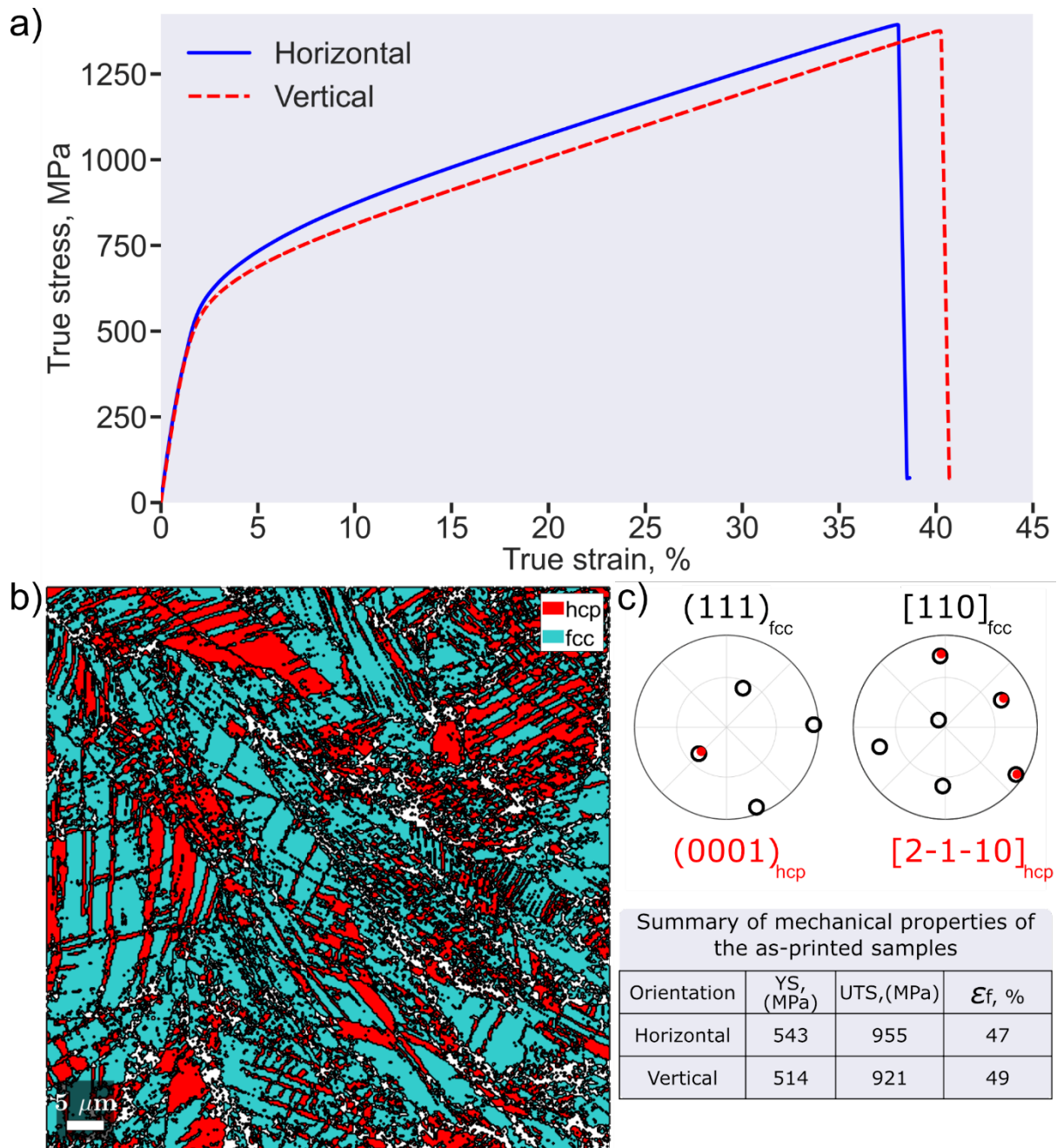


Figure 29 a) true stress - true strain plots of the as-printed sample obtained from both horizontal and vertical samples, b) EBSD phase maps of the fractured sample showing the FCC and HCP phase, along with the c) Pole figures of the FCC and HCP phase showing the S-N orientation relationship and a table summarizing the mechanical properties obtained from tensile tests.

Figure 29a shows the true stress-true strain plots of the as-printed sample obtained from vertical and horizontal directions and along with the table summarizing their tensile properties. The horizontal sample showed slightly higher yield strength and ultimate tensile strength as compared to the vertical sample. The elongation to fracture was observed to be higher in the vertical samples as compared to the horizontal samples. This difference in mechanical properties is common in PBF-LB processed materials due to the difference in texture with respect to building directions of the sample [160]. Figure 29b shows the EBSD phase map of the fractured horizontal sample. The measured phase fraction was approximately 50 % of the HCP phase. Figure 29c shows the corresponding pole figures of the FCC and HCP phase, confirming the S-N orientation relationship between the deformation induced HCP and FCC phase. In order to understand the TRIP behaviour and the influence of the load partitioning during deformation, in-situ tensile experiments were conducted using high energy synchrotron XRD and EBSD.

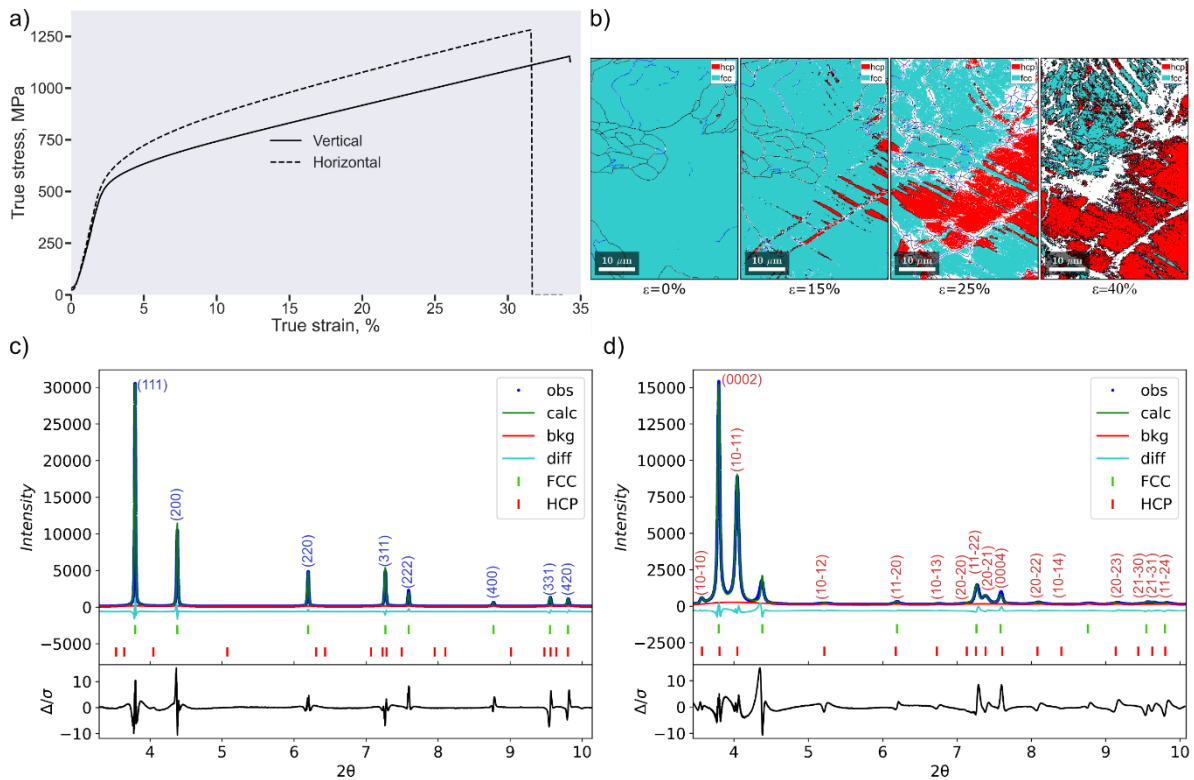


Figure 30 a) True stress vs true strain curve obtained during in-situ HEXRD experiments and b) EBSD phase maps obtained from in-situ EBSD tensile tests and Rietveld refinement on the 1D HEXRD patterns of the horizontal sample along the loading direction from c) as-printed state and d) after fracture, refined using GSAS II [151].

Figure 30a shows the true stress true strain plots obtained from the in-situ HEXRD experiments. The tensile behaviour with respect to the different building directions is

similar to what was observed in the ex-situ tensile tests (see Figure 29a). However, the observed strains were lower. This is due to non-standard geometry used during the in-situ HEXRD tests, which is known to result in varied strain. Figure 30b shows the EBSD phase maps of the in-situ EBSD tests showing the evolution of phase fractions as a function of strain. In the as-printed state, only FCC phase was observed because of the limited spatial resolution to index the nano-scaled HCP phase. At 15% nominal strain, the HCP phase fraction was 4% and with increase in the strain to 25%, the HCP phase fraction grew significantly to nearly 33%. Finally, at 40% nominal strain, the final measured HCP phase fraction was nearly 50%. This is consistent with the postmortem phase fractions shown in Figure 29b. Rietveld analysis was performed on the 1D-XRD profiles in order to confirm the relative phase fractions before and after in-situ tests and the results are shown in Figures 30c and 30d. Before the deformation, i.e., in the as-printed state, 0.8% and 1.5% of HCP was obtained from refinement while after refinement the HCP phase fraction increased to approximately 42% and 60% in the horizontal and vertical sample, respectively.

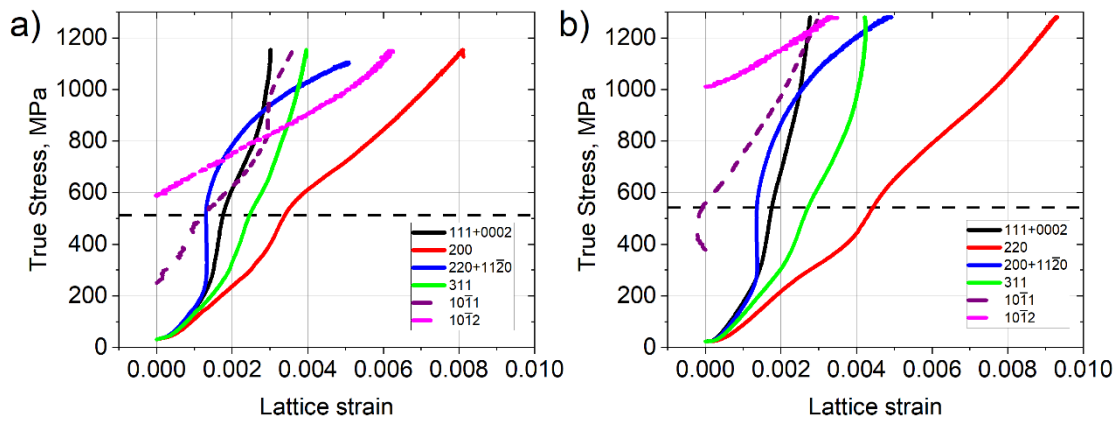


Figure 31 Lattice strain evolution with applied true stress along LD for a) vertical sample and for b) horizontal sample along. The black dashed line represents the yield strengths for horizontal and vertical samples obtained from the ex-situ tensile tests.

Figure 31 shows the lattice strain evolution for selected FCC and HCP reflections, measured from peak fitting as a function of true stress for vertical and horizontal samples. Though HCP phase was observed in both horizontal and vertical specimens as mentioned before, the volume fraction of it was too low as compared to FCC peaks to reliably fit it in the beginning. With increasing strain, as the HCP phase fraction increased, the HCP (10-11) reflection could be identified with greater reliability

starting at approximately 250 MPa and 375 MPa for vertical and horizontal samples, respectively.

Examining the lattice strain measurements, all FCC reflections exhibited nonlinear stress-strain response below the macroscopic yield point. The degree of nonlinearity increased in the order of FCC (200), (311), (111), and (220), in both vertical and horizontal samples. Although this nonlinearity is typical of FCC materials [161], the observed deviation from nonlinearity coincided with the formation of the HCP (10-10) reflection in both vertical and horizontal samples (Figures 31a and 31b). Further increase in the strain was observed to result in increasing nonlinearity for all observed FCC reflections, while the HCP (10-11) plane continued to strain linearly up to the macroscopic yield point. Beyond the yield point, the formation of HCP (10-12) reflection was observed in both vertical and horizontal samples albeit at different macroscopic stress. Further straining the samples showed significant increase in the lattice strain for the HCP (10-12) reflection, and result in the further unloading of all FCC reflections together with the HCP (10-11) reflection. The relaxation of FCC reflections at approximately 200 MPa below the macroscopic yield point, and the increase in nonlinearity of the FCC phase as the HCP phase started to appear in both vertical and horizontal samples, validated that load sharing was due to the stress induced martensitic transformation, occurring in the elastic regime of the tensile curve.



## 6 Conclusions

The aim of this thesis is to study the relationship between PBF-LB processing conditions and the microstructure and properties of ferritic stainless steels and medium entropy alloys. By delving into the influence of inoculation, interstitial solid solution strengthening, and processing conditions, this research yielded significant insights that advance our understanding of these materials and their potential applications. This research has led to the following important conclusions as summarized below.

### *In-situ inoculation in ferritic stainless steels (RQ1 and RQ2)*

Pre-alloying ferritic stainless steel with titanium and nitrogen effectively promotes the formation of fine equiaxed grains with preferential  $\langle 111 \rangle$  orientation as compared to preferential  $\langle 100 \rangle$  preferential orientation of grains when manufactured by means of PBF-LB. This transformation in grain morphology is attributed to the formation of efficient inoculants, namely a mixture of pure titanium nitrides and core-shell structured oxy-nitrides as depicted by EDS. These inoculants facilitate nucleation and growth of equiaxed grains in the as-printed materials. In both Ti-containing materials, the centre of the melt pools exhibited a high concentration of fine, equiaxed grains with sizes under 1  $\mu\text{m}$ , while the periphery of this zone contained slightly coarser, columnar grains. This distribution is attributed to the favourable solidification conditions at the centre of the melt pools, which promote the nucleation and growth of inoculants. These favourable conditions include relatively low G-values, high velocities (R), and extended liquid lifetimes. The higher number density of titanium-nitride particles in the equiaxed grain regions supports this explanation.

Both Ti-containing and Ti-free materials exhibited finer grain sizes in single tracks produced at higher scan speeds (1000 mm/s). However, the bulk samples of Ti-free material showed significantly coarser grains compared to the single tracks due to epitaxial growth during remelting by neighbouring tracks and subsequent layers. In contrast, the bulk samples of Ti-containing material exhibited an improvement in grain refinement due to remelting, suggesting an interactive effect between the formation of inoculants and the remelting process.



### *As-printed microstructure and properties of CoCrNi and CoCrNi-N MEAs (RQ3)*

As-printed microstructures revealed cellular solidification structure with elemental segregation of chromium and nitrogen to the cell walls, as predicted from Scheil solidification simulations. Along with the cellular solidification structure, high density of dislocation cells was observed in both the alloys, supposed to be a result of the subsequent thermal cycling during the layer-by-layer printing process. The CoCrNi-N alloys demonstrated approximately 100 MPa higher yield strength and ultimate tensile strength compared to the CoCrNi variant, while also exhibiting reduced anisotropy in mechanical properties with respect to different building directions. Short-term heat treatments at 800°C for 30 minutes resulted in the formation of fine chromium-rich oxides along the grain boundaries of both alloys and these oxides were not observed in as-printed condition. Increasing the heat treatment temperature led to the coarsening of these oxides while Cr<sub>2</sub>N precipitation was not observed during the heat treatment process. After heat treatment at 1200°C, both alloys exhibited a recrystallized microstructure. The CoCrNi-N alloy consistently displayed hardness value approximately 35 HV higher than the CoCrNi variant, both in the as-printed and heat-treated states. Addition of 0.5 wt% and 5 wt% TiN nanoparticles of size around 80 nm to CoCrNi alloy improved the mechanical properties without any change in the general microstructure. The distribution of the TiN was much finer than depicted from metal powder size. The improvement in the hardness value of approximately 30 HV and 80 HV was observed with the addition of 0.5 wt% and 5 wt% TiN nanoparticles.

Potentiodynamic tests in acidic and saline environments showed better corrosion properties for both the CoCrNi and CoCrNi-N materials compared to those for conventional and PBF-LB fabricated 316L. The CoCrNi-N showed better passivation behaviour but similar corrosion behaviour when compared to the CoCrNi. The angle-resolved XPS (ARXPS) on passivated samples did not show any presence of Co and Ni on the passive film. The passive film was observed to be composed of Cr-oxide and Cr-hydroxide as confirmed by the peak fitting. The hydroxide to oxide ratios extracted from the intensities of curve fitted peaks revealed no significant difference in surface composition between the CoCrNi and CoCrNi-N alloys.



#### *Influence of nitrogen on the recrystallization behaviour of CoCrNi MEA (RQ4)*

High-temperature heat treatments of CoCrNi and CoCrNi-N at 800°C, 900°C, and 1000°C for longer holding times revealed distinct microstructural and phase stability changes. For both alloys, heat treatment at 800°C resulted in the precipitation of chromium-rich oxides, while 900°C induced recrystallization accompanied by the formation of larger nitride particles in CoCrNi-N. At 1000°C, recrystallization progressed further, but the recrystallized grain fraction remained lower in CoCrNi-N compared to CoCrNi. Oxide particle analysis indicated a higher number density in CoCrNi, suggesting a lower pinning effect in the nitrogen-containing alloy by such oxide particles. Since the sole difference between the alloys is nitrogen content, the lower recrystallization kinetics in CoCrNi-N is hence suggested to be attributed to nitrogen segregation at grain boundaries, leading to solute drag, hindering grain boundary migration.

#### *Influence of PBF-LB processing metastable Co<sub>45</sub>Cr<sub>25</sub>(FeNi)<sub>30</sub> MEA (RQ5)*

Microstructural examination revealed that high cooling rates inherent to PBF-LB processing led to the formation of nano-scaled HCP phase in the as-printed Co<sub>45</sub>Cr<sub>25</sub>(FeNi)<sub>30</sub> metastable MEA. This HCP phase was observed in both vertical and horizontal cross sections of the as-printed sample. The pole figures of FCC and HCP phases revealed that this athermal martensite (HCP phase) observed in the as-printed sample followed the Shoji-Nishiyama (S-N) orientation relationship. The mechanical properties of the as-printed samples were found to be dependent on the building direction, with the horizontal samples showing slightly higher yield strength and ultimate tensile strength values while lower elongation to fracture as compared to the vertical samples. This difference in the mechanical properties is common in PBF-LB processed materials owing to the difference in texture with respect to building orientation of the sample. Postmortem EBSD analysis revealed approximately 50% HCP phase in the fractured horizontal sample, with a similar S-N orientation relationship between the HCP and FCC phase. In-situ tensile experiments were conducted using high energy synchrotron XRD and EBSD to understand the TRIP behaviour and the influence of the load partitioning during deformation. The results showed that the HCP phase fraction increased with increasing strain, and that the nano-scaled HCP phase in the as-printed state played an important role in the TRIP behaviour of the alloy. The HCP phase fraction increased from 0.8% and 1.5% to

approximately 42 % (at fracture) and 60 % (at 40% nominal strain) respectively for horizontal and vertical samples in the as-printed state. From the lattice strain/true stress plots, we observed that the FCC reflections start to deviate from linearity well below the macroscopic yield point, which coincided with the formation of HCP (10-11) reflection, indicating the load sharing between the FCC and HCP phase. This proves that not only stress induced martensitic transformation was happening, but the so formed HCP also played a crucial role in shaping the mechanical behaviour of the alloy.

## 7 Future scope

The following aspects are not addressed yet in the current thesis but are potential directions to be considered for future research.

### Inoculation:

- To explore the influence of inoculation on the static and dynamic mechanical properties of ferritic stainless steels manufactured using the PBF-LB process.
- To investigate the influence of ex-situ and in-situ addition of inoculants on the CET in the columnar regions of ferritic stainless steels, both with and without inoculation forming elements.
- To investigate the feasibility of inoculation in austenitic alloys manufactured using the PBF-LB process.

### Medium entropy alloys:

#### **CoCrNi-N MEAs**

- To conduct a comprehensive study to elucidate the deformation mechanisms for CoCrNi and CoCrNi-N in both as-printed and heat-treated conditions. Specifically, the interplay between high dislocation cell density in the as-printed state and its influence on twinning behaviour is of interest.
- To conduct detailed investigation on the high temperature stability of both CoCrNi and CoCrNi-N alloys, particularly the underlying mechanisms responsible for the stabilization of hardness after heat treatments at 1000°C.
- To further extend the research on the high temperature stability of CoCrNi and CoCrNi-N alloys by delving into their creep behaviour.

#### **The Co<sub>45</sub>Cr<sub>25</sub>(FeNi)<sub>30</sub> MEA**

- To study the influence of stress relieving/annealing heat treatments on the phase stability, microstructure and resulting mechanical properties.
- To examine the relationship between microstructural changes, such as grain size and phase distribution, and their influence on the TRIP behaviour and load partitioning behaviour of the alloy.
- To conduct a detailed microstructural characterization of the deformation mechanisms, such as dislocation slip and twinning, in FCC and HCP phases of the alloy, in both the as printed and heat-treated states, for a better understanding of their role in the observed load partitioning behaviour.



## **Acknowledgements**

I would like to express my deepest gratitude to my supervisors, Prof. Lars Nyborg and Prof. Sheng Guo, for providing me with this exceptional opportunity and their unwavering guidance, support, and encouragement throughout my research journey. Their expertise, passion for science, and mentorship have been instrumental in shaping my academic and professional development. I am particularly grateful for their insights and stimulating discussions, which have fuelled my passion for exploring the fascinating world of materials science. Additionally, I would like to extend my sincere appreciation to Prof. Eduard Hryha for his unwavering support and encouragement. I would also like to express my deepest gratitude to Prof. Uta Klement for her insightful discussions and invaluable suggestions. Sincerest thanks to Prof. Nobuhiro Tsuji for hosting me and supporting me during my research stay at Kyoto University. I would like to extend my thanks to Dr. Reza Gholizadeh for your guidance, support, and help.

I would like to express my sincere gratitude to Prof. Greta Lindwall, Prof. Durga Ananthanarayanan, and Dr. Niklas Holländer Pettersson for their invaluable insights and contributions to this project. The industrial partners Höganäs AB and Kanthal AB are gratefully acknowledged for their generous support and collaboration. I am particularly indebted to Adjunct professors Karin Frisk and Sven Bengtsson, Dr. Maheswaran Vattur Sundaram from Höganäs AB, and Mr. Roger Berglund from Kanthal AB for their valuable assistance with alloys, analyses, and stimulating discussions. I extend my heartfelt gratitude to Dr. Zhuoer Chen for his guidance and invaluable discussions. Special thanks are due to Dr. Tatiana Mishurova and Dr. Alexander Evans for their support with synchrotron experiments, analyses, and insightful discussions. I am deeply grateful to Prof. Yu Cao and Dr. Eric Tam for their expert guidance and support with XPS. I am also deeply appreciative of Prof. Fang Liu's invaluable contributions to the TEM experiments, insightful discussions, and valuable suggestions, which significantly enhanced the project.

This thesis work would not have been possible without the support from Dr. Yiming Yao, Roger, Johnny, Håkan and Dr. Antonio. Special “bobble head” thanks to Dr. Dmitri Riabov for his help with TEM. I would like to acknowledge the support from the administrative staff, Lilvor, Jessica, and Charlott. I would like to thank all my

friends and colleagues at the department especially everyone in the MM and EM divisions.

I would like to offer my special thanks to Dr. Swathi K Manchili for the guidance and support and gossips throughout my time in Sweden and especially for making the office fun. I am also profoundly grateful to Plinio for all the playful pranks, which have brightened countless days at the office. A special thank you to Erika, Alberto, Marcos and Zhuoer for their friendship, laughter, and cherished memories. I am also immensely grateful to, Angelica, Fardan, Anok, Gren, Sahith, Vishnu, Sofia, and the many others who have enriched my time here with all the fun and laughter and good times.

Last but not least, I would like to thank my parents for all their support these years and would like to dedicate this this work to them. I would definitely not even be in this position if not for their sacrifice and their support.

## **References**

- [1] Additive manufacturing-General principles-Fundamentals and vocabulary 1,2, n.d. <https://www.iso.org/obp>.
- [2] E. Davoodi, H. Montazerian, A.S. Mirhakimi, M. Zhianmanesh, O. Ibhaddode, S.I. Shahabad, R. Esmaeilizadeh, E. Sarikhani, S. Toorandaz, S.A. Sarabi, R. Nasiri, Y. Zhu, J. Kadkhodapour, B. Li, A. Khademhosseini, E. Toyserkani, Additively manufactured metallic biomaterials, *Bioact Mater* 15 (2022) 214–249. <https://doi.org/10.1016/J.BIOACTMAT.2021.12.027>.
- [3] L.J. Kumar, C.G. Krishnadas Nair, Current Trends of Additive Manufacturing in the Aerospace Industry, *Advances in 3D Printing and Additive Manufacturing Technologies* (2017) 39–54. [https://doi.org/10.1007/978-981-10-0812-2\\_4](https://doi.org/10.1007/978-981-10-0812-2_4).
- [4] R. Bogue, 3D printing: the dawn of a new era in manufacturing?, *Assembly Automation* 33 (2013) 307–311. <https://doi.org/10.1108/AA-06-2013-055>.
- [5] B. Mehta, K. Frisk, L. Nyborg, Advancing novel Al-Mn-Cr-Zr based family of alloys tailored for powder bed fusion-laser beam process, *J Alloys Compd* 967 (2023). <https://doi.org/10.1016/j.jallcom.2023.171685>.
- [6] S. Chen, Y. Tong, P.K. Liaw, Additive manufacturing of high-entropy alloys: A review, *Entropy* 20 (2018). <https://doi.org/10.3390/e20120937>.
- [7] A. Ostovari Moghaddam, N.A. Shaburova, M.N. Samodurova, A. Abdollahzadeh, E.A. Trofimov, Additive manufacturing of high entropy alloys: A practical review, *J Mater Sci Technol* 77 (2021) 131–162. <https://doi.org/10.1016/J.JMST.2020.11.029>.
- [8] W. Zhang, H. Wang, B.J. Kooi, Y. Pei, Additive manufacturing of interstitial-strengthened high entropy alloy: Scanning strategy dependent anisotropic mechanical properties, *Materials Science and Engineering: A* 872 (2023) 144978. <https://doi.org/10.1016/J.MSEA.2023.144978>.
- [9] V. Ocelík, N. Janssen, S.N. Smith, J.T.M. De Hosson, Additive Manufacturing of High-Entropy Alloys by Laser Processing, *Jom* 68 (2016) 1810–1818. <https://doi.org/10.1007/s11837-016-1888-z>.

- [10] P. Agrawal, R.S. Haridas, S. Thapliyal, S. Yadav, R.S. Mishra, B.A. McWilliams, K.C. Cho, Metastable high entropy alloys: An excellent defect tolerant material for additive manufacturing, *Materials Science and Engineering: A* 826 (2021) 142005. <https://doi.org/10.1016/J.MSEA.2021.142005>.
- [11] B. Li, L. Zhang, B. Yang, Grain refinement and localized amorphization of additively manufactured high-entropy alloy matrix composites reinforced by nano ceramic particles via selective-laser-melting/remelting, *Composites Communications* 19 (2020) 56–60. <https://doi.org/10.1016/J.COCO.2020.03.001>.
- [12] S. Thapliyal, S.S. Nene, P. Agrawal, T. Wang, C. Morphey, R.S. Mishra, B.A. McWilliams, K.C. Cho, Damage-tolerant, corrosion-resistant high entropy alloy with high strength and ductility by laser powder bed fusion additive manufacturing, *Addit Manuf* 36 (2020) 101455. <https://doi.org/10.1016/J.ADDMA.2020.101455>.
- [13] A. Durga, N.H. Pettersson, S.B.A. Malladi, Z. Chen, S. Guo, L. Nyborg, G. Lindwall, Grain refinement in additively manufactured ferritic stainless steel by in situ inoculation using pre-alloyed powder, *Scr Mater* 194 (2021). <https://doi.org/10.1016/j.scriptamat.2020.113690>.
- [14] D. Herzog, V. Seyda, E. Wycisk, C. Emmelmann, Additive manufacturing of metals, *Acta Mater* 117 (2016) 371–392. <https://doi.org/10.1016/j.actamat.2016.07.019>.
- [15] AMPOWER Report on the Additive Manufacturing market, (n.d.). <https://additive-manufacturing-report.com/> (accessed October 5, 2021).
- [16] C. Villamil, J. Nylander, S.I. Hallstedt, J. Schulte, M. Watz, Additive manufacturing from a strategic sustainability perspective, *Proceedings of International Design Conference, DESIGN* 3 (2018) 1381–1392. <https://doi.org/10.21278/idc.2018.0353>.
- [17] S. Kou, *Welding metallurgy*, 3rd ed., Wiley, 2020. <https://doi.org/10.1002/0471434027>.
- [18] C. Kusuma, The Effect of Laser Power and Scan Speed on Melt Pool The Effect of Laser Power and Scan Speed on Melt Pool Characteristics of Pure Titanium and Ti-6Al-4V Alloy for Selective Characteristics of Pure Titanium and Ti-6Al-



- 4V Alloy for Selective Laser Melting Laser Melting, (n.d.). [https://corescholar.libraries.wright.edu/etd\\_all](https://corescholar.libraries.wright.edu/etd_all) (accessed October 13, 2021).
- [19] D.F. Louw, P.G.H. Pistorius, The effect of scan speed and hatch distance on prior-beta grain size in laser powder bed fused Ti-6Al-4V, *The International Journal of Advanced Manufacturing Technology* 2019 103:5 103 (2019) 2277–2286. <https://doi.org/10.1007/S00170-019-03719-W>.
- [20] A.B. Spierings, K. Dawson, P.J. Uggowitzer, K. Wegener, Influence of SLM scan-speed on microstructure, precipitation of Al<sub>3</sub>Sc particles and mechanical properties in Sc-and Zr-modified Al-Mg alloys, *Mater Des* 140 (2018) 134–143. <https://doi.org/10.1016/j.matdes.2017.11.053>.
- [21] H. Jia, H. Sun, H. Wang, Y. Wu, H. Wang, Scanning strategy in selective laser melting (SLM): a review, *The International Journal of Advanced Manufacturing Technology* 2021 113:9 113 (2021) 2413–2435. <https://doi.org/10.1007/S00170-021-06810-3>.
- [22] J.J. Marattukalam, D. Karlsson, V. Pacheco, P. Beran, U. Wiklund, U. Jansson, B. Hjörvarsson, M. Sahlberg, The effect of laser scanning strategies on texture, mechanical properties, and site-specific grain orientation in selective laser melted 316L SS, *Mater Des* 193 (2020). <https://doi.org/10.1016/j.matdes.2020.108852>.
- [23] A.R.A. Dezfoli, W.-S. Hwang, W.-C. Huang, T.-W. Tsai, Determination and controlling of grain structure of metals after laser incidence: Theoretical approach, *Scientific Reports* 2017 7:1 7 (2017) 1–11. <https://doi.org/10.1038/srep41527>.
- [24] K.P. Monroy, J. Delgado, L. Sereno, J. Ciurana, N.J. Hendrichs, Effects of the Selective Laser Melting manufacturing process on the properties of CoCrMo single tracks, *Metals and Materials International* 2014 20:5 20 (2014) 873–884. <https://doi.org/10.1007/S12540-014-5011-0>.
- [25] S. Ghosh, L. Ma, L.E. Levine, R.E. Ricker, M.R. Stoudt, J.C. Heigel, J.E. Guyer, Single-Track Melt-Pool Measurements and Microstructures in Inconel 625, *JOM* 2018 70:6 70 (2018) 1011–1016. <https://doi.org/10.1007/S11837-018-2771-X>.

- [26] Y. Lee, M. Nordin, S.S. Babu, D.F. Farson, Effect of Fluid Convection on Dendrite Arm Spacing in Laser Deposition, *Metallurgical and Materials Transactions B* 2014 45:4 45 (2014) 1520–1529. <https://doi.org/10.1007/S11663-014-0054-7>.
- [27] P. Köhnen, M. Létang, M. Voshage, J.H. Schleifenbaum, C. Haase, Understanding the process-microstructure correlations for tailoring the mechanical properties of L-PBF produced austenitic advanced high strength steel, *Addit Manuf* 30 (2019) 100914. <https://doi.org/10.1016/J.ADDMA.2019.100914>.
- [28] X. Zhang, C.J. Yocom, B. Mao, Y. Liao, Microstructure evolution during selective laser melting of metallic materials: A review, *J Laser Appl* 31 (2019) 031201. <https://doi.org/10.2351/1.5085206>.
- [29] Y. Liu, Y. Yang, D. Wang, A study on the residual stress during selective laser melting (SLM) of metallic powder, *International Journal of Advanced Manufacturing Technology* 87 (2016) 647–656. <https://doi.org/10.1007/s00170-016-8466-y>.
- [30] N. Nadammal, S. Cabeza, T. Mishurova, T. Thiede, A. Kromm, C. Seyfert, L. Farahbod, C. Haberland, J.A. Schneider, P.D. Portella, G. Bruno, Effect of hatch length on the development of microstructure, texture and residual stresses in selective laser melted superalloy Inconel 718, *Mater Des* 134 (2017) 139–150. <https://doi.org/10.1016/J.MATDES.2017.08.049>.
- [31] E.D. Amoako, P. Mensah, S. Akwaboa, S. Ibekwe, G. Li, Parametric Study of SLM Processing Parameters on In-Situ Residual Stress, *ASME 2019 Heat Transfer Summer Conference, HT 2019, Collocated with the ASME 2019 13th International Conference on Energy Sustainability* (2019). <https://doi.org/10.1115/HT2019-3623>.
- [32] Y. Hong, C. Zhou, Y. Zheng, L. Zhang, J. Zheng, The cellular boundary with high density of dislocations governed the strengthening mechanism in selective laser melted 316L stainless steel, *Materials Science and Engineering: A* 799 (2021) 140279. <https://doi.org/10.1016/J.MSEA.2020.140279>.
- [33] K.M. Bertsch, G. Meric de Bellefon, B. Kuehl, D.J. Thoma, Origin of dislocation structures in an additively manufactured austenitic stainless steel 316L, *Acta Mater* 199 (2020) 19–33. <https://doi.org/10.1016/J.ACTAMAT.2020.07.063>.

- [34] D. Kong, C. Dong, S. Wei, X. Ni, L. Zhang, R. Li, L. Wang, C. Man, X. Li, About metastable cellular structure in additively manufactured austenitic stainless steels, *Addit Manuf* 38 (2021) 2214–8604. <https://doi.org/10.1016/j.addma.2020.101804>.
- [35] O. Zinovieva, V. Romanova, R. Balokhonov, Effects of scanning pattern on the grain structure and elastic properties of additively manufactured 316L austenitic stainless steel, *Materials Science and Engineering: A* 832 (2022) 142447. <https://doi.org/10.1016/J.MSEA.2021.142447>.
- [36] B.S. Murty, S.A. Kori, M. Chakraborty, Grain refinement of aluminium and its alloys by heterogeneous nucleation and alloying, *International Materials Reviews* 47 (2002) 3–29. <https://doi.org/10.1179/095066001225001049>.
- [37] M.J. Bermingham, D.H. StJohn, J. Krynen, S. Tedman-Jones, M.S. Dargusch, Promoting the columnar to equiaxed transition and grain refinement of titanium alloys during additive manufacturing, *Acta Mater* 168 (2019) 261–274. <https://doi.org/10.1016/j.actamat.2019.02.020>.
- [38] K. v. Yang, Y. Shi, F. Palm, X. Wu, P. Rometsch, Columnar to equiaxed transition in Al-Mg(-Sc)-Zr alloys produced by selective laser melting, *Scr Mater* 145 (2018) 113–117. <https://doi.org/10.1016/J.SCRIPTAMAT.2017.10.021>.
- [39] B. Chalmers, *Principles of Solidification*, *Applied Solid State Physics* (1970) 161–170. [https://doi.org/10.1007/978-1-4684-1854-5\\_5](https://doi.org/10.1007/978-1-4684-1854-5_5).
- [40] Hasse. Fredriksson, Ulla. Akerlind, *Solidification and Crystallization Processing in Metals and Alloys.*, (2012) 828.
- [41] A.L. Greer, J.H. Perepezko, F. Franks, B. Cantor, R.W. Cahn, Grain refinement of alloys by inoculation of melts, in: *Philosophical Transactions of the Royal Society A: Mathematical, Physical and Engineering Sciences*, Royal Society, 2003: pp. 479–495. <https://doi.org/10.1098/rsta.2002.1147>.
- [42] J.F. Wallace, Grain Refinement of Steels, *Jom* 15 (1963) 372–376. <https://doi.org/10.1007/bf03378248>.
- [43] A.L. Greer, T.E. Quested, Heterogeneous grain initiation in solidification, <https://doi.org/10.1080/14786430500198486> 86 (2007) 3665–3680. <https://doi.org/10.1080/14786430500198486>.

- [44] J.H. Martin, B.D. Yahata, J.M. Hundley, J.A. Mayer, T.A. Schaedler, T.M. Pollock, 3D printing of high-strength aluminium alloys, *Nature* 2017 549:7672 549 (2017) 365–369. <https://doi.org/10.1038/nature23894>.
- [45] J.H. Martin, B. Yahata, J. Mayer, R. Mone, E. Stonkevitch, J. Miller, M.R. O'Masta, T. Schaedler, J. Hundley, P. Callahan, T. Pollock, Grain refinement mechanisms in additively manufactured nano-functionalized aluminum, *Acta Mater* 200 (2020) 1022–1037. <https://doi.org/10.1016/j.actamat.2020.09.043>.
- [46] F. Yan, W. Xiong, E.J. Faierson, Grain Structure Control of Additively Manufactured Metallic Materials, *Materials* 2017, Vol. 10, Page 1260 10 (2017) 1260. <https://doi.org/10.3390/MA10111260>.
- [47] W.E. Frazier, Metal additive manufacturing: A review, *J Mater Eng Perform* 23 (2014) 1917–1928. <https://doi.org/10.1007/s11665-014-0958-z>.
- [48] J.R. Kennedy, A.E. Davis, A.E. Caballero, S. Williams, E.J. Pickering, P.B. Prangnell, The potential for grain refinement of Wire-Arc Additive Manufactured (WAAM) Ti-6Al-4V by ZrN and TiN inoculation, *Addit Manuf* 40 (2021) 101928. <https://doi.org/10.1016/J.ADDMA.2021.101928>.
- [49] S. Mereddy, M.J. Bermingham, D. Kent, A. Dehghan-Manshadi, D.H. StJohn, M.S. Dargusch, Trace Carbon Addition to Refine Microstructure and Enhance Properties of Additive-Manufactured Ti-6Al-4V, *JOM* 2018 70:9 70 (2018) 1670–1676. <https://doi.org/10.1007/S11837-018-2994-X>.
- [50] M.R. Rolchigo, M.Y. Mendoza, P. Samimi, D.A. Brice, B. Martin, P.C. Collins, R. LeSar, Modeling of Ti-W Solidification Microstructures Under Additive Manufacturing Conditions, *Metallurgical and Materials Transactions A* 2017 48:7 48 (2017) 3606–3622. <https://doi.org/10.1007/S11661-017-4120-Z>.
- [51] M.J. Bermingham, S.D. McDonald, A.J. Buddery, D.H. Stjohn, M.S. Dargusch, Processing considerations for cast Ti-25Nb-3Mo-3Zr-2Sn biomedical alloys, *Materials Science and Engineering: C* 31 (2011) 1520–1525. <https://doi.org/10.1016/J.MSEC.2011.06.011>.
- [52] D. Zhang, A. Prasad, M.J. Bermingham, C.J. Todaro, M.J. Benoit, M.N. Patel, D. Qiu, D.H. StJohn, M. Qian, M.A. Easton, Grain Refinement of Alloys in Fusion-Based Additive Manufacturing Processes, *Metallurgical and Materials*

- Transactions A 2020 51:9 51 (2020) 4341–4359. <https://doi.org/10.1007/S11661-020-05880-4>.
- [53] F. Beilelli, R. Casati, F. Larini, M. Riccio, M. Vedani, Investigation on two Ti–B-reinforced Al alloys for Laser Powder Bed Fusion, *Materials Science and Engineering: A* 808 (2021) 140944. <https://doi.org/10.1016/J.MSEA.2021.140944>.
- [54] X.P. Li, G. Ji, Z. Chen, A. Addad, Y. Wu, H.W. Wang, J. Vleugels, J. van Humbeeck, J.P. Kruth, Selective laser melting of nano-TiB<sub>2</sub> decorated AlSi10Mg alloy with high fracture strength and ductility, *Acta Mater* 129 (2017) 183–193. <https://doi.org/10.1016/J.ACTAMAT.2017.02.062>.
- [55] S. Thapliyal, S. Shukla, L. Zhou, H. Hyer, P. Agrawal, P. Agrawal, M. Komarasamy, Y. Sohn, R.S. Mishra, Design of heterogeneous structured Al alloys with wide processing window for laser-powder bed fusion additive manufacturing, *Addit Manuf* 42 (2021) 102002. <https://doi.org/10.1016/J.ADDMA.2021.102002>.
- [56] B. Li, B. Qian, Y. Xu, Z. Liu, F. Xuan, Fine-structured CoCrFeNiMn high-entropy alloy matrix composite with 12 wt% TiN particle reinforcements via selective laser melting assisted additive manufacturing, *Mater Lett* 252 (2019) 88–91. <https://doi.org/10.1016/j.matlet.2019.05.108>.
- [57] Y. Brif, M. Thomas, I. Todd, The use of high-entropy alloys in additive manufacturing, *Scr Mater* 99 (2015) 93–96. <https://doi.org/10.1016/j.scriptamat.2014.11.037>.
- [58] H. Ikehata, E. Jäggle, Grain refinement of Fe-X alloys fabricated by laser powder bed fusion, *Materials Science Forum* 1016 MSF (2021) 580–586. <https://doi.org/10.4028/WWW.SCIENTIFIC.NET/MSF.1016.580>.
- [59] H. Ikehata, E. Jäggle, Evaluation of microstructure and tensile properties of grain-refined, Ti-alloyed ferritic stainless steel fabricated by laser powder bed fusion, *Materials Science and Engineering: A* 818 (2021) 141365. <https://doi.org/10.1016/J.MSEA.2021.141365>.
- [60] D. Karlsson, C.Y. Chou, N.H. Pettersson, T. Helander, P. Harlin, M. Sahlberg, G. Lindwall, J. Odqvist, U. Jansson, Additive manufacturing of the ferritic stainless steel SS441, *Addit Manuf* 36 (2020) 101580. <https://doi.org/10.1016/j.addma.2020.101580>.

- [61] B.L. Bramfitt, The effect of carbide and nitride additions on the heterogeneous nucleation behavior of liquid iron, *Metallurgical Transactions* 1 (1970) 2958. <https://doi.org/10.1007/BF03037838>.
- [62] A. Durga, N.H. Pettersson, S.B.A. Malladi, Z. Chen, S. Guo, L. Nyborg, G. Lindwall, Grain refinement in additively manufactured ferritic stainless steel by in situ inoculation using pre-alloyed powder, *Scr Mater* 194 (2021). <https://doi.org/10.1016/j.scriptamat.2020.113690>.
- [63] E. Liverani, S. Toschi, L. Ceschini, A. Fortunato, Effect of selective laser melting (SLM) process parameters on microstructure and mechanical properties of 316L austenitic stainless steel, *J Mater Process Technol* 249 (2017) 255–263. <https://doi.org/10.1016/J.JMATPROTEC.2017.05.042>.
- [64] S. Liu, Y.C. Shin, Additive manufacturing of Ti6Al4V alloy: A review, *Mater Des* 164 (2019) 107552. <https://doi.org/10.1016/J.MATDES.2018.107552>.
- [65] A.I. Mertens, J. Delahaye, J. Lecomte-Beckers, Fusion-Based Additive Manufacturing for Processing Aluminum Alloys: State-of-the-Art and Challenges, *Adv Eng Mater* 19 (2017) 1700003. <https://doi.org/10.1002/ADEM.201700003>.
- [66] T.D. Ngo, A. Kashani, G. Imbalzano, K.T.Q. Nguyen, D. Hui, Additive manufacturing (3D printing): A review of materials, methods, applications and challenges, *Compos B Eng* 143 (2018) 172–196. <https://doi.org/10.1016/J.COMPOSITESB.2018.02.012>.
- [67] X. Gong, K. Chou, Microstructures of Inconel 718 by Selective Laser Melting, *TMS 2015 144th Annual Meeting & Exhibition* (2015) 461–468. [https://doi.org/10.1007/978-3-319-48127-2\\_58](https://doi.org/10.1007/978-3-319-48127-2_58).
- [68] Y. Hu, W. Mao, P. Yan, N. Li, Effect of Normalizing Treatment on Mechanical Properties of AISI 441 Stainless Steel Prepared by Investment Casting, *Metals* 2021, Vol. 11, Page 474 11 (2021) 474. <https://doi.org/10.3390/MET11030474>.
- [69] M.P. Sello, W.E. Stumpf, Laves phase precipitation and its transformation kinetics in the ferritic stainless steel type AISI 441, *Materials Science and Engineering: A* 528 (2011) 1840–1847. <https://doi.org/10.1016/J.MSEA.2010.09.090>.

- [70] M.P. Sello, W.E. Stumpf, Laves phase embrittlement of the ferritic stainless steel type AISI 441, *Materials Science and Engineering: A* 527 (2010) 5194–5202. <https://doi.org/10.1016/J.MSEA.2010.04.058>.
- [71] Z. Yang, G. Xia, C. Wang, Z. Nie, J. Templeton, J. Stevenson, P. Singh, A. Manivannan, T. Shultz, W. Surdoval, Investigation of AISI 441 Ferritic Stainless Steel and Development of Spinel Coatings for SOFC Interconnect Applications, 2008. <http://www.ntis.gov/ordering.htm>.
- [72] M.G. Maruma, C.W. Siyasiya, W.E. Stumpf, Mount Grace Country House and Spa, Magaliesburg, South Africa.. 115 *The Journal of The Southern African Institute of Mining and Metallurgy*, 113 (2013) 15–17.
- [73] B. Cantor, I.T.H. Chang, P. Knight, A.J.B. Vincent, Microstructural development in equiatomic multicomponent alloys, *Materials Science and Engineering: A* 375–377 (2004) 213–218. <https://doi.org/10.1016/J.MSEA.2003.10.257>.
- [74] J.W. Yeh, S.K. Chen, S.J. Lin, J.Y. Gan, T.S. Chin, T.T. Shun, C.H. Tsau, S.Y. Chang, Nanostructured high-entropy alloys with multiple principal elements: Novel alloy design concepts and outcomes, *Adv Eng Mater* 6 (2004) 299–303. <https://doi.org/10.1002/ADEM.200300567>.
- [75] E.P. George, D. Raabe, R.O. Ritchie, High-entropy alloys, *Nature Reviews Materials* 2019 4:8 4 (2019) 515–534. <https://doi.org/10.1038/s41578-019-0121-4>.
- [76] D.B. Miracle, High entropy alloys as a bold step forward in alloy development, *Nat Commun* 10 (2019) 1–3. <https://doi.org/10.1038/s41467-019-09700-1>.
- [77] M.H. Tsai, J.W. Yeh, High-entropy alloys: A critical review, *Mater Res Lett* 2 (2014) 107–123. <https://doi.org/10.1080/21663831.2014.912690>.
- [78] E.J. Pickering, N.G. Jones, High-entropy alloys: a critical assessment of their founding principles and future prospects, *International Materials Reviews* 61 (2016) 183–202. <https://doi.org/10.1080/09506608.2016.1180020>.
- [79] Y. Zhou, D. Zhou, X. Jin, L. Zhang, X. Du, B. Li, Design of non-equiatomic medium-entropy alloys, *Scientific Reports* 2018 8:1 8 (2018) 1–9. <https://doi.org/10.1038/s41598-018-19449-0>.
- [80] L. Jiang, Z.Q. Cao, J.C. Jie, J.J. Zhang, Y.P. Lu, T.M. Wang, T.J. Li, Effect of Mo and Ni elements on microstructure evolution and mechanical properties of the

- CoFeNiVMoy high entropy alloys, *J Alloys Compd* 649 (2015) 585–590. <https://doi.org/10.1016/J.JALLCOM.2015.07.185>.
- [81] S. Singh, N. Wanderka, B.S. Murty, U. Glatzel, J. Banhart, Decomposition in multi-component AlCoCrCuFeNi high-entropy alloy, *Acta Mater* 59 (2011) 182–190. <https://doi.org/10.1016/J.ACTAMAT.2010.09.023>.
- [82] A. Manzoni, H. Daoud, R. Völkl, U. Glatzel, N. Wanderka, Phase separation in equiatomic AlCoCrFeNi high-entropy alloy, *Ultramicroscopy* 132 (2013) 212–215. <https://doi.org/10.1016/J.ULTRAMIC.2012.12.015>.
- [83] C.Y. Cheng, J.W. Yeh, High thermal stability of the amorphous structure of GexNbTaTiZr (x=0.5, 1) high-entropy alloys, *Mater Lett* 181 (2016) 223–226. <https://doi.org/10.1016/J.MATLET.2016.06.040>.
- [84] Y. Zhang, Y.J. Zhou, J.P. Lin, G.L. Chen, P.K. Liaw, Solid-Solution Phase Formation Rules for Multi-component Alloys, *Adv Eng Mater* 10 (2008) 534–538. <https://doi.org/10.1002/ADEM.200700240>.
- [85] S. Guo, C. Ng, J. Lu, C.T. Liu, Effect of valence electron concentration on stability of fcc or bcc phase in high entropy alloys, *J Appl Phys* 109 (2011) 103505. <https://doi.org/10.1063/1.3587228>.
- [86] J.-W. Yeh, Physical Metallurgy of High-Entropy Alloys, *JOM* 2015 67:10 67 (2015) 2254–2261. <https://doi.org/10.1007/S11837-015-1583-5>.
- [87] S. Guo, C.T. Liu, Phase stability in high entropy alloys: Formation of solid-solution phase or amorphous phase, *Progress in Natural Science: Materials International* 21 (2011) 433–446. [https://doi.org/10.1016/S1002-0071\(12\)60080-X](https://doi.org/10.1016/S1002-0071(12)60080-X).
- [88] S. Guo, Phase selection rules for cast high entropy alloys: an overview, <https://doi.org/10.1179/1743284715Y.0000000018> 31 (2015) 1223–1230. <https://doi.org/10.1179/1743284715Y.0000000018>.
- [89] A.K. Singh, N. Kumar, A. Dwivedi, A. Subramaniam, A geometrical parameter for the formation of disordered solid solutions in multi-component alloys, *Intermetallics* (Barking) 53 (2014) 112–119. <https://doi.org/10.1016/J.INTERMET.2014.04.019>.



- [90] X. Yang, Y. Zhang, Prediction of high-entropy stabilized solid-solution in multi-component alloys, *Mater Chem Phys* 132 (2012) 233–238. <https://doi.org/10.1016/J.MATCHEMPHYS.2011.11.021>.
- [91] K.G. Pradeep, C.C. Tasan, M.J. Yao, Y. Deng, H. Springer, D. Raabe, Non-equiatomic high entropy alloys: Approach towards rapid alloy screening and property-oriented design, *Materials Science and Engineering: A* 648 (2015) 183–192. <https://doi.org/10.1016/J.MSEA.2015.09.010>.
- [92] C.J. Tong, Y.L. Chen, S.K. Chen, J.W. Yeh, T.T. Shun, C.H. Tsau, S.J. Lin, S.Y. Chang, Microstructure characterization of Al<sub>x</sub>CoCrCuFeNi high-entropy alloy system with multiprincipal elements, *Metall Mater Trans A Phys Metall Mater Sci* 36 (2005) 881–893. <https://doi.org/10.1007/s11661-005-0283-0>.
- [93] C.J. Tong, M.R. Chen, S.K. Chen, J.W. Yeh, T.T. Shun, S.J. Lin, S.Y. Chang, Mechanical performance of the Al<sub>x</sub>CoCrCuFeNi high-entropy alloy system with multiprincipal elements, in: *Metall Mater Trans A Phys Metall Mater Sci, Minerals, Metals and Materials Society*, 2005: pp. 1263–1271. <https://doi.org/10.1007/s11661-005-0218-9>.
- [94] H.-P. Chou, Y.-S. Chang, S.-K. Chen, J.-W. Yeh, Microstructure, thermophysical and electrical properties in Al<sub>x</sub>CoCrFeNi ( $0 \leq x \leq 2$ ) high-entropy alloys, *Materials Science and Engineering: B* 163 (2009) 184–189. <https://doi.org/10.1016/J.MSEB.2009.05.024>.
- [95] J. Joseph, T. Jarvis, X. Wu, N. Stanford, P. Hodgson, D.M. Fabijanic, Comparative study of the microstructures and mechanical properties of direct laser fabricated and arc-melted Al<sub>x</sub>CoCrFeNi high entropy alloys, *Materials Science and Engineering A* 633 (2015) 184–193. <https://doi.org/10.1016/j.msea.2015.02.072>.
- [96] Y.F. Kao, S.K. Chen, T.J. Chen, P.C. Chu, J.W. Yeh, S.J. Lin, Electrical, magnetic, and Hall properties of Al<sub>x</sub>CoCrFeNi high-entropy alloys, *J Alloys Compd* 509 (2011) 1607–1614. <https://doi.org/10.1016/j.jallcom.2010.10.210>.
- [97] Y.H. Jo, W.M. Choi, D.G. Kim, A. Zargaran, S.S. Sohn, H.S. Kim, B.J. Lee, N.J. Kim, S. Lee, FCC to BCC transformation-induced plasticity based on thermodynamic phase stability in novel V<sub>10</sub>Cr<sub>10</sub>Fe<sub>45</sub>Co<sub>x</sub>Ni<sub>35-x</sub> medium-

- entropy alloys, *Scientific Reports* 2019 9:1 9 (2019) 1–14. <https://doi.org/10.1038/s41598-019-39570-y>.
- [98] S. Basu, Z. Li, K.G. Pradeep, D. Raabe, Strain rate sensitivity of a TRIP-assisted dual-phase high-entropy alloy, *Front Mater* 5 (2018) 379083. <https://doi.org/10.3389/FMATS.2018.00030/BIBTEX>.
- [99] D. Raabe, Z. Li, D. Ponge, Metastability alloy design, *MRS Bull* 44 (2019) 266–272. <https://doi.org/10.1557/MRS.2019.72>.
- [100] Z. Li, K.G. Pradeep, Y. Deng, D. Raabe, C.C. Tasan, Metastable high-entropy dual-phase alloys overcome the strength–ductility trade-off, *Nature* 2016 534:7606 534 (2016) 227–230. <https://doi.org/10.1038/nature17981>.
- [101] C.C. Tasan, Y. Deng, K.G. Pradeep, M.J. Yao, H. Springer, D. Raabe, Composition Dependence of Phase Stability, Deformation Mechanisms, and Mechanical Properties of the CoCrFeMnNi High-Entropy Alloy System, *JOM* 66 (2014) 1993–2001. <https://doi.org/10.1007/S11837-014-1133-6/TABLES/1>.
- [102] H. Huang, J. Wang, H. Yang, S. Ji, H. Yu, Z. Liu, Strengthening CoCrNi medium-entropy alloy by tuning lattice defects, *Scr Mater* 188 (2020) 216–221. <https://doi.org/10.1016/J.SCRIPTAMAT.2020.07.027>.
- [103] J.P. Liu, J.X. Chen, T.W. Liu, C. Li, Y. Chen, L.H. Dai, Superior strength-ductility CoCrNi medium-entropy alloy wire, *Scr Mater* 181 (2020) 19–24. <https://doi.org/10.1016/J.SCRIPTAMAT.2020.02.002>.
- [104] H. Huang, J. Wang, H. Yang, S. Ji, H. Yu, Z. Liu, Strengthening CoCrNi medium-entropy alloy by tuning lattice defects, *Scr Mater* 188 (2020) 216–221. <https://doi.org/10.1016/j.scriptamat.2020.07.027>.
- [105] Z. Li, K.G. Pradeep, Y. Deng, D. Raabe, C.C. Tasan, Metastable high-entropy dual-phase alloys overcome the strength-ductility trade-off., *Nature* 534 (2016) 227–30. <https://doi.org/10.1038/nature17981>.
- [106] B. Gludovatz, A. Hohenwarter, K.V.S. Thurston, H. Bei, Z. Wu, E.P. George, R.O. Ritchie, Exceptional damage-tolerance of a medium-entropy alloy CrCoNi at cryogenic temperatures, *Nat Commun* 7 (2016) 1–8. <https://doi.org/10.1038/ncomms10602>.

- [107] A. Saeed-Akbari, J. Imlau, U. Prah, W. Bleck, Derivation and Variation in Composition-Dependent Stacking Fault Energy Maps Based on Subregular Solution Model in High-Manganese Steels, *Metallurgical and Materials Transactions A* 2009 40:13 40 (2009) 3076–3090. <https://doi.org/10.1007/S11661-009-0050-8>.
- [108] W. Woo, J.S. Jeong, D.-K. Kim, C.M. Lee, S.-H. Choi, J.-Y. Suh, S.Y. Lee, S. Harjo, T. Kawasaki, Stacking Fault Energy Analyses of Additively Manufactured Stainless Steel 316L and CrCoNi Medium Entropy Alloy Using In Situ Neutron Diffraction, *Scientific Reports* 2020 10:1 10 (2020) 1–15. <https://doi.org/10.1038/s41598-020-58273-3>.
- [109] A.J. Zaddach, C. Niu, C.C. Koch, D.L. Irving, Mechanical properties and stacking fault energies of NiFeCrCoMn high-entropy alloy, *JOM* 65 (2013) 1780–1789. <https://doi.org/10.1007/S11837-013-0771-4>.
- [110] M. Shih, J. Miao, M. Mills, M. Ghazisaeidi, Stacking fault energy in concentrated alloys, *Nature Communications* 2021 12:1 12 (2021) 1–10. <https://doi.org/10.1038/s41467-021-23860-z>.
- [111] S. Zhao, Y. Osetsky, G.M. Stocks, Y. Zhang, Local-environment dependence of stacking fault energies in concentrated solid-solution alloys, *Npj Computational Materials* 2019 5:1 5 (2019) 1–7. <https://doi.org/10.1038/s41524-019-0150-y>.
- [112] F. Otto, A. Dlouhý, C. Somsen, H. Bei, G. Eggeler, E.P. George, The influences of temperature and microstructure on the tensile properties of a CoCrFeMnNi high-entropy alloy, *Acta Mater* 61 (2013) 5743–5755. <https://doi.org/10.1016/J.ACTAMAT.2013.06.018>.
- [113] S. Huang, H. Huang, W. Li, D. Kim, S. Lu, X. Li, E. Holmström, S.K. Kwon, L. Vitos, Twinning in metastable high-entropy alloys, *Nature Communications* 2018 9:1 9 (2018) 1–7. <https://doi.org/10.1038/s41467-018-04780-x>.
- [114] J. Su, X. Wu, D. Raabe, Z. Li, Deformation-driven bidirectional transformation promotes bulk nanostructure formation in a metastable interstitial high entropy alloy, *Acta Mater* 167 (2019) 23–39. <https://doi.org/10.1016/J.ACTAMAT.2019.01.030>.
- [115] S.F. Liu, Y. Wu, H.T. Wang, W.T. Lin, Y.Y. Shang, J.B. Liu, K. An, X.J. Liu, H. Wang, Z.P. Lu, Transformation-reinforced high-entropy alloys with superior

- mechanical properties via tailoring stacking fault energy, (2019). <https://doi.org/10.1016/j.jallcom.2019.04.035>.
- [116] T. Zheng, J. Lv, Y. Wu, H.H. Wu, S. Liu, J. Tang, M. Zhou, H. Wang, X. Liu, S. Jiang, Z. Lu, Effects of stacking fault energy on the deformation behavior of CoNiCrFeMn high-entropy alloys: A molecular dynamics study, *Appl Phys Lett* 119 (2021). <https://doi.org/10.1063/5.0069108/1065158>.
- [117] D. Wei, X. Li, W. Heng, Y. Koizumi, F. He, W.-M. Choi, B.-J. Lee, H.S. Kim, H. Kato, A. Chiba, Novel Co-rich high entropy alloys with superior tensile properties, 7 (2019) 82–88. <https://doi.org/10.1080/21663831.2018.1553803>.
- [118] J. Su, D. Raabe, Z. Li, Hierarchical microstructure design to tune the mechanical behavior of an interstitial TRIP-TWIP high-entropy alloy, *Acta Mater* 163 (2019) 40–54. <https://doi.org/10.1016/J.ACTAMAT.2018.10.017>.
- [119] Z. Wang, W. Lu, D. Raabe, Z. Li, On the mechanism of extraordinary strain hardening in an interstitial high-entropy alloy under cryogenic conditions, *J Alloys Compd* 781 (2019) 734–743. <https://doi.org/10.1016/J.JALLCOM.2018.12.061>.
- [120] W. Lu, C.H. Liebscher, G. Dehm, D. Raabe, Z. Li, W. Lu, C.H. Liebscher, G. Dehm, D. Raabe, Z. Li, Bidirectional Transformation Enables Hierarchical Nanolaminate Dual-Phase High-Entropy Alloys, *Advanced Materials* 30 (2018) 1804727. <https://doi.org/10.1002/ADMA.201804727>.
- [121] G. Wu, S. Balachandran, B. Gault, W. Xia, C. Liu, Z. Rao, Y. Wei, S. Liu, J. Lu, M. Herbig, W. Lu, G. Dehm, Z. Li, D. Raabe, G. Wu, S. Balachandran, B. Gault, W. Xia, C. Liu, Z. Rao, Y. Wei, M. Herbig, W. Lu, G. Dehm, Z. Li, D. Raabe, S. Liu, J. Lu, Crystal–Glass High-Entropy Nanocomposites with Near Theoretical Compressive Strength and Large Deformability, *Advanced Materials* 32 (2020) 2002619. <https://doi.org/10.1002/ADMA.202002619>.
- [122] B. Schuh, F. Mendez-Martin, B. Völker, E.P. George, H. Clemens, R. Pippan, A. Hohenwarter, Mechanical properties, microstructure and thermal stability of a nanocrystalline CoCrFeMnNi high-entropy alloy after severe plastic deformation, *Acta Mater* 96 (2015) 258–268. <https://doi.org/10.1016/j.actamat.2015.06.025>.

- [123] A.D.J. Saldívar García, A. Maní Medrano, A. Salinas Rodríguez, Effect of solution treatments on the FCC/HCP isothermal martensitic transformation in Co-27Cr-5Mo-0.05C aged at 800°C, *Scr Mater* 40 (1999) 717–722. [https://doi.org/10.1016/S1359-6462\(98\)00489-8](https://doi.org/10.1016/S1359-6462(98)00489-8).
- [124] C.K. Soundararajan, H. Luo, D. Raabe, Z. Li, Hydrogen resistance of a 1 GPa strong equiatomic CoCrNi medium entropy alloy, *Corros Sci* 167 (2020) 108510. <https://doi.org/10.1016/J.CORSCI.2020.108510>.
- [125] F. Weng, Y. Chew, Z. Zhu, S. Sui, C. Tan, X. Yao, F.L. Ng, W.K. Ong, G. Bi, Influence of oxides on the cryogenic tensile properties of the laser aided additive manufactured CoCrNi medium entropy alloy, *Compos B Eng* 216 (2021) 108837. <https://doi.org/10.1016/J.COMPOSITESB.2021.108837>.
- [126] N.K. Adomako, J.H. Kim, Y.T. Hyun, High-temperature oxidation behaviour of low-entropy alloy to medium- and high-entropy alloys, *Journal of Thermal Analysis and Calorimetry* 2018 133:1 133 (2018) 13–26. <https://doi.org/10.1007/S10973-018-6963-Y>.
- [127] X. Shang, Z. Wang, F. He, J. Wang, J. Li, J. Yu, The intrinsic mechanism of corrosion resistance for FCC high entropy alloys, *Science China Technological Sciences* 2017 61:2 61 (2017) 189–196. <https://doi.org/10.1007/S11431-017-9114-1>.
- [128] J. Yan, W. Fang, J. Huang, J. Zhang, R. Chang, X. Zhang, B. Liu, J. Feng, F. Yin, Plastic deformation mechanism of CoCr<sub>x</sub>Ni medium entropy alloys, *Materials Science and Engineering: A* 814 (2021) 141181. <https://doi.org/10.1016/J.MSEA.2021.141181>.
- [129] H. He, M. Naeem, F. Zhang, Y. Zhao, S. Harjo, T. Kawasaki, B. Wang, X. Wu, S. Lan, Z. Wu, W. Yin, Y. Wu, Z. Lu, J.J. Kai, C.T. Liu, X.L. Wang, Stacking Fault Driven Phase Transformation in CrCoNi Medium Entropy Alloy, *Nano Lett* 21 (2021) 1419–1426. [https://doi.org/10.1021/ACS.NANOLETT.0C04244/ASSET/IMAGES/LARGE/NL0C04244\\_M003.JPEG](https://doi.org/10.1021/ACS.NANOLETT.0C04244/ASSET/IMAGES/LARGE/NL0C04244_M003.JPEG).
- [130] I. Moravcik, J. Cizek, L. de A. Gouvea, J. Cupera, I. Guban, I. Dlouhy, Nitrogen interstitial alloying of CoCrFeMnNi high entropy alloy through reactive powder milling, *Entropy* 21 (2019) 1–7. <https://doi.org/10.3390/e21040363>.

- [131] I. Moravcik, V. Hornik, P. Minárik, L. Li, I. Dlouhy, M. Janovska, D. Raabe, Z. Li, Interstitial doping enhances the strength-ductility synergy in a CoCrNi medium entropy alloy, *Materials Science and Engineering: A* 781 (2020) 139242. <https://doi.org/10.1016/J.MSEA.2020.139242>.
- [132] I. Moravcik, H. Hadraba, L. Li, I. Dlouhy, D. Raabe, Z. Li, Yield strength increase of a CoCrNi medium entropy alloy by interstitial nitrogen doping at maintained ductility, *Scr Mater* 178 (2020) 391–397. <https://doi.org/10.1016/J.SCRIPTAMAT.2019.12.007>.
- [133] I. Moravcik, N.S. Peighambardoust, A. Motallebzadeh, L. Moravcikova-Gouvea, C. Liu, J.M. Prabhakar, I. Dlouhy, Z. Li, Interstitial nitrogen enhances corrosion resistance of an equiatomic CoCrNi medium-entropy alloy in sulfuric acid solution, *Mater Charact* 172 (2021) 110869. <https://doi.org/10.1016/J.MATCHAR.2020.110869>.
- [134] I. Moravcik, N.S. Peighambardoust, A. Motallebzadeh, L. Moravcikova-Gouvea, C. Liu, J.M. Prabhakar, I. Dlouhy, Z. Li, Interstitial nitrogen enhances corrosion resistance of an equiatomic CoCrNi medium-entropy alloy in sulfuric acid solution, *Mater Charact* 172 (2021) 110869. <https://doi.org/10.1016/J.MATCHAR.2020.110869>.
- [135] Y.Y. Shang, Y. Wu, J.Y. He, X.Y. Zhu, S.F. Liu, H.L. Huang, K. An, Y. Chen, S.H. Jiang, H. Wang, X.J. Liu, Z.P. Lu, Solving the strength-ductility tradeoff in the medium-entropy NiCoCr alloy via interstitial strengthening of carbon, *Intermetallics* (Barking) 106 (2019) 77–87. <https://doi.org/10.1016/J.INTERMET.2018.12.009>.
- [136] S.B.A. Malladi, P.L. Tam, Y. Cao, S. Guo, L. Nyborg, Corrosion behaviour of additively manufactured 316L and CoCrNi, *Surface and Interface Analysis* 55 (2023) 404–410. <https://doi.org/10.1002/sia.7200>.
- [137] I. Moravcik, M. Zelený, A. Dlouhy, H. Hadraba, L. Moravcikova-Gouvea, P. Papež, O. Fikar, I. Dlouhy, D. Raabe, Z. Li, Impact of interstitial elements on the stacking fault energy of an equiatomic CoCrNi medium entropy alloy: theory and experiments, *Sci Technol Adv Mater* 23 (2022) 376–392. <https://doi.org/10.1080/14686996.2022.2080512>.

- [138] M. Klimova, D. Shaysultanov, A. Semenyuk, S. Zherebtsov, N. Stepanov, Effect of carbon on recrystallised microstructures and properties of CoCrFeMnNi-type high-entropy alloys, *J Alloys Compd* 851 (2021) 156839. <https://doi.org/10.1016/J.JALLCOM.2020.156839>.
- [139] D.E. Jodi, J. Park, N. Park, Precipitate behavior in nitrogen-containing CoCrNi medium-entropy alloys, *Mater Charact* 157 (2019) 109888. <https://doi.org/10.1016/j.matchar.2019.109888>.
- [140] D.E. Jodi, N. Choi, J. Park, N. Park, Mechanical Performance Improvement by Nitrogen Addition in N-CoCrNi Compositionally Complex Alloys, *Metallurgical and Materials Transactions A* 2020 51:6 51 (2020) 3228–3237. <https://doi.org/10.1007/S11661-020-05738-9>.
- [141] J. Zhang, K.N. Yoon, M.S. Kim, H.S. Ahn, J.Y. Kim, Z. Li, T. Sasaki, K. Hono, E.S. Park, Strengthening by customizing microstructural complexity in nitrogen interstitial CoCrFeMnNi high-entropy alloys, *J Alloys Compd* 901 (2022) 163483. <https://doi.org/10.1016/J.JALLCOM.2021.163483>.
- [142] E. Abbe, Beiträge zur Theorie des Mikroskops und der mikroskopischen Wahrnehmung: I. Die Construction von Mikroskopen auf Grund der Theorie, *Archiv Für Mikroskopische Anatomie* 9 (1873) 413–418. <https://doi.org/10.1007/BF02956173/METRICS>.
- [143] Ponor, Electron-matter interaction volume and various types of signal generated - Wikimedia Commons, (n.d.). <https://commons.wikimedia.org/w/index.php?curid=93635964> (accessed September 27, 2021).
- [144] F. Bachmann, R. Hielscher, H. Schaeben, Texture Analysis with MTEX – Free and Open Source Software Toolbox, *Solid State Phenomena* 160 (2010) 63–68. <https://doi.org/10.4028/WWW.SCIENTIFIC.NET/SSP.160.63>.
- [145] P.J. Goodhew, J. Humphreys, J. Humphreys, *Electron Microscopy and Analysis, Electron Microscopy and Analysis* (2000). <https://doi.org/10.1201/9781482289343>.
- [146] G.A. Jeffery, Elements of x-ray diffraction (Cullity, B. D.), *J Chem Educ* 34 (1957) A178. <https://doi.org/10.1021/ED034PA178>.

- [147] A. Balerna, S. Mobilio, Introduction to synchrotron radiation, *Synchrotron Radiation: Basics, Methods and Applications* (2015) 3–28. [https://doi.org/10.1007/978-3-642-55315-8\\_1/FIGURES/23](https://doi.org/10.1007/978-3-642-55315-8_1/FIGURES/23).
- [148] G. Artioli, Powder diffraction and synchrotron radiation, *Synchrotron Radiation: Basics, Methods and Applications* (2015) 319–336. [https://doi.org/10.1007/978-3-642-55315-8\\_10/FIGURES/10](https://doi.org/10.1007/978-3-642-55315-8_10/FIGURES/10).
- [149] C. Hanmandlu, A. Singh, K. Moorthy Boopathi, al -, J. Hyuck Heo, N. Mya Su Aung, S. Yeong Hong, G. Abbondanza, A. Grespi, A. Larsson, J. Kieffer, D. Karkoulis, PyFAI, a versatile library for azimuthal regrouping, *J Phys Conf Ser* 425 (2013) 202012. <https://doi.org/10.1088/1742-6596/425/20/202012>.
- [150] M. Newville, T. Stensitzki, D.B. Allen, A. Ingargiola, LMFIT: Non-Linear Least-Square Minimization and Curve-Fitting for Python, (n.d.). <https://doi.org/10.5281/ZENODO.11813>.
- [151] B.H. Toby, R.B. Von Dreele, GSAS-II: the genesis of a modern open-source all purpose crystallography software package, *Urn:Issn:0021-8898 46* (2013) 544–549. <https://doi.org/10.1107/S0021889813003531>.
- [152] S.B.A. Malladi, Z. Chen, A. Durga, N.H. Pettersson, G. Lindwall, S. Guo, L. Nyborg, Single track versus bulk samples: Understanding the grain refinement in inoculated ferritic stainless steels manufactured by powder bed fusion-laser beam, *Materialia (Oxf)* (2023) 101952. <https://doi.org/10.1016/j.mtla.2023.101952>.
- [153] J. Fu, Q. Nie, W. Qiu, J. Liu, Y. Wu, Morphology, orientation relationships and formation mechanism of TiN in Fe-17Cr steel during solidification, *Mater Charact* 133 (2017) 176–184. <https://doi.org/10.1016/J.MATCHAR.2017.10.001>.
- [154] A. Hunter, M. Ferry, Texture enhancement by inoculation during casting of ferritic stainless steel strip, *Metall Mater Trans A Phys Metall Mater Sci* 33 (2002) 1499–1507. <https://doi.org/10.1007/s11661-002-0072-y>.
- [155] Y. Wu, S. Zhang, X. Cheng, H. Wang, Investigation on solid-state phase transformation in a Ti-47Al-2Cr-2V alloy due to thermal cycling during laser additive manufacturing process, *J Alloys Compd* 799 (2019) 325–333. <https://doi.org/10.1016/J.JALLCOM.2019.05.337>.
- [156] Y. Liu, J. Zhang, Z. Pang, Numerical and experimental investigation into the subsequent thermal cycling during selective laser melting of multi-layer 316L



- stainless steel, *Opt Laser Technol* 98 (2018) 23–32.  
<https://doi.org/10.1016/J.OPTLASTEC.2017.07.034>.
- [157] T. Zacharia, S.A. David, J.M. Vitek, T. Debroy, Heat transfer during Nd: Yag pulsed laser welding and its effect on solidification structure of austenitic stainless steels, *Metallurgical Transactions A* 20 (1989) 957–967.  
<https://doi.org/10.1007/BF02651661/METRICS>.
- [158] Y. Liu, Z. Pang, J. Zhang, Comparative study on the influence of subsequent thermal cycling on microstructure and mechanical properties of selective laser melted 316L stainless steel, *Appl Phys A Mater Sci Process* 123 (2017) 1–10.  
<https://doi.org/10.1007/S00339-017-1313-7/FIGURES/8>.
- [159] S.B.A. Malladi, L. Cordova, S. Guo, L. Nyborg, Laser-based Powder Bed Fusion of dispersion strengthened CoCrNi by ex-situ addition of TiN, in: *Procedia CIRP*, Elsevier B.V., 2022: pp. 368–372.  
<https://doi.org/10.1016/j.procir.2022.08.168>.
- [160] A. Charmi, R. Falkenberg, L. Ávila, G. Mohr, K. Sommer, A. Ulbricht, M. Sprengel, R. Saliwan Neumann, B. Skrotzki, A. Evans, Mechanical anisotropy of additively manufactured stainless steel 316L: An experimental and numerical study, *Materials Science and Engineering: A* 799 (2021) 140154.  
<https://doi.org/10.1016/J.MSEA.2020.140154>.
- [161] Y.M. Wang, T. Voisin, J.T. McKeown, J. Ye, N.P. Calta, Z. Li, Z. Zeng, Y. Zhang, W. Chen, T.T. Roehling, R.T. Ott, M.K. Santala, P.J. Depond, M.J. Matthews, A. V. Hamza, T. Zhu, Additively manufactured hierarchical stainless steels with high strength and ductility, *Nature Materials* 17:1 17 (2017) 63–71.  
<https://doi.org/10.1038/nmat5021>.